Moist Baroclinic Instability and Macroturbulence of the Midlatitude Atmosphere

by

Matthieu Kohl

Submitted to the Department of Earth, Atmospheric, and Planetary Sciences
in partial fulfillment of the requirements for the degree of

Doctor of Philosophy in Atmospheric Science

at the

MASSACHUSETTS INSTITUTE OF TECHNOLOGY

February 2023

Author .....
Department of Earth, Atmospheric, and Planetary Sciences
December 15, 2022

Certified by .....
Paul A. O'Gorman
Professor of Atmospheric Science
Thesis Supervisor

Accepted by .....
Robert van der Hilst
Schlumberger Professor of Earth and Planetary Sciences
Head of Department of Earth, Atmospheric, and Planetary Sciences

Moist Baroclinic Instability and Macroturbulence of the Midlatitude Atmosphere

by

Matthieu Kohl

Submitted to the Department of Earth, Atmospheric, and Planetary Sciences
on December 15, 2022, in partial fulfillment of the
requirements for the degree of
Doctor of Philosophy in Atmospheric Science

Abstract

Water and its change of phase greatly enrich the dynamics of the midlatitude atmosphere and challenge us to extend our theories of baroclinic instability and macroturbulence beyond dry adiabatic dynamics. Two specific phenomena in which latent heating plays a key role and that are poorly understood form the central focus of this thesis.

Past research has identified a special class of storm, dubbed the Diabatic Rossby Vortex (DRVs), which derives its energy from latent heating rather than baroclinic effects and as such goes beyond the traditional understanding of midlatitude storm formation. DRVs have been implicated in extreme and poorly predicted forms of cyclogenesis along the east coast of the US and west coast of Europe and have recently emerged as the dominant mode of instability in an idealized GCM with climate warming. While we have a good theoretical understanding of dry cyclogenesis, our understanding of DRV formation, and propagation as well as their growth rate and length scale is poor. In chapters 2 and 4 of my thesis, a fluid dynamical theory is developed for DRVs both in terms of simple conceptual models of moist instability and potential vorticity dynamics of finite-amplitude storms. In particular, the dispersion relation for the growth rate and length scale of DRVs is derived analytically, and it is shown that DRVs become faster than both dry or moist baroclinic waves in the limit of a convectively-neutral stratification.

Latent heating also makes upward motion stronger than downward motion, and this asymmetry has important implications for the distribution of precipitation and its extremes. Current theories based around small-amplitude modes greatly overestimate the change in asymmetry with warming. In chapter 3, we develop a toy-model that takes into account adjustment of the atmosphere to a state of moist macroturbulence and show that it better reproduces the slow increase in the asymmetry from winter to summer over the seasonal cycle in reanalysis and with climate warming in idealized simulations.

Thesis Supervisor: Paul A. O'Gorman

Title: Professor of Atmospheric Science

Acknowledgments

I am deeply indebted to my advisor Paul O'Gorman for his close scientific collaboration and mentorship over the years of my PhD, always generous with his time and his ideas. Above all, I appreciate the freedom and support he gave me to work in a manner that was true to my training and style in geophysical fluid dynamics, and the openness and interest he showed to discuss ideas beyond science. I look back with special fondness to three moments: my first visit to MIT when Paul suggested a paper for discussion that was particularly well-aligned with my background and interests - finding explanations for the results of this paper formed the basis of most of my PhD; a meeting spent discussing the applicability of Kuhn's concept of normal and revolution to atmospheric and climate science; and a flurry of email exchanges over the weekend in January 2020 when we shared a special moment of DRV discovery after our usual Friday meeting. I have learned a lot from Paul beyond the purely scientific: perseverance in the face of hard problems, attention to the whole and the parts, remaining respectful and kind in disagreement, clarity of writing and thinking, and the ability to make ever more elegant figures and slides. Go raibh maith agat!

I would also like to express my gratitude to my other committee members: Stephan Pfahl for always challenging me to connect theories to observation, Glenn Flierl for always having an open door for me and for the many blackboard discussions over the years, and Kerry Emanuel for going out of his way to organize a special reading course on moist midlatitude dynamics in my first semester - without this introduction, which is hard to come by in books and lectures, most of this thesis work would not have been possible. Beyond the scientific support, I would like to thank all of them for the kindness, understanding and guidance they showed when I had to navigate through an extremely difficult phase of my life.

Many thanks also go to faculty at EAPS and at previous institutions that I attended: Susan Solomon for investing time into teaching interdisciplinary courses on environmental history and policy at MIT and allowing me to join the experience as a TA, John Marshall for the many conversations over the years about science, politics,

and life in the UK - although you told me not to do another baroclinic instability study for my PhD, I hope you find the one in this thesis interesting :), Olivier Darrigol for hosting me at Berkeley and the many conversations since about the history of science, Michael McIntyre for coming out of quasi-retirement to allow a part III student to work on vortices in Jupiter's weather layer and for instilling your principles of lucidity - I hope you find this thesis lived up to them -, and Guillaume Lapeyre for hosting me for almost an entire year in your office at ENS and sparking my continued interest for all variables asymmetric.

I would also like to express my indebtedness to the support I have received over the years from the many staff members at EAPS, in particular Megan Jordan, Brandon Milardo, Alma Pellecer, Roberta Allard, David Wright, Daisy Cabin, and Ann Greaney-Williams, which greatly facilitated the administrative hurdles I had to clear to study at MIT - particularly as an international student in pandemic times -, and allowed me to focus fully on completing the research for this thesis. Thank you!

Special thanks also go to colleagues who became close friends and supported me with their good spirits throughout my time at MIT: Ziwei Li for the tears and sweat spent over code and badminton courts, Martín Vélez-Pardo for the many discussions during long walks around Charles river, Santiago Benavides for sharing in my love and enthusiasm for 'good old GFD' and getting me up to speed on dedalus with as much support and interest as if it were your own project, Evghenia Prikhodko for our conversations about literature and Europe and the many fun evenings at Clary street (when I move out of the dorm rooms and have a living room of my own, I will finally return the favor), Raphael Rousseau for sharing in my enthusiasm about the outdoors and taking me on long hikes, Constantin Arnscheidt for the many discussions about life and doing science in Germany, UK and the US, Jonathan Lin for the many conversations about the differences between tropical and extratropical dynamics and how to lead a happy life, Kasturi Shah and Zahra Essack for forming the undefeatable trio of international students in the face of bureaucracy and political crisis, Minmin Fu for the many walks and talks about the state of climate science and the world, and all my past and current office mates for the many fond memories of friendship

over shared lunches and cookie hours at EAPS and reminding me that 'Before you do science, you should eat'!

Last but not least, vielen Dank an Adrian van Kan, Oliver Leicht, David Schnettler, Mark Daniels, Pedro Lippmann, Lukas Huwald für die vielen Jahre der Freundschaft. Doris, Frank und Sunny für die schönen Momente am Strand in Frankreich und das Gefühl der Entspannung in stressigen Zeiten. Mama, Papa und Fabien für eure Mühen, eure permanente Zusprache, das liebevolle Zuhause, und die ständige Unterstützung und Freiheit zu werden wer ich bin. Papy Maurice pour ton exemple de toujours cultiver un esprit sain et curieux dans un corps sain. Ganz zum Schluss Sinja, für die Liebe, Geborgenheit und Ruhe in guten wie in schlechten Zeiten und das Glück, den schönsten Moment der Entdeckung dieser Arbeit mit dir zusammen geteilt zu haben. $\Sigma\epsilon\ \phi\iota\lambda\tilde{\omega}$!

Ich widme diese Arbeit in liebevollem Gedenken an meinen Opa Willi Kohl und meine Oma Christiane Pey. Je dédie ce travail en douce mémoire à mon papy Willi Kohl et ma mamie Christiane Pey.

I acknowledge financial support from NSF AGS 2031472, the MIT presidential fellowship, the Warren-Klein fellowship and the mTerra Catalyst Fund.

Contents

List of Figures

List of Tables

Chapter 1

Introduction

Cloud imagery from geostationary satellites reveals the rich class of dynamical motions present in the atmosphere on any given day of weather from the small-scale puffy convective motion in the tropics to the large-scale comma shaped midlatitude cyclones with their elongated frontal bands and their anticlockwise swirl in the Northern Hemisphere and clockwise swirl in the Southern Hemisphere (Fig. 1-1). In this thesis we will limit ourselves to large-scale motion in the midlatitudes and be concerned with two broad themes: how do perturbations grow in the midlatitude atmosphere and develop into extratropical storms that we see on satellite imagery (the problem of instability), and how do the statistical properties of the midlatitude flow look like in the presence of many growing and decaying perturbations (the problem of macroturbulence[1]). In both of these themes our overarching concern will be the role that water and its change of phase play in the dynamics through the release of latent heating. We will call this the problem of moist baroclinic instability and macroturbulence of the midlatitude atmosphere.

When looking at cloud imagery from satellites, it is tempting to regard the clouds as mere markers of the underlying dynamics, passive tracers that are being advected around like white dye without any active part to play in generating and sustaining the dynamical patterns themselves. Much of our theoretical understanding of the

[1]Here macroturbulence is used following Held (1999) to refer to the turbulence of the large scale atmosphere, as distinct from the turbulence in say the boundary layer.

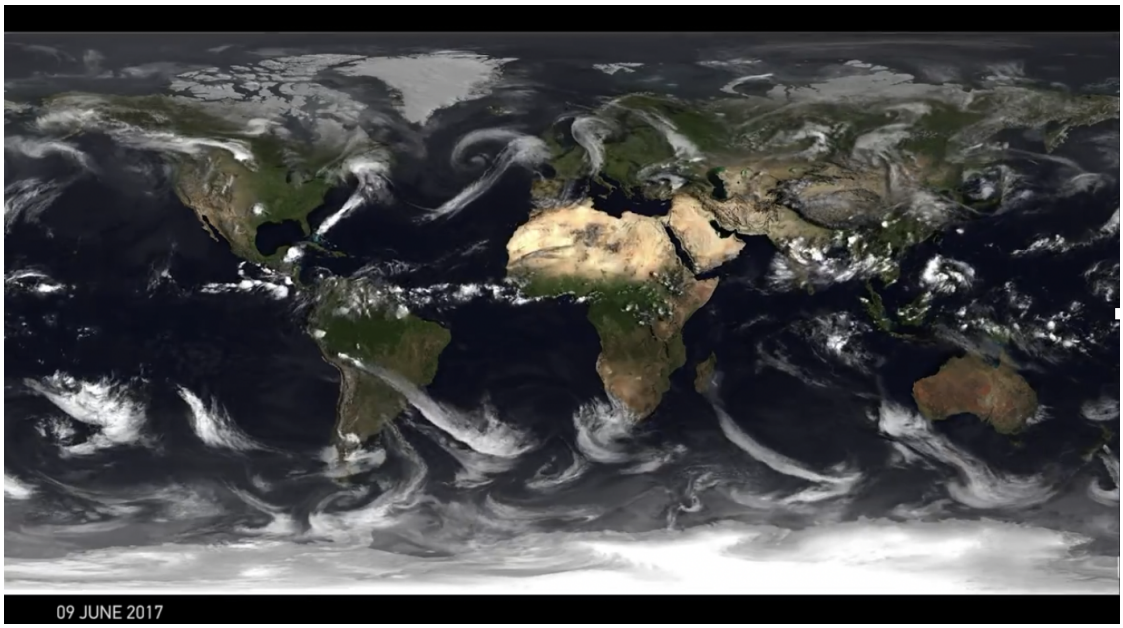

Figure 1-1: Global infrared satellite imagery from EUMETSAT for 9th June, 2017. The two storms that are visible in the North Atlantic, one close to the east coast of US and one close to the west coast of Europe, were identified as DRVs by the tracking algorithm of Boettcher and Wernli (2013) as part of an updated DRV climatology based on ERA5 reanalysis. Both disturbances originated within a strong cloud field off the coast of Florida. The first disturbance propagated more zonally towards Europe, the second disturbance propagated more meridionally along the coast of the US with a day succession. Photo has been extracted from the EUMETSAT video 'A year of weather' ©EUMETSAT[2017].

dynamics of storms, fronts and macroturbulence in the midlatitudes today still hails from such a simplified dry-adiabatic view of the atmosphere (e.g. Charney 1947, Eady 1949, Phillips 1954, Hoskins 1975, Hoskins 1976, Charney 1971).[2] And for good reason. By ignoring the complexity of moist processes, it was possible to isolate in simple mathematical models the disturbances and macroturbulent states resulting from the energy supply of an unstable meridional temperature gradient alone and to show broad agreement with midlatitude flow. It has been pointed out however, that in the process midlatitude dynamics underwent a process of "dessication" which jars with our basic experience of weather and stands in sharp contrast to the 'thermal view' of the midlatitudes in the 19th century. This thermal view placed great emphasis on the thermodynamics of water and its change of phase, and the important role of latent heating as an energetic source for the midlatitude storms (Kutzbach 1979, Emanuel 2001). Indeed, considerable work has shown that latent heating processes play a crucial part in the dynamics of the midlatitude atmosphere. It changes the growth rate, length scale, and predictability of storms and ultimately gives rise to new classes of disturbances and turbulent states that have no direct analogue in dry-adiabatic theory (e.g. Emanuel et al. (1987), Wernli et al. (2002), Lapeyre and Held (2004)). We have recovered only slowly from this Kuhnian loss of moist processes in our midlatitude theories. Understanding the role of water in weather and climate has thus been posed as one of the grand challenges of the science of meteorology as it entered its new millenium (Emanuel 2001). This rings true even more so today as the pressing concerns associated with climate change push us to extend our theoretical understanding of cyclogenesis and macroturbulence into ever warmer and moister climate regimes in which latent heating effects become increasingly important. On a high level therefore, this PhD is the continuation of an investigation into the integral role that latent heating plays in the dynamics of the midlatitude atmosphere and an attempt to isolate its effects in simple mathematical models that are "effective

[2]It should be noted that the modern presentation of such models in textbooks is sometimes 'drier' than the original authors probably intended. In a later section of his paper, Eady (1949) for instance acknowledged the limitations of a purely dry description and sought to extend his model by including a zone of saturated air in the instability analysis as an extension. He noted the tendency towards frontogenesis at the boundary of the cloudy zone and the increase in growth rates.

equivalents for the purposes of theoretical computation", to borrow from the late Napier Shaw's 'Methods of Meteorological Investigation' (Shaw 1903).

Two specific phenomena in which latent heating plays a key role and that have challenged our theoretical understanding form the central focus of this thesis: 1.) Diabatic Rossby Vortices, which are a special class of midlatitude storms that derive their energy from latent heating, rather than baroclinic effects and as such go beyond the traditional understanding of midlatitude storm formation, 2.) the asymmetry of the distribution of the vertical velocity field which has important implications for the distribution of precipitation and its extremes. In the following, I will start with a brief review of the inherent complexities of moist dynamics and the theoretical framework used throughout this thesis to make sense of them. Then, I will provide a brief introduction into both topics, summarize the existing body of knowledge, identify the research gaps and spell out the specific questions motivating the research in this thesis.

1.1 Why Moist Dynamics is inherently complicated - Intuition and Mathematical Formulation

The presence of moisture renders the dynamics more complicated but also much more interesting due to the inherent nonlinearity that is introduced by the irreversible fallout of condensates during precipitation. Formally, for an air parcel following saturated ascent and conserving its saturated equivalent potential temperature $\frac{D\theta^*}{Dt} = 0$, the Lagrangian rate of change of dry potential temperature $\theta(p, \theta^*)$ can be written as

$$\frac{D\theta}{Dt} = \omega \frac{\partial \theta}{\partial p}\Big|_{\theta^*} + \frac{D\theta^*}{Dt}\frac{\partial \theta}{\partial \theta^*}\Big|_p = \omega \frac{\partial \theta}{\partial p}\Big|_{\theta^*}. \tag{1.1}$$

The dynamics are now greatly complicated when taking moisture into account: whilst moist ascending air releases latent heat upon condensation and feels a locally reduced static stability, the descending air after rainfall is mostly dry and feels the full static

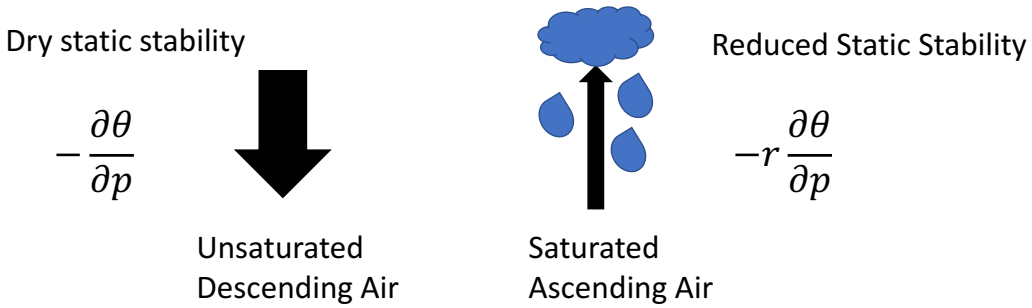

Figure 1-2: Schematic illustrating the additional nonlinearity that is introduced into the thermodynamic equation due to precipitation. Ascending air is moist, condenses, releases latent and feels a reduced static stability $-r\frac{\partial\theta}{\partial p}$, where r is the reduction factor in Eq. (1.4). However, after irreversible fall-out of condensate during precipitation, the descending air is dry and feels the full static stability $\frac{\partial\theta}{\partial p}$. 1.2.

stability (see Fig. 1-2). This introduces an additional nonlinearity into the thermodynamic equation

$$\frac{\partial\theta}{\partial t} + \mathbf{u}\cdot\nabla\theta + r(\omega)\omega\frac{\partial\theta}{\partial p} = 0, \tag{1.2}$$

with

$$r(\omega) = \begin{cases} r, & -\omega \geq 0 \\ 1, & -\omega < 0 \end{cases} \tag{1.3}$$

and

$$r = 1 - \frac{\partial\theta}{\partial p}\Big|_{\theta^*} \Big/ \frac{\partial\theta}{\partial p}, \tag{1.4}$$

is the reduction factor under the assumption of saturated moist-adiabatic ascent.[3] The reduction factor is a three-dimensional field that can be calculated from temperature and pressure. It is generally smallest for the atmosphere at low levels and tends to one with altitude because the static stability becomes closer to dry adiabatic. In the summer or with climate warming, the reduction factor decreases because the midlatitude lapse rate becomes closer to moist-adiabatic (Stone and Carlson 1979).

The nonlinear latent heating term which is introduced by the irreversible fallout of precipitation is the source of much of the complexity and richness of moist dynamics. It is only fully negligible in the dry limit or the limit in which it is always raining (O'Gorman 2011). As a consequence, even in the case of small-amplitude moist motion, Eq. (1.2) becomes advectively linear but remains thermodynamically nonlinear.[4] We re-emphasize that the critical process at the source of the complexity of moist dynamics is not latent heating per se, but the irreversible fallout of precipitation. If latent heating were present but all the condensate retained rather than removed, the dynamics would be analogous to the dry problem with a greatly reduced static stability.

The framework discussed so far goes back to Emanuel et al. (1987) and will be employed throughout this thesis. While it makes simplifying assumptions, such as that ascent is saturated and descent is fully dry and neglects effects like the re-evaporation of rain, we will show throughout this thesis that it can be successfully used to interpret and understand complex simulation and reanalysis data, and to isolate latent heating effects within simple models amenable to theoretical insights.

[3]We show in the appendix A that the reduction factor in Eq. (1.4) can be rewritten with a bit of manipulation as $r = \frac{\theta}{\theta^*}\frac{\Gamma_m}{\Gamma_d}\left(\frac{\partial\theta^*}{\partial p}\right) / \left(\frac{\partial\theta}{\partial p}\right)$, where Γ_d and Γ_m are the dry-adiabatic and moist-adiabatic lapse rates, respectively. This is the form used in the literature (Fantini 1995, Eq. 7) and shown throughout this thesis.

[4]It is possible to consider separately regions of ascent and descent for which $r(w)$ would be linear, but the transition point, which determines the length scale of ascending to descending motion, is a priori unknown and must be found as part of the solution. This leads to nonlinear constraints.

1.2 Diabatic Rossby Vortices: Extratropical Storms with Strong Latent Heating

Different modes of instability and storm formation in the atmosphere can be interpreted elegantly within the potential vorticity (PV) formalism (Hoskins et al. 1985) which we will employ here to review and contrast dry and moist forms of instability and provide intuition for the DRV mechanism. The PV is a particularly useful quantity for understanding atmospheric dynamics since it can be inverted, after specifying appropriate boundary and balance conditions, to fully determine the velocity and temperature field in the atmosphere. Furthermore, it is conserved under frictionless, adiabatic motion and its modification through non-conservative processes such as latent heating thus allows us to understand the fundamental ways in which moist processes affect the large scale flow. As such it has emerged in the literature as an important metric for understanding the role of latent heating in cyclogenesis (e.g. Davis and Emanuel 1991, Wernli et al. 2002, Stoelinga 1996, Ahmadi-Givi et al. 2004).

One of the complexities introduced by latent heating is that it can generate its own 'moist' PV anomalies as distinct from the 'dry' or 'displacement' PV anomalies generated from baroclinic advection (Fig. 1-3a). Dry PV anomalies are typically generated on the model boundaries, where the mean meridional PV gradients are strong. Northward and southward advection against a PV gradient gives rise to anomalies in the form of Rossby wave trains.[5] Moist PV anomalies on the other hand, are generated above and below the latent heating source which is located in the interior of the atmosphere where the meridional PV gradients are weaker. Vertical gradients of the latent heating source are associated with diabatic PV generation which leads to the production of a negative PV anomaly above the heating maximum and a positive PV anomaly below the heating maximum. Moist PV anomalies can

[5]In the real atmosphere, the low level potential vorticity anomalies/gradients correspond to surface temperature anomalies/gradients. However, it can be shown that these are mathematically equivalent to potential vorticity anomalies/gradients above the boundary (Bretherton 1966). This makes it possible to present a unified framework of instability in terms of PV.

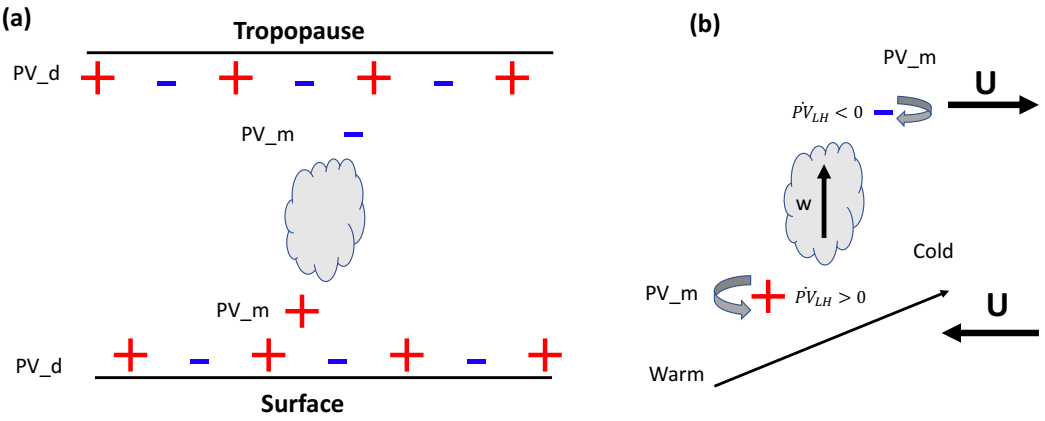

Figure 1-3: (a) Schematic of the model troposphere that contains dry PV anomalies ($\mathrm{PV_d}$) from baroclinic advection close to the surface and tropopause where meridional PV gradients are strong, and moist PV anomalies ($\mathrm{PV_m}$) generated by latent heating in the interior of the atmosphere - negative above the heating source and positive below the heating source. (b) Schematic of the growth mechanism of the Diabatic Rossby Vortex: two moist PV anomalies are maintained through PV generation from latent heating $\dot{PV}_{LH}$ against a shear flow $-U$ and U, that is in thermal wind balance with a meridional temperature gradient. As a result they can interlock and grow.

then begin to interact with each other or with dry PV anomalies giving rise to a rich class of moist baroclinic disturbances that are not accounted for in dry models and theories. [6]

A mode of interaction involving two moist PV anomalies, positive below and negative aloft, driven entirely by latent heating rather than baroclinic processes, has received special attention in the literature on moist baroclinic instability due to its ability to self-amplify without upper level forcing (Snyder and Lindzen 1991, Parker and Thorpe 1995, Whitaker and Davis 1994, Moore and Montgomery 2004, Oda and Kanehisa 2011). The growth mechanism is illustrated in Fig. 1-3b. Cyclonic flow around the low level positive PV anomaly, embedded in a meridional temperature gradient that has temperature decreasing poleward, leads to warm air advection east of the low level positive PV anomaly. This leads to ascent east of the positive PV anomaly and west of the negative PV anomaly. In the presence of sufficient moisture,

[6]The terminology of 'dry' and 'moist' anomalies follows loosely that of De Vries et al. (2010). It should be noted however, that in the presence of nonlinear heating a simple decomposition of PV into a dry and moist component, as the authors did, is no longer possible. A mathematically precise classification of all the different modes of interactions thus remains an outstanding problem of moist dynamics, and the field has worked with heuristic classifications instead.

condensation occurs upon ascent, which releases latent heating. Latent heating induces a positive PV tendency to the east of the positive PV anomaly below the heating maximum, and a negative PV tendency to the west of the negative PV anomaly above the heating maximum. This allows the PV anomalies to counterpropagate against the background flow, phase lock, and self-amplify optimally in the configuration in which the induced meridional velocities by both anomalies overlap between each other to generate maximum meridional advection and hence maximum ascent and diabatic PV generation. We note that the disturbance has been drawn in a frame in which it is stationary. If we were to translate to a realistic background flow that is eastward in both layers, the disturbance would propagate eastward at a speed larger than the ambient flow due to the re-generation of positive PV east of the low level anomaly.

Because of the nonlinearity of latent heating, i.e. no latent cooling in the area of descent west of the positive anomaly and east of the negative anomaly, no negative PV anomaly is generated in the lower layer and no positive PV anomaly in the top layer. Unlike baroclinic advection which has a tendency to produce wave-like anomalies from northward and southward advection (illustrated by the Rossby wavetrains at the tropopause and surface in Fig. 1-3a), latent heating thus has a tendency to produce isolated solutions (illustrated by the isolated moist PV cloud tower in Fig. 1-3a). Due to the diabatic character of the disturbance and its isolated nature, this mode of interaction has been called the 'diabatic Rossby Vortex', or short DRV (Moore and Montgomery 2004, Moore and Montgomery 2005, O'Gorman et al. 2018). Because positive diabatic generation of PV east of the low level anomaly plays the surrogate role of meridional advection in a classic Rossby wave, such disturbances are also known as 'diabatic Rossby waves', or short DRWs, in the literature (Parker and Thorpe 1995, Boettcher and Wernli 2013). However, both terminologies refer to the same diabatically driven phenomena (Boettcher and Wernli 2013).[7]

In this thesis, we will refer to it as DRV to emphasize the isolated character of the solution which also helps to distinguish it most clearly from moist baroclinic waves

[7]It is worth noting that the short-hand 'DRV' is easier to pronounce and use in spoken English than 'DRW', whereas 'DRW' is easier to pronounce and use in spoken German than 'DRV'. This might be another reason for why both terminologies remain in use.

(see Fig. 1 and 2 in O'Gorman et al. 2018). Moist baroclinic waves were described theoretically using a two-layer Phillip's model with nonlinear heating at the interface by Emanuel et al. (1987). The authors derived analytical expressions for the growth rate and length scale as a function of r. They showed that latent heating increases the growth rates and decreases the ascent length of dry waves in the Phillip's model. Crucially however, the solutions in the presence of latent heating remain periodic waves with smaller ascent, than descent length. In terms of our diagram (Fig. 1-3a), this can be intuited by the fact that for a moist two-layer Phillip's model dry and moist PV anomalies occur in the same layer by construction and so PV anomalies receive contributions from both baroclinic and latent heating effects. This disrupts the pure moist-moist interaction mechanism and the tendency to produce isolated solutions, although the precise conditions under which solutions transition between moist-baroclinic waves and DRV modes remains unaddressed in the literature.

We also emphasize the isolated character of the disturbance to point out that existing analytical theories for moist-moist interactions that are based around linearizations of the heating term for simplicity, can only represent a first step towards a more complete understanding (Snyder and Lindzen 1991, Oda and Kanehisa 2011). These studies elegantly demonstrated the possibility of growth through moist disturbances alone by considering a free-shear flow in which the dry instability mechanism is removed. However, the latent heating parametrization prescribed is unphysical and they did not obtain isolated solutions as a result. In the case of Oda and Kanehisa 2011, the analytical solutions for the modes also suffer from the well-known problem that if the static stability is reduced everywhere, and not just conditionally in ascent areas, the growth rates for the most unstable modes become infinite in the limit of strong latent heating $r \to 0$ as pointed out by Emanuel et al. (1987). Reduction of the static stability in updrafts only is crucial for obtaining finite growth rates in the limit of strong latent heating. As such an analytical theory for the growth rate and length scale of DRV modes in the presence of nonlinear heating is currently missing from the literature.

DRVs have now been studied and found in a range of different models and ob-

servation. They were first identified in certain parameter ranges of the moist-Eady model with nonlinear heating as a new mode of instability which could self-intensify diabatically without interaction with an upper level disturbance (Montgomery and Farrell 1991, Montgomery and Farrell 1992, Whitaker and Davis 1994, Moore and Montgomery 2004). Subsequent studies with a mesoscale model showed that the mechanism of diabatic generation could spin up isolated dipole towers of PV starting from an environment that is sufficiently moist and baroclinic without upper level forcing (Moore and Montgomery 2005). On the observational side, DRVs were shown to be implicated in case studies of strong cyclogenesis along the east coast of the US and the west coast of Europe causing significant destruction to property and human life (Wernli et al. 2002, Moore et al. 2008). These storms served as catalysts for more extensive climatological studies that used a tracking algorithm, enforcing sufficient baroclinicity, moisture, absence of upper level forcing, and rapid propagational speed, to systematically identify and examine DRVs (Boettcher and Wernli 2013, Boettcher and Wernli 2015). DRVs were found to occur in all ocean basins and seasons, at a rate of roughly 10 systems per month in the Northern and 4 systems per month in the Southern Hemisphere with more DRVs in summer than in winter in both hemispheres. Two DRVs that were identified in the North Atlantic by the tracking algorithm of Boettcher and Wernli (2013) for an updated climatology based on ERA5 reanalysis, are visible in cloud satellite imagery shown in Fig. 1-1. They spun out of a strong cloud zone off the coast of Florida one day apart. The first one tracked more zonally towards Europe, and the second one more meridionally along the east coast of the US. Recently, calculations of moist baroclinic instability over a range of different climates in an idealized GCM showed that the most unstable modes of baroclinic instability transitioned from quasi-periodic waves to isolated DRV solutions in warming climate (O'Gorman et al. 2018). The break-up of the quasi-periodic modes of instability was found to occur at a midlatitude surface air temperature of 292K which is close to Earth's temperature in midlatitude summer. An increase in the importance of latent heating effects on extratropical eddies is expected under global warming since atmospheric moisture content increases strongly with temperature due

to the Clausius-Clapeyron relationship (Schneider et al. 2010). The transition to DRV modes of instability thus point to the profound modifying effect that latent heating has on the structure of rapidly growing eddies in a warming climate.

It is clear from the literature that DRVs are isolated disturbances that are spawned in moist-baroclinic environments and can rapidly intensify from latent heating without the presence of upper level forcing. While we have a good theoretical understanding of dry cyclogenesis both in terms of simple analytical models of baroclinic instability (Eady 1949, Phillips 1954, Charney 1947) and PV dynamics of storms at finite amplitude (Davis and Emanuel 1991), our understanding of DRV formation and propagation, the controls on their growth rates and length scales, and the transition from moist-baroclinic wave to isolated DRV solutions is poor. Developing an equivalent conceptual understanding for DRVs is therefore critical and one of the major objectives of this thesis.

1.3 Asymmetry of the Vertical Velocity Distribution in Moist Macroturbulence

Another effect of latent heating is to break the symmetry between upward and downward motion, making upward motion stronger than downward motion and by mass continuity shrinking updraft area compared to downdraft area. A snapshot of a typical vertical velocity profile in the midlatitudes, showing stronger upward than downward motion is shown in Fig. 1-4.

The asymmetry of the vertical velocity distribution has important implications for the distribution of precipitation and its extremes because precipitation is a strong function of vertical motion. The asymmetry also directly enters the definition of the 'effective static stability' of O'Gorman (2011), which has been successfully used in recent years to reason about the effects of latent heating in a range of dynamical problems from cyclone deepening rates, Hadley cell extent, and Eliassen-Palm fluxes simply by replacing the dry static stability by the effective static stability in moist

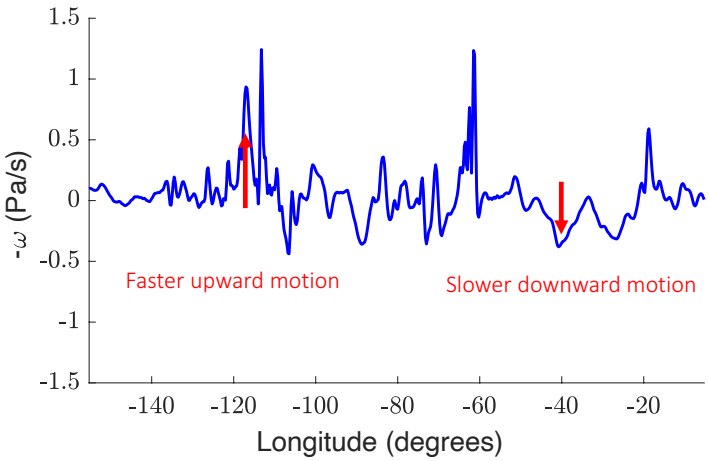

Figure 1-4: Vertical velocity $-\omega$ at 45°N and 500hPA from ERA5 on June 2nd, 2017 showing that upward motion are typically stronger than downward motion.

theories (O'Gorman 2011, Levine and Schneider 2015, Booth et al. 2015, Pfahl et al. 2015, Dwyer and O'Gorman 2017). While the effective static stability has proven to be a useful tool, it it not a closed theory of moist dynamics. Its definition depends on the asymmetry which is not known a priori and must be inferred in practice from simulation output or reanalysis.

In order to be able to understand the distribution of precipitation extremes and to reason about important changes to the general circulation under climate change using the effective static stability, we are thus led to the fundamental question of what sets the vertical velocity asymmetry and how much does it change with warming. Recent simulations with an idealized GCM have shown that the increase in asymmetry under warming is much smaller in the macroturbulent regime than for the modes of moist baroclinic instability (O'Gorman et al. 2018). This distinction is significant since the atmosphere is constantly in a state of moist macroturbulence, but scalings for moist baroclinic modes have formed the basis for understanding skewness changes with warming in the literature (Pendergrass and Gerber 2016). While we can use moist baroclinic instability theory (Emanuel et al. 1987, Zurita-Gotor 2005) to understand changes in the asymmetry in the modal regime, a theory for the asymmetry that is reached in the macroturbulent state of the flow is currently missing from the literature. This is one of the major objectives of my thesis.

1.4 Thesis Outline

In chapter 2, a simple moist 2-layer QG model without PV gradients is introduced and shown to capture an isolated DRV mode. The dispersion relation for the growth rate and length scales of the DRV mode is derived analytically retaining the full complexity of a nonlinear heating term. Asymptotic solutions are found in the limit of a convectively neutral stratification and comparisons are made to the results for dry and moist-baroclinic waves. The most unstable mode when PV gradients are reintroduced into the moist 2-layer model is calculated for varying strength of the latent heating and the meridional PV gradients and a phase diagram is created for when the most unstable modes are isolated DRVs versus moist baroclinic waves. A simple PV argument is introduced that explains the conditions under which a wave to vortex mode transition occurs. We conclude by making comparisons between the PV structure of DRV modes to DRV storms at finite amplitude and use a generalized PV tendency to relate the PV structure and PV tendency in observed storms.

In chapter 3, we apply inversions of a moist QG omega equation with reduced stability parametrization to the idealized GCM runs of O'Gorman et al. (2018) to assess the contributions to the asymmetry of the vertical velocity distribution coming from the dynamical forcing on the right-hand side of the moist omega equation versus the reduction in moist static stability in the modal versus the macroturbulent regime. We show that in the modal regime both dynamical forcing and a reduction in moist static stability contribute to the asymmetry whereas in the macroturbulent regime the reduction in moist static stability primarily contributes to the asymmetry. The dynamical forcing becomes practically unskewed. We then distill the results of the inversions into a toy-model of the macroturbulent asymmetry that is solved for a given reduction factor and wavenumber of the dynamical forcing to reproduce the slow change of the asymmetry over the seasonal cycle in reanalysis and with global warming in idealized simulations. Consistent with the toy-model predictions we show using simulations of moist QG turbulence, that high asymmetry states are still possible even when the dynamical forcing is unskewed provided that the wavenumber of the

dynamical forcing is sufficiently large. We show that in this regime the flow can be characterized as a DRV world.

In chapter 4, we return to DRVs and study their dynamics in turbulent simulations of the moist quasigeostrophic and moist primitive equations to better understand the role that finite amplitude effects have on the dynamics of individual storms and the character of the macroturbulent simulations. Higher order effects are then distilled into a 1d model that is solved for a small and high Rossby number and a current and warm climate configuration to reproduce much of the observed PV structure of DRV modes and DRV storms.

In chapter 5, we summarize the findings of this thesis and discuss their implications and future work.

Chapter 2

The Diabatic Rossby Vortex: Growth Rate, Length Scale and the Wave-Vortex Transition

Abstract

In idealized simulations of moist baroclinic instability on a sphere, the most unstable mode transitions from a periodic wave to an isolated vortex in sufficiently warm climates. The vortex mode is maintained through latent heating and shows the principle characteristics of a diabatic Rossby vortex (DRV) which has been found in a range of different simulations and observations of the current climate. Currently, there is no analytical theory for DRVs or understanding of the wave-vortex transition that has been found in warmer climates. Here, we introduce a minimal moist two-layer quasigeostrophic model with tilted boundaries capable of producing a DRV mode, and we derive growth rates and length scales for this DRV mode. In the limit of a convectively-neutral stratification, the length scale of ascent of the DRV is the same as that of a periodic moist baroclinic wave, but the growth rate of the DRV is 54% faster. We explain the isolated structure of the DRV using a simple potential vorticity (PV) argument, and we create a phase diagram for when the most unstable solution is a periodic wave versus a DRV, with the DRV emerging when the moist static stability and meridional PV gradients are weak. Finally, we compare the structure of the

[1]This chapter has been published as Matthieu Kohl and Paul A. O'Gorman (2022). The Diabatic Rossby Vortex: Growth Rate, Length Scale, and the Wave–Vortex Transition, Journal of the Atmospheric Sciences, 79(10), 2739-2755 and is reproduced here with slight adaption.

DRV mode to DRV storms found in reanalysis and to a DRV storm in a warm-climate simulation.

2.1 Significance Statement

Past research has identified a special class of midlatitude storm, dubbed the Diabatic Rossby Vortex (DRV), which derives its energy from the release of latent heat associated with condensation of water vapor, and as such goes beyond the traditional understanding of midlatitude storm formation. DRVs have been implicated in extreme and poorly predicted forms of cyclogenesis along the east coast of the US and the west coast of Europe with significant damage to property and human life. The purpose of this study is to develop a mathematical theory for the intensification rate and length scale of DRVs in order to gain a deeper understanding of the dynamics of these storms in current and future climates.

2.2 Introduction

In small-amplitude calculations of moist baroclinic instability over a wide range of climates in an idealized GCM, O'Gorman et al. (2018) found that the most unstable mode transitions from a quasi-periodic wave to an isolated vortex at a midlatitude surface air temperature of roughly 292K.[2] The structure of the vortex mode that emerged in warm climates (Fig. 2-1a) consists of a dipole of interlocking potential vorticity (PV) anomalies above the boundary layer: cyclonic in the lower free troposphere and anticyclonic in the upper troposphere. Warm air advection to the east of the cyclonic anomaly and to the west of the anticylonic anomaly leads to ascent and diabatic PV generation from latent heat release in the form of a dipole. We note that because the mode is found for warm-climate simulations, the diabatic generation extends higher in the atmosphere than it would in the current climate.

[2]The most unstable modes were calculated in O'Gorman et al. (2018) through repeated rescaling of perturbations to small amplitude, assuming upward motion to be saturated, and using a basic state equal to the zonal and time-mean of a fully nonlinear simulation for that climate.

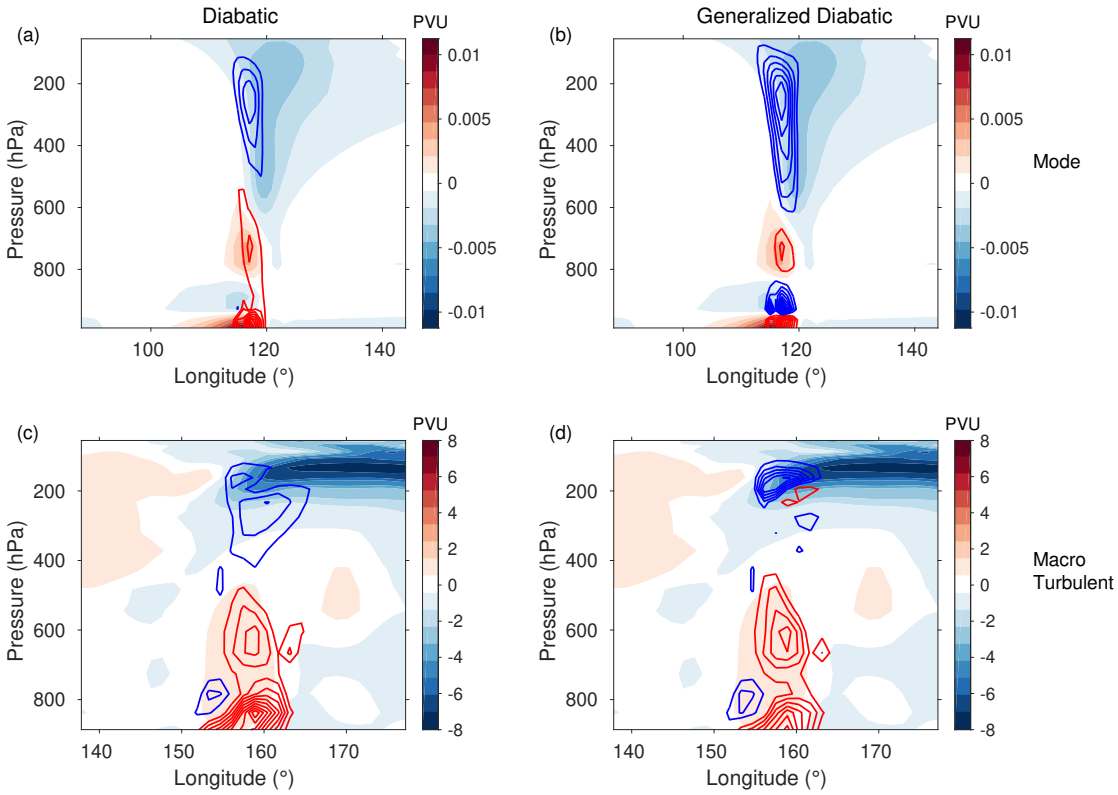

Figure 2-1: PV anomalies (shading) and diabatic generation of PV due to latent heating (contours) for (a) the DRV mode at latitude 44° in a calculation of small-amplitude moist baroclinic instability on a sphere in a warm climate (global mean surface temperature 311 K) using an idealized GCM (O'Gorman et al., 2018), and (c) a DRV storm at latitude 61° in the corresponding macroturbulent (i.e., finite amplitude) simulation at statistical equilibrium in the same GCM. (b,d) are the same as (a,c) except that they show the generalized diabatic generation of PV calculated according to Eq. (2.29) which includes both diabatic PV generation and diabatic vertical advection of PV, where the only diabatic process considered is latent heating. Potential vorticity (PV) is calculated using the hydrostatic approximation to Ertel's PV, and PV anomalies are with respect to the zonal mean. The contour interval is 9.2×10^{-5} pvu h^{-1} in (a,b) and 0.07 pvu h^{-1} in (c,d). The zero contour is not plotted. Note that since the DRV mode in (a,c) was calculated using repeated rescaling of amplitude, the overall amplitude of its fields are arbitrary.

The constellation of PV anomalies and diabatic PV generation is such that the anomalies are amplified and maintained against the background shear flow. The resulting vortex mode bears the principle characteristic of a diabatic Rossby vortex (DRV) which has been found in a range of different simulations and observation. Its emergence as the fastest growing mode within the moist baroclinic instability calculations of O'Gorman et al. (2018) points to the profound modifying influence that latent heating has on the structure of fast growing disturbances in a warming climate.

DRVs first emerged as an alternative mode of instability in idealized studies of moist baroclinic instability. The presence of moisture greatly enriches the dynamics of unstable modes due to the fact that condensation and precipitation are strongly associated with ascending but not descending motion, and hence an additional nonlinearity is introduced into the thermodynamic equation (O'Gorman, 2011). Emanuel et al. (1987) represented condensational heating in Eady and two-level semi-geostrophic models by assuming saturated moist-adiabatic ascent. This assumption leads to a nonlinear factor $r(w)$ that is a function of the vertical velocity w and reduces the potential vorticity (or static stability in quasigeostrophic (QG) models) by a factor $r < 1$ in updrafts while leaving it unchanged in downdrafts ($r = 1$). While this parameterization is a simplification, it captures the essential asymmetry that is introduced through the irreversible fall-out of condensate during precipitation, and r may be calculated from the observed temperature and pressure distributions in the atmosphere. The effect of this condensational heating was to increase the growth rates and decrease the area of ascent of growing modes with respect to dry waves, results that are borne out well by moist baroclinic life cycle studies with shallow water models (Lambaerts et al., 2012) or more comprehensive forecasting models (Booth et al., 2015). When moist instability calculations were done with a more realistic reduction factor $r(z)$ that varied vertically, the short wavelength cut-off of the Eady model disappeared (Whitaker and Davis, 1994; Moore and Montgomery, 2004). A new mode of instability emerged at shorter wavelengths which could intensify without the presence of upper level forcing (Montgomery and Farrell, 1991, 1992; Whitaker

and Davis, 1994; Moore and Montgomery, 2004). This mode now grew through the interaction of a surface potential temperature anomaly and an interior PV anomaly, rather than primarily through an interaction of anomalies of potential temperature at the surface and lid, and the budget of eddy available potential energy was dominated by diabatic rather than baroclinic generation.

Subsequent three-dimensional simulations with a mesoscale model by Moore and Montgomery (2005) showed that this alternative diabatic growth mechanism could generate isolated coherent PV-dipole structures consisting of a phase locked low-level cyclonic anomaly and a midtropospheric anticyclonic anomaly starting from an initial moist baroclinic environment without upper level forcing. The isolated and diabatic character of such a growing disturbance without upper level forcing led Moore and Montgomery (2004) to classify it as 'Diabatic Rossby Vortex' (DRV) - a term we adopt in this paper. More recently, idealized channel simulations of cyclone development using a weather forecasting model (Tierney et al. 2018) showed signs of break-up into "jagged diabatic" PV structures reminiscent of a DRV at sufficiently warm temperatures, in line with the results of O'Gorman et al. (2018). Finally, going beyond initial value problems, turbulent simulations on a beta plane using moist two-layer QG or shallow water equations showed a transition from a smooth large-scale jet flow, to a jet-flow disrupted by the presence of small-scale vortices, that rapidly intensify through moist-dynamical feedbacks in the strongly precipitating regime of the simulation (Lapeyre and Held 2004,Bembenek et al. 2020). In Bembenek et al. (2020) these vortices were explicitly likened to DRVs. We have also found growing DRVs in the fully nonlinear warm-climate simulations of O'Gorman et al. (2018). An example of such a DRV is shown in Fig. 2-1c, and it exhibits considerable similarity with the DRV mode calculated by repeated rescaling to small amplitude (Fig. 2-1a), although the positive PV anomaly extends higher into the atmosphere and the negative PV anomaly and diabatic PV generation are more concentrated at the upper tropopause.

DRVs have also been invoked to account for the initial phase prior to explosive growth of certain cyclones in in operational analyses and realistic simulations. Both

the European extreme storm 'Lothar' in 1999 (Wernli et al. 2002) and the explosive east-coast winter storm in 2005 (Moore et al. 2008) were shown to propagate and intensify moderately through diabatic effects without upper level forcing before intensifying explosively through upper-level interactions in a secondary growth process. In this paper, we will remain focused on the initial phase of diabatic self-amplification/propagation without considering upper interactions. While the isolated and vortical structure of the east-coast winter storm led Moore et al. (2008) to classify it as a DRV following the terminology of Moore and Montgomery (2004), the rapid propagational character of 'Lothar', faster than the ambient winds, led Wernli et al. (2002) to classify it as a 'Diabatic Rossby Wave' (DRW) with the positive diabatic PV generation to the east of the low level cyclonic PV anomaly playing the role of meriodional PV advection in a classic dry Rossby wave as discussed in Parker and Thorpe (1995). Both DRV and DRW refer to the same phenomena, but neither name is fully satisfactory since such storms are isolated like vortices but propagate through PV generation like a wave (Boettcher and Wernli, 2013). The upper-level negative PV anomaly is found to be relatively weak in observed storms, and some uncertainty exists in the literature as to when latent heating leads to growth through interaction of the positive low-level PV anomaly with a self-induced negative upper PV anomaly, or rather just leads to propagation of the low-level PV anomaly. The importance of diabatic effects in individual case studies of rapid cyclogenesis, led Boettcher and Wernli (2013) to study DRVs more systematically by compiling a 10-year (2001-2010) climatology of DRV tracks for the North Pacific and North Atlantic. DRVs occurred at an average rate of 81 systems per year over the North Pacific and 43 system per year over the North Atlantic. In line with the case studies of 'Lothar' and the east-coast winter storm, DRVs in the current climate were found to propagate with moderate intensification before interacting in a second phase with a pre-existing upper level PV anomaly or jet stream.

It is clear from the literature that DRVs constitute an alternative diabatic growth mechanism that relies both on sufficient baroclinicity and moisture, and which produces relatively small scale modes that can self-amplify exponentially even without

the presence of upper level forcing. Currently, there is no theory for the growth rate and length scale of DRVs or the wave-vortex transition that occurs at higher temperatures in moist baroclinic instability simulations. Analytically tractable models of dry and moist baroclinic instability (Eady, 1949; Charney, 1947; Phillips, 1954; Emanuel et al., 1987; Zurita-Gotor, 2005) form much of the basis of our theoretical understanding of cyclones due to their ability to isolate the mechanism of cyclone formation in a conceptually simple model and to relate growth rate and length scale of cyclones to atmospheric parameters in a quantitative way. Given the importance of diabatic effects in cyclogenesis both in the current and future climate, it seems desirable to develop an equivalent conceptually simple model for a DRV.

To this end, we introduce in this paper a minimal moist two-layer QG model with tilted upper and lower boundaries and show that it is capable of producing a DRV mode. Latent heating is represented by an assumption of saturated ascent in updrafts following previous work (Emanuel et al., 1987; Fantini, 1995; Zurita-Gotor, 2005). We tilt the model boundaries at a slope equal to that of the mean isentropes to make the two-layer model an analog of the interior of the Eady model in which dry-baroclinic instability has been shut off but any moist instability retained. This allows us to transition to a pure DRV solution within a conceptually simple model. We note that this model is similar in spirit to the unbounded balanced shear flow studied by Snyder and Lindzen (1991) to demonstrate the possibility of growth through diabatically generated interior anomalies in a setup which is dry modally stable. However, Snyder and Lindzen (1991) allowed for negative latent heating in descent regions and so obtained periodic wave solutions rather than an isolated DRV.

We begin in section 2.3 by formulating the tilted two-layer model and showing that it produces a DRV mode. We then study its PV budget and derive the dispersion relation of the DRV mode analytically, a significant novelty of this paper. Asymptotic solutions for the growth rate and ascent area of the DRV are found in the limit of small r. We also solve the dispersion relation for the infinite domain numerically by root-finding for the whole range of r. In section 2.4, we study the emergence of DRV modes in the more general case that includes non-zero meridional

PV gradients. We first introduce a simple PV argument to explain the wave-vortex transition observed to occur as latent heating becomes dominant in the moist baroclinic instability simulations of O'Gorman et al. (2018). We then generate a phase diagram for when the most unstable mode in a partially tilted two-layer model is a periodic wave versus a DRV as a function of the PV gradients and r. In section 2.5, we compare the warm-climate DRV mode and DRV storm from the idealized GCM simulations of O'Gorman et al. (2018) to two storms in the present climate that have been previously been found to have the characteristics of DRVs. Lastly, in section 2.6 we summarize our results and discuss their implications.

2.3 A Simple Model for a DRV

2.3.1 Model formulation

We seek a minimal model that can capture the internal interactions of diabatically generated PV anomalies characteristic of a DRV. We start from the moist quasi-geostrophic equations on an f-plane:

$$\partial_t \nabla^2 \psi + J(\psi, \nabla^2 \psi) - f w_z = 0, \tag{2.1}$$

$$\partial_t \psi_z + J(\psi, \psi_z) + \frac{N^2}{f} r(w) w = \frac{N^2}{f} \overline{r(w) w}, \tag{2.2}$$

where ψ is the streamfunction, w is the vertical velocity, N^2 is the constant static stability, f is the Coriolis parameter, $J(A, B) = A_x B_y - B_x A_y$ is the Jacobian, and $\overline{(...)}$ is a horizontal domain average. Equations (2.1,2.2) are equivalent to Eqs. 16 and 17 of Fantini (1995) except for the addition of the the term $\frac{N^2}{f}\overline{r(w)w}$ on the right hand side of the thermodynamic equation Eq. (2.2) which acts as a spatially uniform radiative cooling to ensure that the domain-mean temperature remains constant even though there is latent heating. The effects of latent heating on the dynamics are encapsulated in the spirit of simple moist theories (Emanuel et al., 1987; Fantini,

1995) by the nonlinear factor

$$r(w) = \begin{cases} r, & w \geq 0 \\ 1, & w < 0 \end{cases} \tag{2.3}$$

which reduces the static stability by a factor r in regions of ascent. Under an assumption of saturated moist-adiabatic ascent, $r = \frac{\theta}{\theta^*}\frac{\Gamma_m}{\Gamma_d}\left(\frac{\partial\theta^*}{\partial z}\right) / \left(\frac{\partial\theta}{\partial z}\right)$ (see Eq.(7) of Fantini 1995), where θ and θ^* are the potential and saturated equivalent potential temperature, respectively, and Γ_d and Γ_m are the dry-adiabatic and moist-adiabatic lapse rates, respectively. The reduction factor in the ascent region varies strongly in the vertical. In cyclones with strong diabatic heating, r can go all the way to zero in the interior and tend towards 1 as the tropopause is reached. Averaged in the vertical, $r = 0.1$ is a typical value for the current climate (global mean surface temperature of 288K) and $r = 0.01$ for the warm climate GCM simulations (global mean surface temperature of 311K) in O'Gorman et al. (2018). Physically the nonlinear factor $r(w)$ represents the fact that whilst moist ascending air releases latent heat upon condensation and feels a locally reduced static stability, the descending air is subsaturated (after irreversible fall-out of condensate by precipitation) and thus feels the full static stability. Moist thermodynamics thus introduces an additional nonlinearity into the equations which greatly enriches the dynamics.

We simplify the dynamics further by discretizing the equations in the vertical into two equal layers of height (Fig. 2-2), anticipating that the two layers will be sufficient to represent the PV-dipole structure of the DRV. We introduce a barotropic stream function $\phi = \frac{\psi_1+\psi_2}{2}$ and a baroclinic stream function $\tau = \frac{\psi_1-\psi_2}{2}$ where 1 refers to the upper layer and 2 refers to the lower layer. The layer interface height is $\eta = -\frac{f}{g'}(\psi_1 - \psi_2)$, with $g' = g\frac{\theta_1-\theta_2}{\theta_0}$ where g is the gravitational constant, θ_1 and θ_2 are potential temperatures in each layer, and θ_0 is a reference potential temperature.

We assume small perturbations about a basic state $\tau_0 = -Uy$ corresponding to a flow $u_1 = -\psi_{1y} = U$ in the upper layer and $u_2 = -\psi_{2y} = -U$ in the lower layer. The small amplitude of the perturbations allow us to linearize the advection terms, but

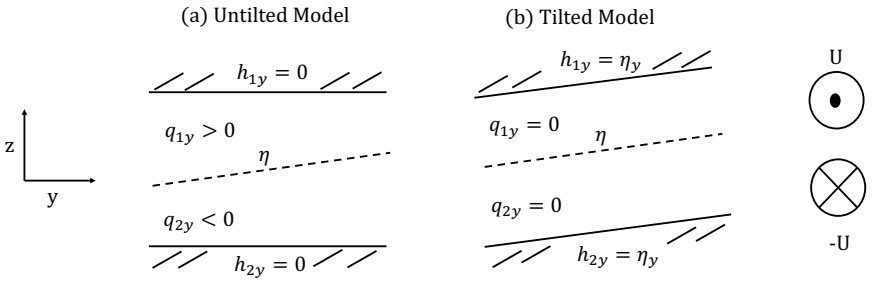

Figure 2-2: Schematic of the (a) untilted and (b) tilted two-layer model with basic-state interface height η, boundary slopes $h_{1y} = h_{2y} = \eta_y$, and basic-state PV-gradients q_{1y} and q_{2y}. Also shown is the basic-state zonal wind profile which is the same for the tilted and untilted models.

the thermodynamic equation remains nonlinear because of the latent heating term.

Finally, the key novelty of our model is that we tilt the top and bottom boundaries, $h_1(y)$ and $h_2(y)$, respectively, to have slopes in the meridional direction of $h_{1y} = h_{2y} = \eta_y = -\frac{2f}{g'}\tau_{0y}$ so as to match the slope of the basic-state layer interface η (Fig. 2-2b) in contrast to the standard untilted two-layer model (Fig. 2-2a). This makes our two-layer model an analogue of the interior of the Eady-model with zero meridional PV-gradients $q_{1y} = q_{2y} = 0$ in the basic state. The dry modal instability through interlocking Rossby-waves is thus shut-off, but any instability solely due to the moist processes is retained. The equations for the perturbations about the basic state are derived in section a of the appendix in the limit of small-amplitude perturbations and are given here in nondimensional form:

$$\partial_t \phi_{xx} + \tau_{xxx} - \tau_x = 0, \tag{2.4}$$

$$\partial_t \tau_{xx} + \phi_{xxx} - \phi_x + w = 0, \tag{2.5}$$

$$\partial_t \tau - \phi_x + r(w)w = \overline{r(w)w}, \tag{2.6}$$

where τ, ϕ and w are now perturbations about the basic state.[3] Finally, we note

[3]Equations (2.4-2.5) are identical to the two-layer moist QG equations (Zurita-Gotor, 2005) except for the addition of the terms $-\tau_x$ and -ϕ_x in Eq. (2.4) and Eq. (2.5), respectively, which arise because of the tilted boundaries, and except for the presence of the mean radiative cooling term $\overline{r(w)w}$ in Eq.2.6. Zurita-Gotor (2005) studied the stability of moist waves by combining the equations into a single equation for w in which case any mean radiative cooling term drops out for an untilted model. We will see shortly, however, that the mean radiative cooling does not drop out when forming the w equation for the tilted model.

that a dry two-layer model with sloping upper and lower boundaries was already introduced by Bretherton (1966) to allow independent variation of PV gradients and vertical shear in an investigation of the short-wavelength cut-off of baroclinic instability. Evidently, the reason for introducing the tilted boundaries here is different, as we are interested in eliminating the basic-state PV gradients all together.

2.3.2 Numerical Simulation

We first solve the tilted model equations numerically to isolate and study the fastest growing mode for a given static-stability reduction factor $0 \leq r \leq 1$. To this end, we discretize the equations using second-order central finite differences in a periodic domain in x.

We integrate the barotropic and baroclinic vorticity equations (Eqs. 2.4,2.5) forward in time for the variables $\Phi = \phi_{xx}$ and $T = \tau_{xx}$. Timestepping is performed with matlab's ode45 function, which is based on an explicit Runge-Kutta (4,5) formula with an adaptive time step.

The system of equations is closed by calculating the vertical velocity w at each time step from the nonlinear omega equation,

$$(r(w)w)_{xx} - w = 2\phi_{xxx} - \phi_x, \tag{2.7}$$

which is formed by eliminating the time derivatives between Eq. (2.5) and (2.6). By using the omega equation, time stepping of Eq. (2.6) is not needed. The nonlinearity in the omega equation arises from $r(w)$ and requires an iterative approach to finding the solution. We solve it iteratively at each time step as $(r(w^n)w^{n+1})_{xx} - w^{n+1} = RHS$, where n is the iteration step. We start the iteration from a random guess for w to define the initial $r(w)$, and we iterate until the root-mean-square (rms) of $(w^{n+1} - w^n)$ is smaller than 10^{-12}.

We start the timestepping from random initial conditions for Φ and T. At each time step, we invert $\Phi = \phi_{xx}$ and $T = \tau_{xx}$ to obtain ϕ and τ by imposing that ϕ and τ have zero mean. We then solve for w using the iterative approach to the

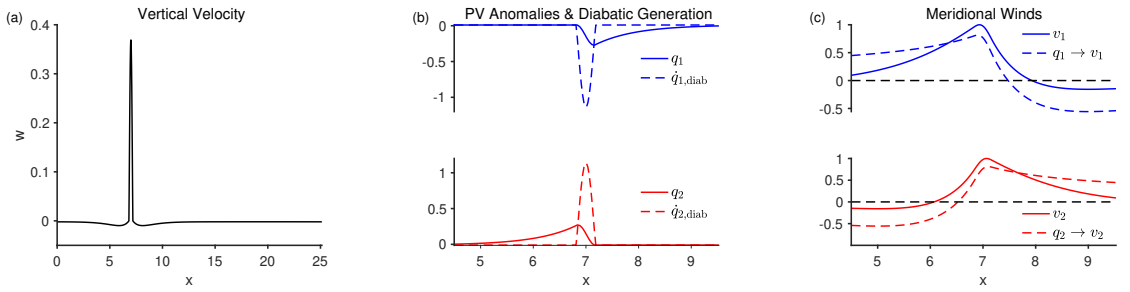

Figure 2-3: (a) Vertical velocity, (b) PV anomalies (solid) and diabatic PV generation rate (dashed), and (c) total meridional winds (solid) and meridional winds induced by PV anomalies in the same layer (dashed). All quantities are plotted versus x for the fastest growing mode of the tilted model equations at $r = 0.01$ which is a DRV. In (b-c), quantities in the upper layer are show in blue and quantities in the lower layer are shown in red. The domain size is $L = 8\pi$ and the grid spacing is $\Delta x = 0.025$. All quantities are non-dimensional and the overall magnitude of the DRV is arbitrary. The results in (b,c) have been zoomed in around the location of ascending motion to better show the structure of the fields since the DRV occupies only a small fraction of the domain.

omega equation described above, and we then update Φ and T using Eqs. (2.4) and (2.5). We rescale the amplitudes of the vectors Φ and T by a factor of 100 each time $\mathrm{rms}(\mathbf{x}) > 10$, where $\mathbf{x} = [T, \Phi]$, to avoid large numbers which could cause problems with the numerical representation. We integrate until the nondimensional time is $t = 200$ when we find that the solution has converged to a normal mode.

The vertical velocity (at time $t = 200$) for $r = 0.01$ is shown in Fig.2-3a where we have used a grid spacing of $\Delta x = 0.025$ and a domain size of 8π . Remarkably, the solution evolves into a DRV with a single spatially localized peak in vertical velocity just like in the warm limit of the idealized GCM calculations of O'Gorman et al. (2018), their Figs. 1f and 2f. The isolated solution is in stark contrast to the spatially periodic structure of moist baroclinic waves. The solution is exponentially growing and fixed in space because the basic-state zonal wind is equal and opposite in each layer, but the DRV would propagate zonally with a more realistic vertical wind profile. We have repeated the calculations using a linear drag on the relative vorticity in the lower layer with a damping time scale of either 10 days (weak drag) or 2.5 days (strong drag). Isolated DRV solutions persist even with drag included, with similar length scale but reduced growth rate compared to the default case with

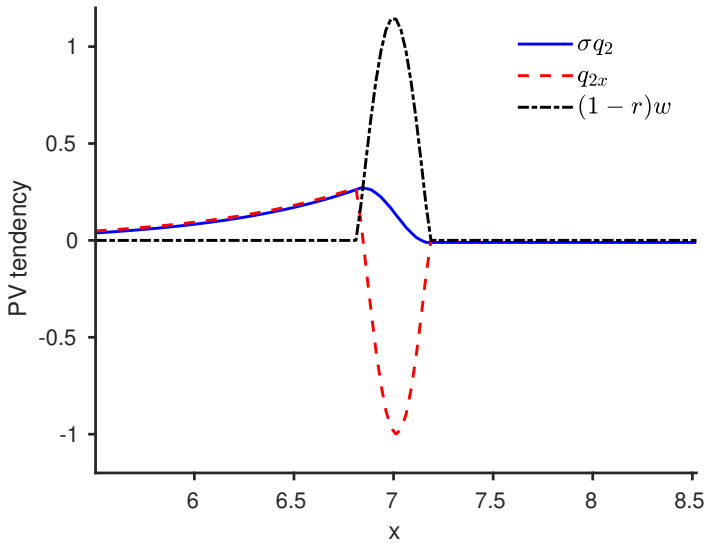

Figure 2-4: Terms in the lower-layer PV budget versus x for the fastest growing mode of the tilted model equations at $r = 0.01$ which is a DRV. The domain size is $L = 8\pi$ and the grid spacing is $\Delta x = 0.025$. The terms in the PV budget that are shown are the total tendency (blue) and the contributions from zonal advection (red dashed), and latent heating (black dashed dotted). The PV tendency from radiative cooling is a small constant with a value of $\overline{r(w)w} = -0.011$ (not shown). All quantities are non-dimensional and the overall magnitude of the DRV is arbitrary. The PV budget has been zoomed in around the location of ascending motion since the DRV occupies only a small fraction of the domain.

no drag (not shown).

We next analyze the PV dynamics of the DRV mode. The PV budget in the lower layer was obtained by rewriting the $r(w)w$ term as $r(w)w = w - (1 - r(w))w$ in the thermodynamic equation (Eq. 2.6), eliminating the w term using the baroclinic vorticity equation (Eq. 2.5) and adding the barotropic vorticity equation (Eq. 2.4) to give

$$\frac{\partial q_2}{\partial t} = \sigma q_2 = q_{2x} + (1 - r(w))w + \overline{r(w)w}, \tag{2.8}$$

where $q_2 = \phi_{xx} - \tau_{xx} + \tau$ is the lower-layer PV, σ is the growth rate, q_{2x} is zonal advection, and $\dot{q}_{2,\text{diab}} = (1 - r(w))w + \overline{r(w)w}$ is the diabatic generation rate. A similar equation may be derived for the upper-layer PV anomaly $q_1 = \phi_{xx} + \tau_{xx} - \tau$ which has diabatic generation given by $\dot{q}_{1,\text{diab}} = -(1 - r(w))w - \overline{r(w)w}$. The DRV mode is made up of a positive PV anomaly in the lower layer and a negative PV anomaly in the upper layer that are both growing through diabatic PV generation (Fig. 2-3b). Note that meridional PV advection does not appear in the PV budget because the meridional PV gradients are zero by construction in the tilted model, but for completeness, we also show the meridional winds (Fig. 2-3c). Exploration of the parameter space of r shows that the basic PV structure remains similar for all values of $0 \leq r < 1$, although the growth rate and horizontal length scale of the ascent region do change when r is varied. At $r = 1$ the system is dry and stable because there are no contributions from latent heating, and by construction there are no meridional PV gradients to otherwise support baroclinic instability.

We calculate the growth rate of the mode by assuming exponential growth of the rms of $\mathbf{x} = [\Phi, T]$ over each time-step Δt to give $\sigma = \log\left(\frac{\text{rms}(\mathbf{x}(\mathbf{t}))}{\text{rms}(\mathbf{x}(\mathbf{t}-\boldsymbol{\Delta}\mathbf{t}))}\right)/\Delta t$. Note that the time-stepping is adaptive and the step size Δt can vary. We then average σ over the end period of the calculation ($t = 195 - 200$).

From Fig. 2-4 we see that within the narrow region of ascent the growth of the positive PV anomaly is due to diabatic PV generation through latent heating that is partially offset by zonal advection. In the region of descending motion to the west,

the PV generation due to latent heating is zero and the growth of the PV anomaly is due to zonal advection over a more extended spatial scale. The PV tendency from radiative cooling is spatially constant with a value of $\overline{r(w)w} = -0.011$. In the region of descent to the east, all the terms in the lower-layer PV budget are zero except for the time tendency and the small term due to radiative cooling. The PV budget in the upper layer is the same as in the lower layer except that the signs of the terms are flipped and they are mirrored about the axis of maximum ascent.

Now that we have isolated the DRV solution within a simplified model, it is possible to develop analytical solutions for its characteristics.

2.3.3 Analytic Theory

We now derive the growth rate and horizontal length scale of the DRV mode. In the modal regime, the DRV satisfies the equations

$$\sigma\phi_{xx} + \tau_{xxx} - \tau_x = 0, \tag{2.9}$$

$$\sigma\tau_{xx} + \phi_{xxx} - \phi_x + w = 0, \tag{2.10}$$

$$\sigma\tau - \phi_x + r(w)w = \overline{r(w)w}. \tag{2.11}$$

We eliminate the stream functions and combine the equations into a single equation for w

$$(rw)_{xxxx} - (2+\sigma^2)(rw)_{xx} + w_{xx} + (r+\sigma^2-1)w = \overline{rw}, \tag{2.12}$$

as shown in section 2.7.2 of the appendix. This equation is similar to the equation for w derived for moist baroclinic modes in an untilted two-layer model (compare with Eq.12 in Zurita-Gotor 2005) except for the two extra terms $-2(rw)_{xx}$ and $(r-1)w$ on the left-hand side of the equation, and the radiative cooling term $\overline{r(w)w}$ on the right-hand side which is constant in space but varies in time. As we will see shortly, the extra terms on the left-hand side are responsible for producing exponentially decaying rather than periodic solutions in the descent area which are characteristic

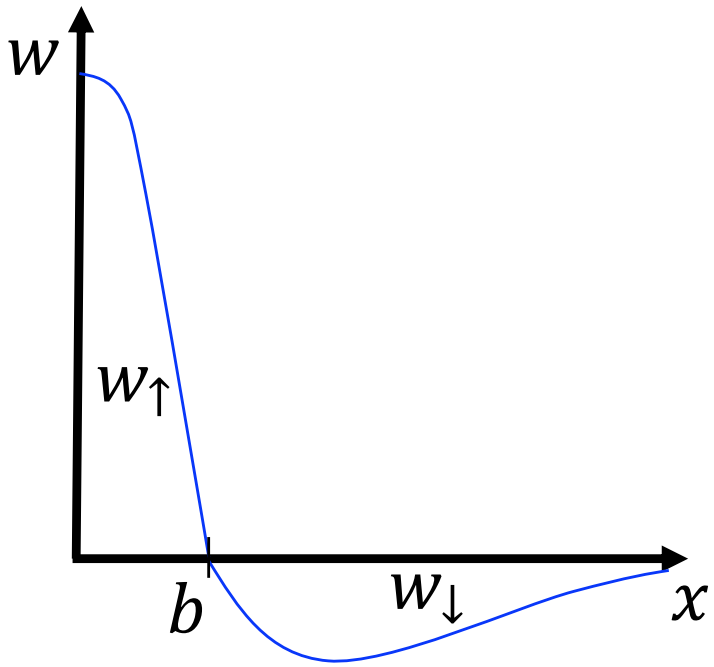

Figure 2-5: Schematic of the solution of the w equation (see Eq. 2.12) for the DRV mode. For $0 \leq x \leq b$ we have ascending motion $w = w_\uparrow > 0$ and $r < 1$, and for $x > b$ we have descending motion $w = w_\downarrow < 0$ and $r = 1$. $x = b$ is the location of the boundary between ascent and descent that must be found as part of the solution.

of an isolated DRV.

We look for symmetric solutions about the peak in w since that is what was obtained in the numerical solutions and since the equation for w is symmetric under $x \to -x$. We put the peak in w at $x = 0$, and by symmetry we need only consider the half of the domain $x \geq 0$, where w is ascending between $0 \leq x \leq b$ and descending for $x > b$ (see Fig. 2-5). Here b is the location of the boundary between ascent and descent that must be solved for.

Eq. 2.12 is readily solved separately in the descending and ascending region. In the descending region, the solution is given by

$$w_\downarrow = \frac{a}{\sigma^2} + d_1 e^{-(x-b)} + d_2 e^{-\sigma(x-b)}, \tag{2.13}$$

where $a = \overline{r(w)w}$, and we have discarded exponential solutions that become unbounded as $x \to \infty$ assuming growing solutions $\sigma \geq 0$. In the ascending region, the

solution is symmetric about $x = 0$ and is given by

$$w_\uparrow = \frac{a}{r + \sigma^2 - 1} + c_1 \cos(k_1 x) + c_2 \cos(k_2 x), \tag{2.14}$$

with wavenumbers

$$k_1 = \frac{1}{\sqrt{2r}} \sqrt{1 - r(2 + \sigma^2) + \sqrt{(1 - r(2 + \sigma^2))^2 - 4r(\sigma^2 + r - 1)}} \tag{2.15}$$

$$k_2 = \frac{1}{\sqrt{2r}} \sqrt{1 - r(2 + \sigma^2) - \sqrt{(1 - r(2 + \sigma^2))^2 - 4r(\sigma^2 + r - 1)}} \tag{2.16}$$

that are functions of r and σ.

We define the domain half-size to be L and then take the limit of an infinite domain $L \to \infty$. Mass conservation expressed as $\int_0^L w dx = 0$ allows us to rewrite $a = \frac{1}{L}\int_0^L r w dx = \frac{1}{L}\int_0^L (r-1) w dx = \frac{1}{L}\int_0^b (r-1) w_\uparrow dx$, which implies that $a \to 0$ as $L \to \infty$ if we want solutions for which b and $w_\uparrow$ remain bounded. We need additional constraints to determine the constants $c_1, c_2, d_1, d_2, \sigma$, and b. We impose that $w_\uparrow = w_\downarrow = 0$ at $x = b$, continuity of $(rw)_x$ and $(rw)_{xx}$ at $x = b$ and mass conservation. The continuity conditions follow from the continuity of ϕ, τ and the existence of the derivatives in the governing Eqs. 2.9-2.11. The constraint that $w_\downarrow = 0$ at $x = b$ gives

$$d_1 = -d_2 - \frac{a}{\sigma^2}. \tag{2.17}$$

Furthermore, the amplitude of the w solution is arbitrary which allows us to fix one of the amplitudes without loss of generality. We choose $d_2 = 1$ when $\sigma > 1$ and $d_2 = -1$ when $\sigma < 1$ to ensure that $w_\downarrow < 0$. In the limit of $L \to \infty$ and $a \to 0$, the resulting

equations are:

$$c_1 \cos(k_1 b) + c_2 \cos(k_2 b) = 0, \tag{2.18}$$

$$c_1 k_1 \sin(k_1 b) + c_2 k_2 \sin(k_2 b) = d_2 \frac{\sigma - 1}{r}, \tag{2.19}$$

$$c_1 k_1^2 \cos(k_1 b) + c_2 k_2^2 \cos(k_2 b) = d_2 \frac{1 - \sigma^2}{r}, \tag{2.20}$$

$$\frac{c_1}{k_1} \sin(k_1 b) + \frac{c_2}{k_2} \sin(k_2 b) = d_2 \frac{\sigma(\sigma - 1)}{\sigma^2 + r - 1}, \tag{2.21}$$

expressing $w_\uparrow = 0$ at $x = b$, continuity of $(r(w)w)_x$, continuity of $(r(w)w)_{xx}$, and mass conservation respectively. The limit of $L \to \infty$ and $a \to 0$ in the mass conservation equation must be taken carefully, a subtle point that is discussed in section 2.7.3 of the appendix.

Eliminating the constants c_1, c_2, which also gets rid of the arbitrary constant d_2 (see section 2.7.4 of the appendix), we obtain two equations

$$\tan(k_1 b) = \frac{r k_1 k_2}{\sigma + 1} \left(-\frac{1}{r k_2} + \frac{\sigma k_2}{\sigma^2 + r - 1} \right), \tag{2.22}$$

$$\tan(k_2 b) = \frac{r k_1 k_2}{\sigma + 1} \left(-\frac{1}{r k_1} + \frac{\sigma k_1}{\sigma^2 + r - 1} \right), \tag{2.23}$$

which along with the definitions of k_1 and k_2 (Eqs. 2.15,2.16) yield the dispersion relationship for the growth rate σ and half-ascent length b as a function of the static-stability reduction factor r, a key novel result of this paper.

In general, this dispersion relationship needs to be solved numerically, but in the limit of a convectively neutral stratification $r \to 0$ it is possible to show analytically that at leading order the growth rate is

$$\sigma = \frac{1 + \sqrt{5}}{2} = 1.62, \tag{2.24}$$

and the half-ascent length is

$$b = \frac{\pi}{2}\sqrt{r}, \tag{2.25}$$

(see section 2.7.5 of the appendix).[4] For comparison, the growth rate (σ) and half-ascent length (equal to b for the DRV) for the fastest growing modes in an untilted dry two-layer model (Phillips 1954) and moist two-layer model (Emanuel et al. 1987) are given in Table 2.1.

Note that the half-ascent length is just quarter the wavelength for the dry mode, and that the results in Emanuel et al. (1987) need to be rescaled by a factor $\sqrt{2}$ to agree with our nondimensionalization. The DRV grows about four times faster than the dry wave, and 1.5 times faster than the moist wave in the small r limit, consistent with the fact that the DRV emerges as the fastest growing solution in the warm climate simulations of moist baroclinic instability in O'Gorman et al. (2018).[5] The ascent length of the DRV and moist wave are the same in the small r limit, and about fifteen times smaller than that of a dry wave for $r = 0.01$.

To obtain σ and b for the full range of r, we solve the dispersion equations numerically. Equations (2.22) and (2.23) are solved using matlab's fsolve. We start by solving at $r = 10^{-3}$ with initial guess $\sigma = 1.53$ and $b = 0.06$ for the first two values of r, and we use linear extrapolation for the initial guesses at each subsequent value of r. The results are compared to the time-marching solutions of Eqs. 2.4,2.5 and 2.7 for a finite domain with periodic boundary conditions in Fig. (2-6), where we use a larger domain $L = 32\pi$ with $\Delta x = 0.084$ for all values of r to resolve the large and weakly growing solutions as $r \to 1$. Note that the time-marching solution at $r = 1$ is

[4]The dimensional growth rate for $r \to 0$ is 1.62 $\sqrt{2}Uf/(NH)$ and the dimensional half-ascent length is $\pi\sqrt{r}/(2\sqrt{2})NH/f$, where H is the depth of one layer and the vertical shear is $2U/H$.

[5]It is possible that 'climate warming' in the idealized GCM calculations of O'Gorman et al. 2018 favors DRVs both through a reduction in the r factor but also through changes in the mean state of the midlatitude atmosphere, in particular a weakening of the mean meridional PV gradient structure at upper levels. Weaker PV gradients can also favor DRV formation (see section 2.4) and are not considered at this point. However, a separate set of instability calculations were performed in O'Gorman et al. 2018 in which the mean state of the atmosphere was held fixed at that of the current climate and the effects of latent heating were parametrized simply through a reduction of the static stability in updrafts, similar to theory. Consistent with the analytical results, the most unstable mode broke up from quasi-periodic waves into isolated DRV modes in the limit as $r \to 0$.

Table 2.1: Comparison of the nondimensional and dimensional growth rate σ, and half-ascent length in two-layer models for the most unstable dry wave (Phillips 1954), moist wave (Emanuel et al. 1987) and DRV. The half-ascent length is given by quarter the wavelength for the dry wave, and by half the length of the region of ascent for the DRV and moist wave (for the DRV it is b). Dimensional values for the growth rate ($\sigma \frac{U}{L_D}$) and ascent length (bL_D) are calculated using typical scales $L_D = \frac{NH}{\sqrt{2}f} = 1000\,\mathrm{km}/\sqrt{2}$, and $U = 10\,\mathrm{m\,s^{-1}}$. The factor of $\sqrt{2}$ in L_D follows from our choice of nondimensionalization. Growth rates for the moist wave and DRV are presented in the limit of a convectively neutral stratification ($r \to 0$). Half-ascent lengths for the moist wave and DRV are presented as the small-r asymptotic expressions for the non-dimensional results, and evaluated at $r = 0.01$ (representative of a warm climate) for the dimensional results, since the ascent length would be zero for $r \to 0$.

	Growth rate $r \to 0$	Growth rate (day^{-1}) $r \to 0$
Dry wave	$\sqrt{2} - 1 = 0.41$	0.50
Moist wave	1.05	1.28
DRV	$\frac{1}{2}(1 + \sqrt{5}) = 1.62$	1.98

	Half-Ascent length $r \ll 1$	Half-Ascent length (km) $r = 0.01$
Dry wave	$\frac{\pi}{2\sqrt{\sqrt{2}-1}}$	1726
Moist wave	$\frac{\pi}{2}\sqrt{r}$	111
DRV	$\frac{\pi}{2}\sqrt{r}$	111

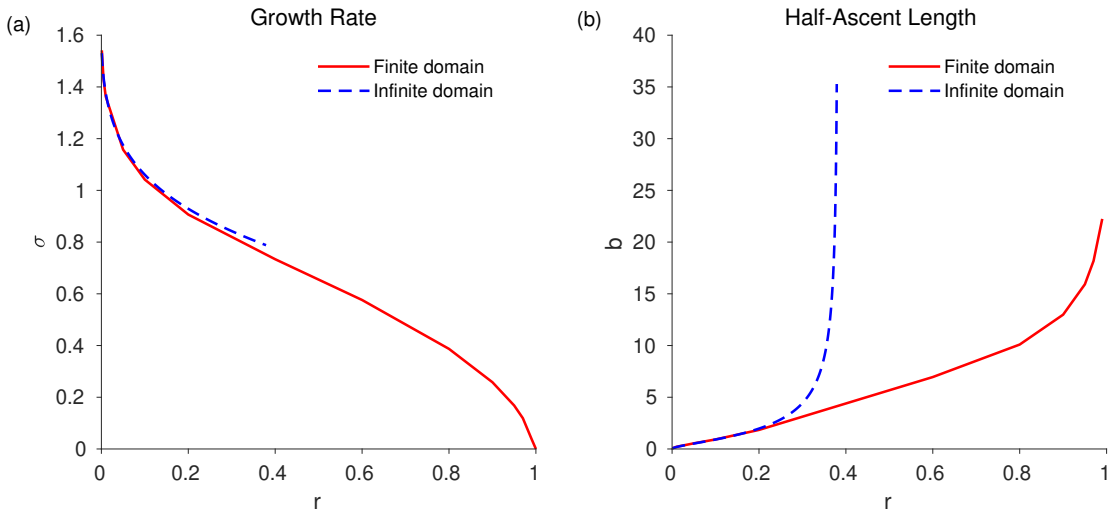

Figure 2-6: (a) Growth rate σ and (b) half-ascent length b from the time-marching solutions of the tilted model equations (Eqs. 2.4,2.5 and 2.7) in a finite periodic domain $L = 32\pi$ with $\Delta x = 0.084$ (solid red), and from the root-finding of the dispersion Eqs. (2.22-2.23) for an infinite domain (dashed blue).

not growing and is not shown in Fig. (2-6). The growth rates from the time-marching and dispersion-relation approaches are in good agreement for values below a critical value of $r = 0.38$, whereas the ascent lengths are in good agreement only for values of r less than roughly 0.2. A sample vertical-velocity profile at $r = 0.01$ (Fig. 2-7) confirms that the w profiles from the time-marching and dispersion relations are in very good agreement at small r. As the critical value of $r = 0.38$ is approached, the root-finding solution for b tends to large numbers. For values of $r > 0.38$, we only find solutions to the dispersion relation for which the half-ascent length $b < 0$. These solutions are unphysical and can be discarded.

Mathematically, the breakdown of the solution on an infinite domain at $r = 0.38$ can be traced to the point at which $\sigma^2 + r - 1 = 0$ and the right-hand sides of Eqs. (2.22-2.23) diverge to infinity. Empirically we find that as this point is approached, both k_1 and k_2 also go to zero, such that $b \to \infty$ is needed to balance a diverging right-hand side. Setting $k_1 = k_2 = 0$ we obtain $r = \left(3 - \sqrt{5}\right)/2 = 0.38$ and $\sigma = \sqrt{(\sqrt{5} - 1)/2} = 0.79$ for the breakdown point in good agreement with the numerical results. Beyond this point $\sigma^2 + r - 1 < 0$, which implies from Eqs. (2.15-2.16) that k_2 becomes imaginary while k_1 remains real. Hence, tan in Eq. (2.23) switches to tanh

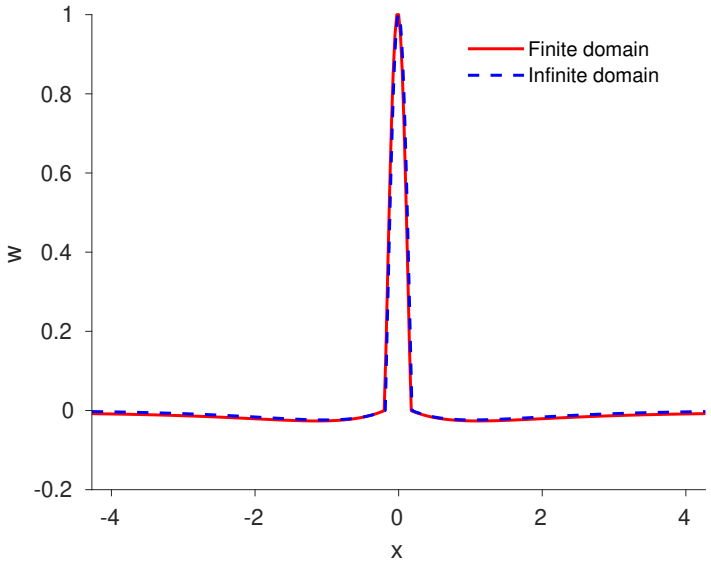

Figure 2-7: Comparison of the vertical velocity versus x for $r = 0.01$ from the time-marching solution (Eqs. 2.4,2.5 and 2.7) in a finite periodic domain (solid red), and from the root-finding of the dispersion relation (Eqs. 2.22-2.23) for an infinite domain (dashed blue).

while the right-hand side of Eq. (2.23) becomes negative. To satisfy the equation for growing modes, this requires $b < 0$ which is unphysical.

Thus, while DRV solutions continue to exist for $r > 0.38$ on a finite domain with periodic boundary conditions, isolated DRV solutions on an infinite domain cease to exist.

2.4 The role of meridional PV gradients and the wave-vortex transition

So far we have discussed the emergence of DRVs in a moist two-layer model with zero meridional PV gradients in which PV is generated purely from diabatic effects. While such a setup is a useful idealization for a DRV mode, we are interested in studying how the occurrence of DRVs generalizes to a more realistic situation with PV gradients. We start by considering a qualitative PV argument for how the dynamics changes as diabatic effects become dominant over meridional PV advection, and we then extend our tilted two-layer model to include meridional PV gradients.

2.4.1 PV dynamical perspective on the wave-vortex transition

The transition from a periodic wave to an isolated vortex mode in simulations of moist baroclinic instability in which diabatic effects become dominant can be interpreted elegantly within the PV framework of a moist two-layer model (see Fig. 2-8). Focusing on the lower layer (the upper layer is analogous), we start from the initial condition of a PV wave train consisting of positive and negative anomalies (Fig. 2-8a).

In a regime in which PV gradients are dominant, meridional advection of the negative background PV gradient in the lower layer would generate a positive PV tendency to the east of a positive PV anomaly, and a negative PV tendency to its west. These advective PV tendencies give rise to a eastward propagating Rossby wave that can phase lock and grow by interacting with a counter-propagating Rossby wave in the upper layer.

If instead we are in a regime in which the diabatic generation of PV is dominant, ascent to the east of a positive PV anomaly causes latent heat release that generates a positive PV tendency in the lower layer, whereas descent to its west does not generate latent heating and thus there is no negative PV tendency in the lower layer. Thus, only positive PV anomalies survive in the lower layer (with repeated amplitude rescaling to calculate the growing mode) due to the asymmetry in diabatic PV generation (Fig. 2-8b).

However, a series of positive PV anomalies have weaker meridional flow between them (because of cancellation of the induced flow from neighboring PV anomalies; Fig. 2-8b) as compared to the meridional flow surrounding an isolated single PV anomaly. Thus one PV anomaly is a faster growing mode of the system when diabatic PV generation is dominant over meridional PV advection (Fig. 2-8c).

2.4.2 Including PV gradients in the two-layer tilted model

A range of PV gradients can be easily included in our two-layer model by tilting the top and bottom boundaries at variable slopes $h_{1y} = \alpha_1$ and $h_{2y} = \alpha_2$. We retain the basic state $\tau_0 = -y$ (nondimensionalized) and $\phi_0 = 0$ corresponding to a shear

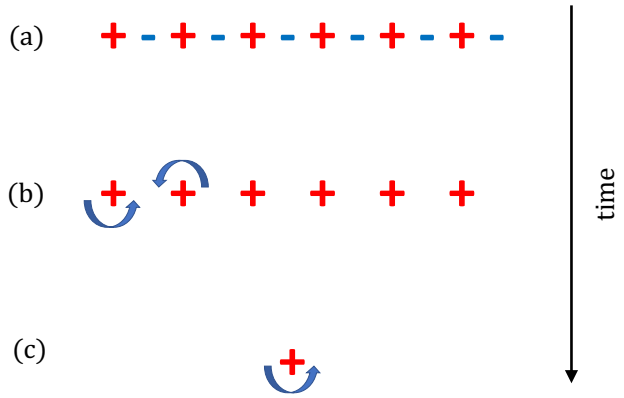

Figure 2-8: PV perspective on the transition from a periodic wave to an isolated vortex in simulations of moist baroclinic instability. Cyclonic PV anomalies are shown in red pluses and anticylonic PV anomalies are shown in blue minuses. Blue arrows illustrate the direction of horizontal winds induced by the anomalies. Starting from an initial condition consisting of (a) a wave train of PV anomalies in the lower layer, (b) only positive anomalies survive due to the asymmetry in diabatic generation. However, a series of positive anomalies have weaker meridional flow between them which leads to weaker diabatic PV generation as compared to an isolated anomaly, and thus (c) one anomaly is a faster growing mode of the system.

flow in thermal wind balance. The perturbation equations around this basic state are derived in section 2.7.1 of the appendix and take the form

$$\partial_t \phi_{xx} + \tau_{xxx} - \frac{1}{2}(\alpha_1 - \alpha_2)\phi_x - \frac{1}{2}(\alpha_1 + \alpha_2)\tau_x = 0, \tag{2.26}$$

$$\partial_t \tau_{xx} + \phi_{xxx} - \frac{1}{2}(\alpha_1 - \alpha_2)\tau_x - \frac{1}{2}(\alpha_1 + \alpha_2)\phi_x + w = 0, \tag{2.27}$$

$$\partial_t \tau - \phi_x + r(w)w = \overline{r(w)w}, \tag{2.28}$$

with PV gradients $q_{1y} = 1 - \alpha_1$ and $q_{2y} = -1 + \alpha_2$.

We solve the equations numerically for given values of r, α_1 and α_2 using time marching as in section 2.3.2. We use a domain size of $L = 8\pi$, but to calculate solutions for a large parameter space we use a larger grid spacing of $\Delta x = 0.13$ than before. We classify the most unstable solution as either an isolated DRV (single local maximum in w) or a periodic wave (multiple local maxima in w) or stable. Local maxima in w for which $w < 0$ are not counted. Cases that are stable or very weakly

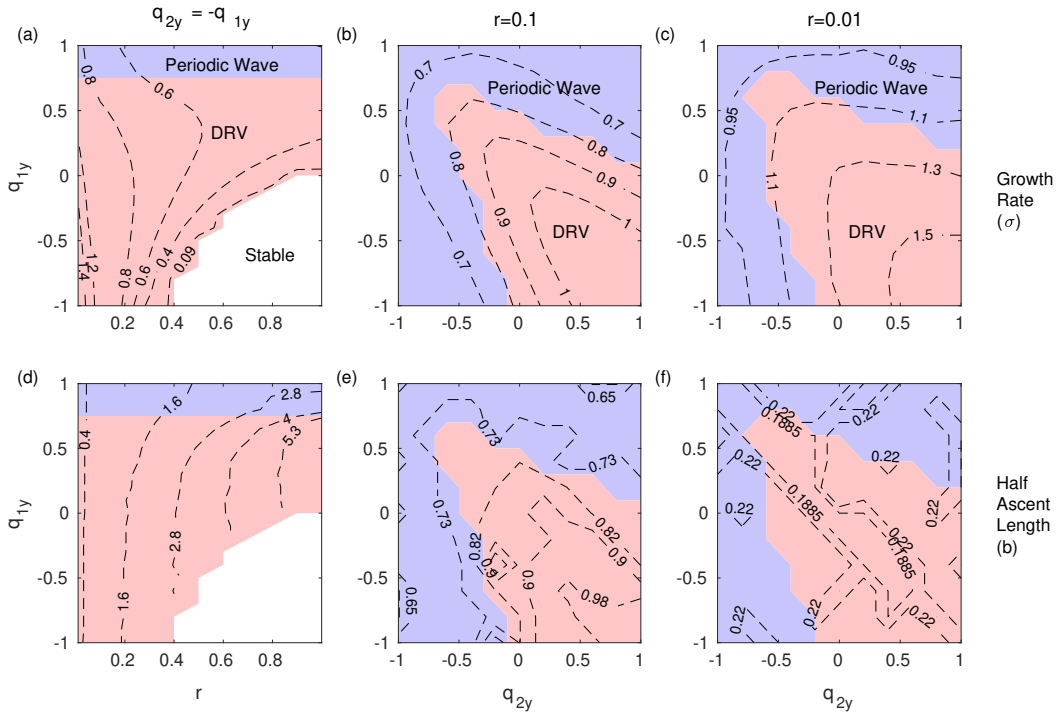

Figure 2-9: Phase diagram showing whether the most unstable mode of the tilted two-layer model is a periodic wave (blue) or a DRV (red) or stable (white) for a setup where (a,d) the PV gradients are equal and opposite in strength $q_{1y} = -q_{2y}$ for multiple values of r, and for a setup where the PV gradients vary independently from each other and (b,e) $r = 0.1$ or (c,f) $r = 0.01$. Dashed lines in (a-c) show the growth rate and dashed lines in (d-f) show the half-ascent length b. The domain length is $L = 8\pi$ and the grid spacing is $\Delta x = 0.13$. Note that the standard two-layer configuration has positive upper-layer PV gradient ($q_{1y} > 0$) and negative lower-layer PV gradient ($q_{2y} < 0$) which corresponds to the upper-left quadrants in (b,c,e, and f).

growing ($\sigma < 0.09$) are counted as stable. The results of this classification are shown in Fig. 2-9 along with the growth rate σ in Fig. 2-9 a-c and half-ascent length b in Fig. 2-9 d-f.

We begin by focusing on the equally-tilted case $\alpha_1 = \alpha_2 = \alpha$ for which $q_{1y} = -q_{2y} = 1 - \alpha$. We let $0 \leq \alpha \leq 2$ which includes the classic untilted regime with $q_{1y} = 1$ and $q_{2y} = -1$ at $\alpha = 0$, the no PV gradient regime $q_{1y} = q_{2y} = 0$ from the previous section at $\alpha = 1$, and a reversed PV gradient regime $q_{1y} = -1$ and $q_{2y} = 1$ at $\alpha = 2$. For $\alpha < 1$, a DRV emerges as the fastest growing solution when the magnitudes of the upper and lower PV gradients are weaker than a threshhold q_{ycrit}

of roughly 0.7 such that $q_{1y} = -q_{2y} < q_{ycrit}$ as shown in Fig. 2-9a.[6] When instead the magnitudes of the upper and lower PV gradients are greater than the critical threshold ($q_{1y} = -q_{2y} > q_{ycrit}$), the periodic wave emerges as the fastest growing solution for all values of r. For the cases with $\alpha > 1$ where the PV gradients are reversed from their usual directions, a DRV is the fastest growing solution but it is necessary for r to be sufficiently low for the solution to be unstable, consistent with the dry solutions ($r = 1$) being Fjørtoft stable (Fjørtoft 1950, Pedlosky 1964) due to the mismatch between the directions of the shear and PV gradients. Evidently, this mismatch is also sufficient to inhibit the growth of the moist modes unless r is sufficiently low such that the dynamics is dominated by latent heating. Overall, these results confirm that the emergence of isolated DRV modes in the tilted model is not an artifact of having exactly zero PV gradients — though this is a useful limit to consider for theory — but rather generalizes to more realistic configurations that do include PV gradients. Again, we have repeated the calculations using a linear drag acting on the relative vorticity in the lower layer with a damping time scale of either 10 days (weak drag) or 2.5 days (strong drag). The wave-vortex transition persists, with the precise boundary largely unaffected by drag. Length scales are similar, but the growth rates are reduced (not shown).

Surprisingly, Fig. 2-9a suggests that the transition from wave to DRV regime in the two-layer model with equal and opposite PV gradients is independent of r (the boundary at q_{ycrit} is entirely horizontal) but does rely on weakening or reversing the PV gradients compared to the classic untilted two-layer model. We investigate this result further by repeating the calculations with PV gradients that are not equal and opposite, but rather allowed to vary independently from each other, for two example values of r (Fig. 2-9 b, c). We observe that lowering of r, as expected in a warmer climate whose stratification is closer to moist adiabatic, does make a difference since it produces DRVs as the fastest growing solution for a larger range of PV gradients,

[6]Note that the solutions classified as DRVs at $r = 1$ could instead be considered to be waves. From the dry dispersion relation, the wavelength of these most unstable dry modes becomes infinite (not shown), and thus one maximum in w is found numerically in the domain no matter how large of a domain is chosen. Note also that the pure DRV solution with $q_{1y} = q_{2y} = 0$ at $r = 0.9$ is shown to be stable but would grow weakly on a larger domain.

particularly away from the diagonal line where the PV gradients are exactly equal and opposite. We also recall from the analytical solutions the existence of an upper bound on r for DRVs to occur in an infinite domain when the PV gradients are zero (Fig. 2-6). Overall, we find that both weak PV gradients and weak moist static stability (small r) can favor DRVs.

2.5 Comparison to storms at finite amplitude

Our two-layer theory for DRV modes and the warm-climate DRV mode in the idealized GCM calculation of O'Gorman et al. (2018) are both based on an assumption of small amplitude disturbances. In this section, we analyze DRV storms in reanalysis and a warm-climate simulation of the idealized GCM to see how finite amplitude affects storm structure. We are particularly interested in the question of whether finite-amplitude effects can weaken the upper-level anticyclonic PV anomaly and possibly lead to DRVs that propagate but do not grow strongly due to the lower PV anomaly not having a strong enough upper PV anomaly with which to interact. Differences in the vertical structure of PV anomalies are expected at finite amplitude for two reasons. First, diabatic PV generation is weaker at finite amplitude in anticyclonic regions, an effect that is captured in semigeostrophic models (Hoskins, 1975; Emanuel et al., 1987). Second, vertical advection of PV at finite amplitude can significantly offset negative diabatic generation at upper levels because positive PV anomalies at lower levels are advected upwards.

We compare the structure of the warm climate DRV mode (Fig. 2-1a) to a finite-amplitude DRV storm in the same idealized GCM and climate (Fig. 2-1c) and to two finite-amplitude storms from reanalysis. The first storm from reanalysis is the east-coast winter storm (Fig. 2-10a), that was identified as a propagating and moderately growing DRV by Moore et al. (2008). It later experienced explosive growth through interaction with a prexisting upper PV anomaly, but we consider the earlier diabatic phase. The second storm from reanalysis is an example midlatitude summer cyclone (Fig. 2-10 c) from an updated version of the DRV climatology of Boettcher and Wernli

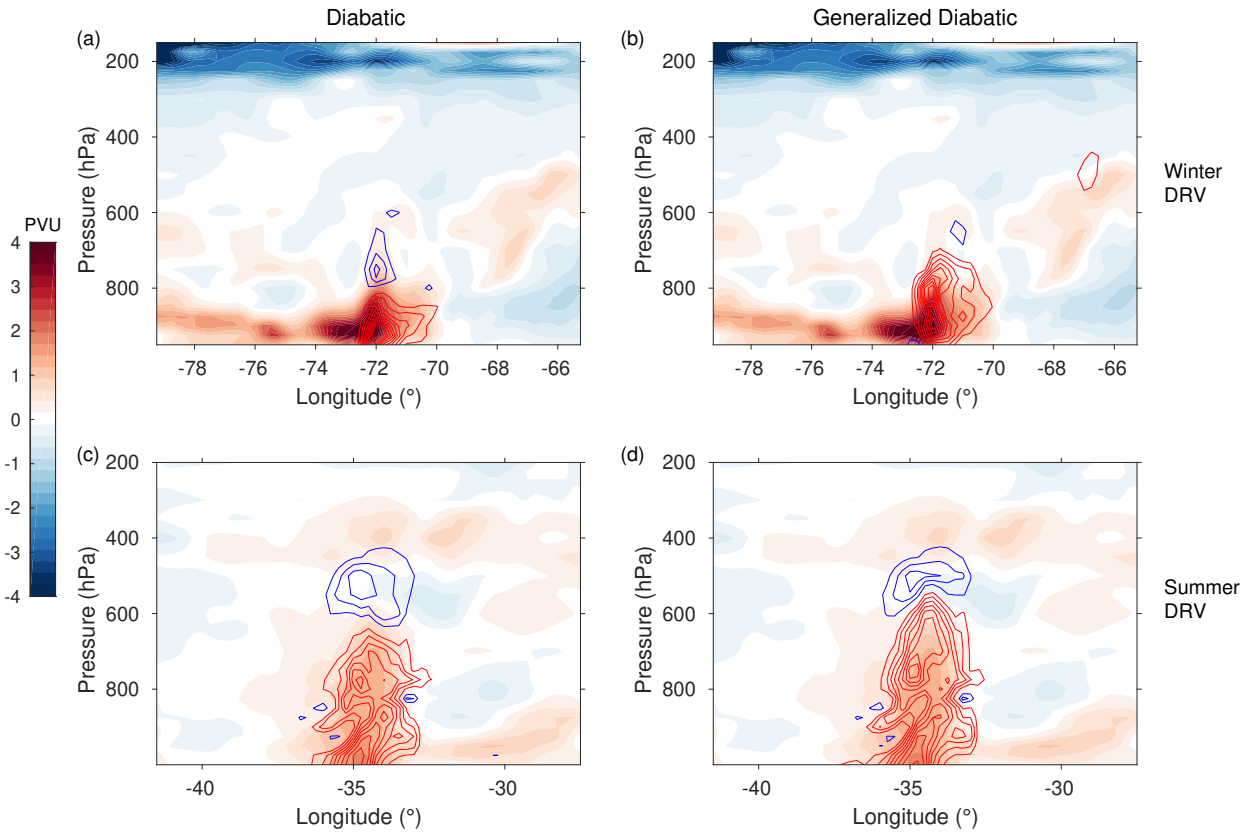

Figure 2-10: PV structure and PV generation rate due to latent heating of the (a,b) 2005 winter storm (latitude 37° at 0000UTC 25 Feb 2005) which was identified as a DRV in Moore et al. (2008), and (c,d) an example summer cyclone (latitude 41.25° at 0500UTC 10 Jul 2009) which was identified as a DRV in the climatology of Boettcher and Wernli (2013). Shading shows PV anomalies with respect to a 4-day moving average (using 6-hourly fields). Contours show (a,c) the diabatic PV generation (the first term on the right-hand-side of Eq. (2.30)) and (b,d) the generalized diabatic PV generation including both diabatic PV generation and diabatic vertical advection as in Eq.(2.29). In all cases only diabatic effects from latent heating are included. Red contours are positive and blue contours are negative, and the contour interval is 0.44 pvu h^{-1} for (a,b) and 0.10 pvu h^{-1} for (c,d). The zero contour line is not shown. All fields are calculated from ERA5 reanalysis, and PV is calculated using the hydrostatic approximation to Ertel's PV.

(2013) that is based on ERA5 reanalysis (Hersbach et al. 2020). It was identified as a DRV by a tracking algorithm, selecting for substantial baroclinicity, sufficient moisture, fast propagation, and weak upper-level forcing. These example storms are meant to illustrate some of the variations in the constellation of PV anomalies and diabatic generation in observed DRVs.

Ertel PV anomalies are defined with respect to a zonal mean for the idealized GCM (using once daily fields for the mode and 6 hourly for the macroturbulent state) and with respect to a 4-day moving average for the 6-hourly fields from ERA5 reanalysis forecasts. The forecast mode is chosen because it provides the temperature tendencies necessary for the calculation of latent heating. The fields are first interpolated from model to pressure levels, for both GCM and reanalysis fields, prior to calculating the PV and PV generation rates.

In addition to considering the usual diabatic PV generation rate, we also consider the diabatic source of PV in isentropic coordinates according to Eq.(74a) in Hoskins et al. (1985)

$$\dot{Q}_{\text{diab}} = Q^2 \frac{\partial(\dot{\theta} Q^{-1})}{\partial p} \left(\frac{\partial \theta}{\partial p} \right)^{-1} \tag{2.29}$$

which we refer to as the generalized PV generation. Here Q is the potential vorticity, θ is the potential temperature, $\dot{\theta}$ is the potential temperature tendency, and we have re-expressed the vertical derivatives with respect to pressure rather than potential temperature. Equation 2.29 may also be written as

$$\dot{Q}_{\text{diab}} = Q \frac{\partial \dot{\theta}}{\partial p} \left(\frac{\partial \theta}{\partial p} \right)^{-1} - \dot{\theta} \frac{\partial Q}{\partial p} \left(\frac{\partial \theta}{\partial p} \right)^{-1}, \tag{2.30}$$

which shows that the generalized PV generation combines diabatic PV generation (first term on the right hand side) and diabatic vertical advection of PV (second term on the right hand side).[7] Including vertical advection of PV is important because it

[7] An alternative approach of including vertical advection of PV in pressure coordinates (rather than diabatic vertical advection) gives similar results except that there can be additional vertical advection of PV in the upper troposphere and stratosphere in regions where latent heating is small.

can strongly offset diabatic PV generation (Büeler and Pfahl 2017, Lackmann 2002, Martínez-Alvarado et al. 2016, Stoelinga 1996, Persson 1995, Pfahl et al. 2015, Wernli and Davies 1997), and its inclusion clearly improves the match between the vertical structures of PV anomalies and PV generation for the small-amplitude DRV mode in the idealized GCM (compare Fig. 2-1a,b). In addition, considering diabatic vertical advection as part of the diabatic source of PV makes a closer connection to our QG theory in which the pseudo-PV is not advected in the vertical.

We only consider diabatic effects due to latent heating. For the idealized GCM, we have confirmed that there is no convective precipitation in the region of the finite-amplitude DRV storm, and $\dot{\theta}$ was inferred from the large-scale condensation tendency of specific humidity which was saved as an output field. For the reanalysis fields, $\dot{\theta}$ was calculated from the ERA5 temperature tendency from all parameterizations in the forecast mode minus the contributions from longwave and shortwave radiation. Radiative contributions to PV generation were separately evaluated and found to be negligible.

The finite-amplitude DRVs from reanalysis (Fig. 2-10) do not extend as high in the atmosphere as the DRV in the warm climate of the idealized GCM, and this is as expected given that they occur in the current climate in which tropopause is lower and latent heating occurs lower in the troposphere. The generalized diabatic PV generation (contours in Fig. 2-10b,d) is noticeably smaller in magnitude for the upper-level negative generation rates as compared to lower-level positive generation rates. From the point of view of Eq. (2.30), the magnitude of diabatic PV generation is reduced in the upper anticylonic region as compared to the lower cyclonic region in which Q is larger, an effect that has been seen before in the context of warm conveyor belts (Joos and Wernli 2012), and the negative diabatic PV generation is also offset by upward diabatic advection of positive PV from the positive PV anomaly lower in the atmosphere. Alternatively, from the point of view of Eq. (2.29), the factor of Q^2 tends to be much smaller in magnitude in anticyclonic regions as compared to cyclonic regions of a finite-amplitude storm. As a result, the upper-level negative PV anomaly is weaker in magnitude than the lower-level positive PV anomaly, especially

in the case of the winter storm in which it is difficult to clearly identify a negative upper-level PV anomaly that is diabatically generated.

The reason the winter storm has a greater asymmetry between lower and upper PV anomalies as compared to the summer storm seems to be because it is a stronger storm (which emphasizes the finite amplitude effects) but also because of more subtle effects related to its vertical profile of $\dot{\theta}$ being more bottom heavy. The absence of a clear upper-level negative PV anomaly in the winter storm may reduce its growth rate at this point in its evolution, but further work would be needed to definitively link the observed growth rates and PV structures, especially given that moist baroclinic waves in the semigeostrophic Eady model have weak upper-level negative PV anomalies but can still grow strongly (Emanuel et al., 1987).

The finite-amplitude DRV in the warm-climate simulation of the idealized GCM (Fig. 2-1c,d) shows some similarities to the corresponding small amplitude mode (Fig. 2-1a,b), although the upper-level negative PV anomaly and the generalized diabatic PV generation are considerably reduced in the storm compared to the mode for vertical levels between 300hPa and 500hPa and the positive PV anomaly extends higher, both as a result of diabatic vertical advection of PV. Negative generation of PV is nonetheless strong in the upper troposphere near the tropopause, and this seems to be because of diabatic vertical advection up the mean vertical PV gradient at those levels.

Overall, our analysis of finite-amplitude DRV storms shows that finite-amplitude effects must be taken into account to relate the structure of PV anomalies and diabatic generation in observed DRVs particularly for the upper-level PV anomalies. Our results also show the value of combining diabatic PV generation and diabatic vertical advection in a generalized diabatic PV generation diagnostic (following Hoskins et al. (1985)), especially when trying to connect to simpler QG models and modal solutions.

2.6 Conclusions

We have analyzed a moist two-layer QG model with conditional latent heating and tilted boundaries and shown that it is capable of producing a DRV mode. The emergence of a DRV solution in a minimal model retaining the essential physics of baroclinicity and moisture clarifies the physical mechanisms involved and allows us to derive the first analytical expressions for the growth rate and horizontal length scale of DRVs.

A key step in our approach is the tilting of the model boundaries at a slope equal to the mean isentropes which makes the two-layer model an analog of the interior of the Eady model in which dry-baroclinic instability has been shut off but moist instabilities are still possible. This allowed us to obtain a pure DRV solution within a conceptually simple two-layer model. PV-budget analysis revealed two distinct dynamical regimes. In the ascending branch, growth of the anomalies was maintained by diabatic heating partly offset by zonal advection, while in the descending branch growth was maintained solely by zonal advection.

We went on to derive the analytical dispersion relation for the growth rate and horizontal length scale of a DRV on an infinite domain, a significant novelty of this paper. The governing equation for the vertical velocity in the DRV is similar to the equation for the vertical velocity of moist baroclinic waves (Emanuel et al., 1987; Zurita-Gotor, 2005) except for the presence of two extra terms which lead to isolated rather than periodic solutions – a distinctive characteristic of the DRV. Analytic solutions to the dispersion equations were found in the limit of small static-stability reduction factor (i.e., in the limit in which the stratification is neutral to moist convection). While the ascent length remains the same for the DRV as for the moist wave solutions of Emanuel et al. (1987) in this limit, the DRV grows faster by 54% as compared to the moist wave. This faster growth is consistent with the fact that the DRV emerged as the fastest growing solution in the moist baroclinic instability simulations of O'Gorman et al. (2018) in a warm climate with small moist static stability. Root-solving of the dispersion equations for a larger range of r values showed that

physical solutions cease to exist when $r > 0.38$. This is an indication that isolated DRV disturbances cannot exist on an infinite domain when the moist static stability is not small enough.

Including non-zero meridional PV gradients in the tilted two-layer model and varying their strengths and varying the moist static stability (as represented by the reduction factor r), we showed that isolated DRV solutions emerge even in more realistic model setups and are not an artifact of the assumption of zero PV gradients in our simplest version of the tilted two-layer model. The most unstable mode transitions from periodic waves to isolated DRVs when the magnitude of the PV gradients is weakened or entirely reversed compared to the standard two-layer setup. This suggests that the vertical structure of meridional PV gradients may be an important additional factor that helps to determine DRV genesis zones in addition to small moist static stability. Weak QG PV gradients can be found particularly at polar latitudes in the current climate, which could help strengthen the links that have been previously established between the growth mechanism of DRVs and polar lows (Montgomery and Farrell 1991, Montgomery and Farrell 1992, Moore and Montgomery 2005, Moreno-Ibáñez et al. 2021).

The stark transition from periodic wave solutions to isolated DRV disturbances when diabatic heating becomes more important than meridional PV advection was also explained qualitatively using 'PV-thinking': in a diabatically dominated regime, the asymmetry of the diabatic heating regenerates only positive PV anomalies in the lower layer and negative PV anomalies in the upper layer. However, a series of like-signed PV anomalies in each layer leads to weaker meriodional flow between the PV anomalies than occurs for a single PV dipole consisting of one anomaly in each layer. Thus the single PV dipole has stronger ascent and latent heating and emerges as the fastest growing mode of the system.

Finally, we compared the structure of small-amplitude DRV modes with finite-amplitude storms from reanalysis in winter and summer and from a warm-climate simulation in an idealized GCM. The finite-amplitude storms have similarities with the small-amplitude DRV modes but also some differences. In the storms from re-

analysis, the upper-level negative PV anomaly is substantially weaker than the lower-level positive PV anomaly. This asymmetry arises because diabatic PV generation is weaker in anticyclonic regions at finite amplitude, and also because upward PV advection from the positive PV anomaly at lower levels can offset the upper-level negative PV generation. For the finite-amplitude DRV in the warm climate of the idealized GCM, vertical advection of the mean vertical PV gradient near the tropopause meant there was still a strong upper-level negative PV anomaly. In the case of the winter storm, the upper-level PV anomaly was sufficiently weak that it was difficult to identify, and we hypothesize that a weak upper-level PV anomaly may explain why some DRV storms in the current climate propagate but do not grow strongly. This hypothesis could be tested in future work with a semigeostrophic model that has sufficient vertical levels to accurately resolve vertical PV advection, and by tracking DRVs across a range of climates in idealized GCM simulations to study the relationship between growth rates and the structure of the PV anomalies.

Future work could also investigate whether a DRV solution and wave-vortex transition can also be isolated within a continous Eady model in which dry baroclinic instability is eliminated by removing the upper lid. This setup is likely no longer tractable analytically (because solutions are no longer separable in the presence of nonlinear heating (Zurita-Gotor 2005)), but a numerical analysis would make for a useful extension of this work, in which realistic features such as near surface temperature advection, vertically dependent drag and vertically dependent static stability reduction factor could be more readily incorporated.

2.7 Appendix

2.7.1 Derivation of the Tilted Two-Layer Model

We discretize the moist-quasigeostrophic equations on an f-plane (Eqs. 2.1,2.2) in the vertical taking into account the tilted boundaries $h_1(y)$ and $h_2(y)$ through a modified boundary condition on w at the top and bottom (Fig. 2-11). For the vorticity

equations in the two layers we obtain

$$\partial_t \nabla^2 \psi_1 + J(\psi_1, \nabla^2 \psi_1) - \frac{f}{H}(J(\psi_1, h_1) - w) = 0, \tag{2.31}$$

$$\partial_t \nabla^2 \psi_2 + J(\psi_2, \nabla^2 \psi_2) - \frac{f}{H}(w - J(\psi_2, h_2)) = 0. \tag{2.32}$$

Adding and subtracting gives vorticity equations in terms of the barotropic streamfunction ϕ and baroclinic streamfunction τ

$$\partial_t \nabla^2 \phi + J(\phi, \nabla^2 \phi) + J(\tau, \nabla^2 \tau) - \frac{f}{2H} J(\phi, h_1 - h_2) - \frac{f}{2H} J(\tau, h_1 + h_2) = 0, \tag{2.33}$$

$$\partial_t \nabla^2 \tau + J(\phi, \nabla^2 \tau) + J(\tau, \nabla^2 \phi) + \frac{f}{H} w - \frac{f}{2H} J(\phi, h_1 + h_2) - \frac{f}{2H} J(\tau, h_1 - h_2) = 0. \tag{2.34}$$

Discretizing the thermodynamic equation in the vertical, we obtain

$$\partial_t \tau + J(\phi, \tau) + \frac{N^2 H}{2f} r(w) w = \frac{N^2 H}{2f} \overline{r(w) w}. \tag{2.35}$$

We non-dimensionalize using $x, y \sim L_D$ where $L_D = \frac{NH}{\sqrt{2}f}$ is the deformation radius with individual layer height H, $z \sim H$, $u, v \sim U$, $w \sim \frac{U^2 H}{f L_D^2}$, $\phi = \tau \sim U L_D$, $t \sim \frac{L_D}{U}$, and $h_1, h_2 \sim \frac{UH}{f L_D}$ to obtain

$$\partial_t \nabla^2 \phi + J(\phi, \nabla^2 \phi) + J(\tau, \nabla^2 \tau) - \frac{1}{2} J(\phi, h_1 - h_2) - \frac{1}{2} J(\tau, h_1 + h_2) = 0, \tag{2.36}$$

$$\partial_t \nabla^2 \tau + J(\phi, \nabla^2 \tau) + J(\tau, \nabla^2 \phi) + w - \frac{1}{2} J(\phi, h_1 + h_2) - \frac{1}{2} J(\tau, h_1 - h_2) = 0, \tag{2.37}$$

$$\partial_t \tau + J(\phi, \tau) + r(w) w = \overline{r(w) w} \tag{2.38}$$

where all variables are now non-dimensional. We next assume small amplitude perturbations about the basic state $\tau_0 = -y$ and $\phi_0 = 0$ corresponding to a shear flow $u_1 = 1$ and $u_2 = -1$, such that the advection terms are linearized. Note however that the thermodynamic equation remains nonlinear because of the nonlinear dependence of $r(w)$ on w. Finally, using the tilted boundary conditions $h_1 = h_2 = y$ and

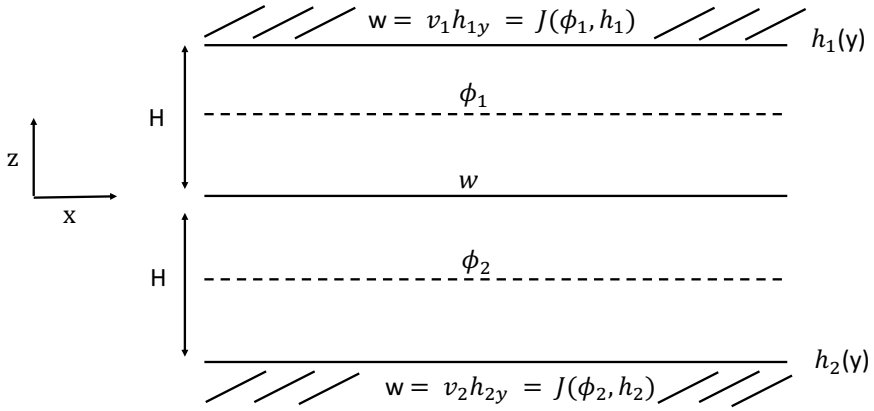

Figure 2-11: Schematic of the tilted two-layer model in the x-z plane.

assuming that the perturbations are independent of y gives the perturbation Eqs. (2.4-2.6). If instead we assume $h_1 = \alpha_1 y$ and $h_2 = \alpha_2 y$, we obtain the perturbation Eqs. (2.26-2.28).

2.7.2 Derivation of the equation for w

Starting from Eqs. (2.9-2.11), we first take two derivatives of Eq. (2.11) and subtract Eq. (2.10) to get

$$(r(w)w)_{xx} - w = 2\phi_{xxx} - \phi_x. \tag{2.39}$$

Multiplying Eq. (2.9) by σ and taking one derivative, and substituting for τ_{xx} and τ_{xxxx} using Eq. (2.10) we find

$$w - w_{xx} + \sigma^2\phi_{xxx} - \phi_{xxxxx} + 2\phi_{xxx} - \phi_x = 0, \tag{2.40}$$

where the last two terms $2\phi_{xxx} - \phi_x$ can be substituted using Eq. (2.39) to give

$$(r(w)w)_{xx} - w_{xx} = \phi_{xxxxx} - \sigma^2\phi_{xxx}. \tag{2.41}$$

Double integration of Eq. (2.41) yields the relation

$$r(w)w - w = \phi_{xxx} - \sigma^2\phi_x + \overline{r(w)w}, \tag{2.42}$$

where we have used mass conservation ($\overline{w} = 0$) to choose the integration constant (this relation will be necessary as a substitution at the end of the derivation). Taking two derivatives of Eq. (2.39) and subtracting Eq. (2.41) twice gives

$$(r(w)w)_{xxxx} - 2(r(w)w)_{xx} + w_{xx} = 2\sigma^2\phi_{xxx} - \phi_{xxx}. \tag{2.43}$$

Subtracting Eq. (2.39) multiplied by σ^2 from Eq. (2.43) we get

$$(r(w)w)_{xxxx} - (2+\sigma^2)(r(w)w)_{xx} + w_{xx} + \sigma^2 w = -\phi_{xxx} + \sigma^2\phi_x. \tag{2.44}$$

Using Eq. (2.42) allows us to substitute the last ϕ terms in Eq. (2.44) to finally obtain Eq. (2.12) which is an equation in w only.

2.7.3 Mass conservation for a DRV on an infinite domain

Imposing mass conservation $\int_0^L w dx = 0$ on the solution defined by Eqs. (2.13) and (2.14) and using Eq. (2.17) yields

$$\begin{aligned}\frac{ab}{r+\sigma^2-1} + \frac{c_1}{k_1}\sin(k_1 b) + \frac{c_2}{k_2}\sin(k_2 b) + \frac{a}{\sigma^2}(L-b) + \frac{a}{\sigma^2}(e^{-(L-b)} - 1) \\ + d_2\left(-\frac{1}{\sigma}(e^{-\sigma(L-b)} - 1) + (e^{-(L-b)} - 1)\right) = 0.\end{aligned} \tag{2.45}$$

We are interested in the infinite-domain limit $L \to \infty$. It is important that we took the integral in x to obtain Eq. (2.45) prior to taking the limit $L \to \infty$ (i.e., taking the limit of the statement of mass conservation) because the order of taking the limit and integral affects the result. As shown in section 2.32.3.3, the definition of a together with mass conservation implies that $a = \frac{1}{L}\int_0^b (r-1)w_\uparrow dx$ such that $a \to 0$ if we want

solutions for which b and $w_\uparrow$ remain bounded. This leaves us with the indeterminate term aL in the mass conservation equation (Eq. 2.45). We can eliminate this term by using

$$aL = \int_0^b (r-1) w_\uparrow dx = (r-1)\left(\frac{ab}{r+\sigma^2-1} + \frac{c_1}{k_1}\sin(k_1 b) + \frac{c_2}{k_2}\sin(k_2 b)\right), \quad (2.46)$$

to arrive at a form of the mass conservation condition that does not involve aL:

$$\frac{ab}{\sigma^2+r-1} + \frac{c_1}{k_1}\sin(k_1 b) + \frac{c_2}{k_2}\sin(k_2 b) + \frac{r-1}{\sigma^2}\left(\frac{ab}{\sigma^2+r-1} + \frac{c_1}{k_1}\sin(k_1 b) + \frac{c_2}{k_2}\sin(k_2 b)\right) - \frac{ab}{\sigma^2} + \frac{a}{\sigma^2}\left(e^{-(L-b)} - 1\right) + d_2\left(-\frac{1}{\sigma}(e^{-\sigma(L-b)} - 1) + (e^{-(L-b)} - 1)\right) = 0. \quad (2.47)$$

We can now take the limit $L \to \infty$ and $a \to 0$ to arrive at Eq. (2.21) in the main text. For completeness we note that by substituting Eq. (2.21) into Eq. (2.46), and taking the limit $L \to \infty$ and $a \to 0$, we obtain the expression

$$aL = d_2 \frac{(r-1)\sigma(\sigma-1)}{r+\sigma^2-1}. \quad (2.48)$$

2.7.4 Derivation of the dispersion relation

To derive the dispersion relation from the constraints (Eqs. 2.18-2.21), we write the constraints solely in terms of equations for c_1 and c_2. Writing Eq. (2.18) and (2.20) as

$$\begin{pmatrix} 1 & 1 \\ k_1^2 & k_2^2 \end{pmatrix} \begin{pmatrix} c_1\cos(k_1 b) \\ c_2\cos(k_2 b) \end{pmatrix} = d_2 \begin{pmatrix} 0 \\ \frac{1-\sigma^2}{r} \end{pmatrix}, \quad (2.49)$$

and inverting, we obtain

$$\begin{pmatrix} c_1\cos(k_1 b) \\ c_2\cos(k_2 b) \end{pmatrix} = \frac{d_2}{k_2^2 - k_1^2} \begin{pmatrix} k_2^2 & -1 \\ -k_1^2 & 1 \end{pmatrix} \begin{pmatrix} 0 \\ \frac{1-\sigma^2}{r} \end{pmatrix}. \tag{2.50}$$

Similarly, writing Eq. (2.19) and (2.21) as

$$\begin{pmatrix} k_1 & k_2 \\ 1/k_1 & 1/k_2 \end{pmatrix} \begin{pmatrix} c_1\sin(k_1 b) \\ c_2\sin(k_2 b) \end{pmatrix} = d_2 \begin{pmatrix} \frac{\sigma-1}{r} \\ \frac{\sigma(\sigma-1)}{\sigma^2+r-1} \end{pmatrix}, \tag{2.51}$$

and inverting, we obtain

$$\begin{pmatrix} c_1\sin(k_1 b) \\ c_2\sin(k_2 b) \end{pmatrix} = \frac{d_2 k_1 k_2}{k_1^2 - k_2^2} \begin{pmatrix} 1/k_2 & -k_2 \\ -1/k_1 & k_1 \end{pmatrix} \begin{pmatrix} \frac{\sigma-1}{r} \\ \frac{\sigma(\sigma-1)}{\sigma^2+r-1} \end{pmatrix} \tag{2.52}$$

Dividing the equations for $c_i \sin k_i b$ and $c_i \cos k_i b$, with $i = 1, 2$, by each other, we obtain the two tan equations that form the dispersion relation (Eqs. 2.22 and 2.23) in section 2.32.3.3.

2.7.5 Asymptotic expressions for growth rate and half-ascent length

In the limit $r \ll 1$, the wavenumbers can be simplified to $k_1 = \frac{1}{\sqrt{r}} + O(\sqrt{r})$ and $k_2 = \sqrt{\sigma^2 - 1} + O(r)$ where we assume that $\sigma = \sigma_0$ is an $O(1)$ quantity to be determined. Plugging these expressions into the two tangent Eqs. (2.22-2.23) that form the dispersion relation we obtain to leading order:

$$\tan\left(\frac{b}{\sqrt{r}}\right) = -\frac{1}{\sqrt{r}(1+\sigma_0)}, \tag{2.53}$$

$$\tan\left(b\sqrt{\sigma_0^2 - 1}\right) = \frac{\sqrt{\sigma_0^2 - 1}(1 - \sigma_0^2 + \sigma_0)}{(1+\sigma_0)(\sigma_0^2 - 1)}. \tag{2.54}$$

The right-hand side of Eq. (2.53) tends to minus infinity as r becomes small. To balance it, we use the ansatz $\frac{b}{\sqrt{r}} = \frac{\pi}{2} + \epsilon$ where $\epsilon \to 0$ as $r \to 0$, from which we obtain that

$$\tan\left(\frac{\pi}{2} + \epsilon\right) \approx -1/\epsilon = -\frac{1}{\sqrt{r}(1+\sigma_0)}, \tag{2.55}$$

which gives $\epsilon = \sqrt{r}(1+\sigma_0)$ and $b = \frac{\pi}{2}\sqrt{r} + r(1+\sigma_0)$ such that to leading order

$$b = \frac{\pi}{2}\sqrt{r}. \tag{2.56}$$

Linearizing the tangent in Eq. (2.54) we obtain:

$$b = \frac{1 - \sigma_0(\sigma_0 - 1)}{(1+\sigma_0)(\sigma_0^2 - 1)}. \tag{2.57}$$

Since b is $O(\sqrt{r})$ but the right-hand side of Eq. (2.57) is $O(1)$, the right hand side must vanish. Thus $1 - \sigma_0(\sigma_0 - 1) = 0$, which implies for growing solutions $\sigma_0 > 0$ that

$$\sigma_0 = \frac{1+\sqrt{5}}{2} = 1.62. \tag{2.58}$$

Chapter 3

Asymmetry of the Distribution of Vertical Velocities in the Extratropical Atmosphere in Theory, Models and Reanalysis

3.1 Abstract

The vertical velocity distribution in the atmosphere is asymmetric with stronger upward than downward motion. This asymmetry has important implications for the distribution of precipitation and its extremes and for an effective static stability that has been used to represent the effects of latent heating on extratropical eddies. Idealized GCM simulations show that current moist dynamical theories greatly overestimate the increase of the asymmetry of the vertical velocity distribution with climate warming. Here, we first analyze the changes in asymmetry with warming using numerical inversions of a moist quasigeostrophic omega equation applied to output from an idealized GCM. The inversions show that changes in the asymmetry are primarily related to changes in moist static stability on the left-hand side of the moist omega equation, whereas the dynamical forcing on the right-hand side of the omega equation

is unskewed and contributes little to the asymmetry of the vertical velocity distribution. We distill these insights into a toy model of the moist omega equation that is solved for a given moist static stability and wavenumber of the dynamical forcing. The toy model reproduces the slow increase of the asymmetry with climate warming in the idealized GCM simulations and over the seasonal cycle from winter to summer in reanalysis. The toy model also predicts that the asymmetry increases with increasing wavenumber. Consistent with this prediction, we show that simulations of moist quasigeostrophic turbulence produce highly asymmetric vertical velocity distributions in the strong latent heating regime despite unskewed dynamical forcing because the wavenumber is large compared to the inverse of the deformation radius. Thus we can understand the asymmetry of the vertical velocity distribution given the moist stability and wavenumber of the dynamical forcing in the omega equation, but further work is needed to understand this wavenumber.

3.2 Introduction

Many different meteorological variables - from geopotential height, to vorticity, to horizontal and vertical winds - show significant departures from Gaussianity in their climatology (Perron and Sura (2013)). Understanding how these skewed distributions arise from some of the underlying physical asymmetries of the atmosphere (planetary rotation, uneven insolation, irreversible fall-out of particles during precipitation) is one of the fundamental challenges of dynamical meteorology. Our focus here is on the large-scale vertical velocity field which has stronger upward than downward motion (Perron and Sura (2013),Tamarin-Brodsky and Hadas (2019)). We measure its asymmetry following O'Gorman (2011) by the factor

$$\lambda = \frac{\overline{\omega' \omega^{\uparrow'}}}{\overline{\omega'^2}} \tag{3.1}$$

where $\omega^{\uparrow} = \omega$ for upward motion and $\omega^{\uparrow} = 0$ otherwise, and primes denote deviations from horizontal averages. Assuming a vertical velocity distribution with zero mean, $\lambda = 0.5$ corresponds to upward and downward velocities that are of the same magnitude, and $\lambda \to 1$ corresponds to the limit in which upward motions are infinitely fast and occur over a vanishing ascent region.[1] The asymmetry parameter takes on typical values of $\lambda \approx 0.6$ in the midlatitudes, is larger in cyclones than anticyclones, and increases over the seasonal cycle between winter and summer storms (O'Gorman 2011,Tamarin-Brodsky and Hadas 2019). The asymmetry of the vertical velocity distribution has been of key interest in studies of precipitation and its extremes (Sardeshmukh et al. 2015, Pendergrass and Gerber 2016) because the intensity of precipitation is closely associated with the strength of upward motion. Furthermore, much research on moist midlatitude dynamics has relied upon an effective static stability to capture the modifying effects of latent heating on the circulation (O'Gorman 2011, Levine and Schneider 2015,Booth et al. 2015, Pfahl et al. 2015, Dwyer and O'Gorman 2017). While this effective static stability has proven a useful tool to convert dry into moist theories in a number of applications, it is not a closed theory since it directly depends on the asymmetry parameter λ which is not known from theory and must be inferred from reanalysis or simulation data. One of the key problems is thus to understand what sets the value of the asymmetry and how it responds as the climate warms.

The variation of the asymmetry parameter with warming was investigated in a previous study by O'Gorman et al. (2018) using an idealized aquaplanet GCM in which large changes in climate and in the extent of the nonlinearity of the flow can be simulated relatively easily. While the asymmetry factor λ increased strongly with warming for the most unstable modes of moist baroclinic instability, the asymmetry increased only slightly with warming in fully nonlinear simulations (O'Gorman et al. 2018, their Fig. 3b). This distinction is significant for our dynamical understanding since the atmosphere is in a macroturbulent state more akin to that of the fully nonlinear simulations, even if insights into cyclogenesis can be obtained from the

[1]If the mean ω is zero, then the asymmetry parameter λ and the skewness$=-\frac{\overline{\omega'^3}}{(\overline{\omega'^2})^{3/2}}$ increase together. However, λ is a lower order statistic that tends to be more robust in calculations and is more closely related to the updraft area fraction (cf. discussion in O'Gorman et al. 2018).

study of unstable modes. Here, macroturbulence refers to the turbulence of large-scale eddies in the troposphere following Held (1999). We will refer to the small-amplitude unstables modes as the 'modal regime' and the fully nonlinear simulations as the 'macroturbulent regime' from here on. The slight increase in λ with warming in the macroturbulent regime of the idealized GCM over a wide range in climates is also consistent with what has been found for the projected changes for the representative concentration pathway 8.5 emission scenario of MPI-ESM-LR (Tamarin-Brodsky and Hadas 2019).

In O'Gorman et al. (2018), the simulations of moist baroclinic instability differed from the fully nonlinear simulations by their small-amplitude disturbances but also by assuming that upward motion is saturated and by only taking into account moist diabatic tendencies from the large-scale condensation scheme and not from the moist convection scheme. To exclude the differences in the representation of moist processes as a cause for the different behavior of the asymmetry with warming, the authors performed a second set of simulations in which both large-scale condensation and moist convection scheme were turned off and the effects of latent heating were parameterized simply by reducing the dry static stability in the region of ascent by a factor $0 < r \leq 1$ in the spirit of simple moist dynamical theories (e.g. Emanuel et al. 1987, Zurita-Gotor 2005). Here, $r = 1$ corresponds to a fully dry simulation and $r \to 0$ corresponds to an increasingly warm and moist climate with weak moist static stability. The mean state of the simulations was held close to that of a control simulation by using a strong relaxation. From here on, we will refer to these simulations as 'reduced stability simulations' to distinguish them from the 'global warming simulations' that include convection and large scale condensation schemes. Even with this greatly simplified representation of moist physics, a similar distinction between modal and macroturbulent regimes emerged: while λ approaches one corresponding to highly asymmetric vertical velocities as $r \to 0$ in the modal regime, λ increases only slightly before equilibrating to a much lower value of about $\lambda = 0.71$ in the macroturbulent regime (O'Gorman et al. 2018, their Fig. 9). The different representation of moist physics are thus not a likely contributor to the different behavior of

λ. Instead, the authors concluded that nonlinear equilibration to a macroturbulent state leads to a significant reduction of skewness particularly in warm climates.

While simple theoretical scalings laws for the asymmetry of moist baroclinic waves exist (Emanuel et al. 1987, Zurita-Gotor 2005, Pendergrass and Gerber 2016), these do not carry over to the macroturbulent regime (O'Gorman et al. 2018, their Fig. 9) making it desirable to develop a theory for the asymptotic value of λ that is reached in the macroturbulent regime. To this end, we place ourselves in the framework of moist quasigeostrophic (QG) theory and more specifically a moist QG omega equation in which the effects of moisture are represented as an internal rather than external process. We show in section 3.3 that the moist QG omega equation captures the behavior of λ in the idealized GCM simulations of O'Gorman et al. (2018) when the dynamical forcing of vertical motion as represented by the right-hand side of the moist omega equation is taken as given from the output of the idealized GCM. The advantage of studying the vertical velocity field through the framework of the moist omega equation is that it allows us to tease apart the contributions to the vertical velocity and its asymmetry coming from the dynamical forcing versus those coming from the moist static stability. We go on to show that changes in λ in the modal regime are related to changes in both the moist static stability and the dynamical forcing, while changes in λ in the macroturbulent regime are primarily related to changes in moist static stability with the dynamical forcing not becoming very skewed.

In section 3.4, we use a two-layer moist quasigeostrohpic model to better understand the role of the moist static stability and dynamical forcing in setting λ. We show how a feedback between the dynamical forcing in the moist omega equation and the vertical velocity leads to an increase in asymmetry of the vertical velocity field in the modal regime. We then distill the insights from the macroturbulent inversions in section 3.3 into a simple toy-model of the moist omega equation in the macroturbulent phase that is solved for a given moist static stability and wavenumber of the dynamical forcing. In contrast to moist baroclinic theory, we show that the toy model reproduces the slow increase of the asymmetry with climate warming in the idealized GCM simulations. We also show that the toy model predicts that the asymmetry

increases as the wavenumber of the dynamical forcing increases. This implies the existence of strongly asymmetric states even for unskewed right-hand side forcing so long as the wavenumber of the dynamical forcing is sufficiently large.

In section 3.5, we apply moist baroclinic theory and our simple toy model to the change of asymmetry seen over the seasonal cycle in reanalysis. We show that while moist baroclinic theory overpredicts the increases in the asymmetry from winter to summer, the toy model does better at capturing the change of the asymmetry seen over the seasonal cycle.

In section 3.6, we run simulations of moist quasigeostrophic turbulence in a two-layer model and confirm the existence of highly asymmetric states when latent heating is strong in the simulations (by setting r to be small) despite unskewed dynamical forcing. As predicted by the toy-model, such states are possible because the wavenumber of the dynamical forcing is high compared with the inverse of the deformation radius. In this regime, the simulations have transitioned from a state of beta-plane turbulence with jets and vortices to a state dominated entirely by diabatic vortices. Thus while moist quasigeostrophic theory can explain much of the controls on the asymmetry of the vertical velocity field, higher-order effects beyond QG must also be taken into account to produce realistic wavenumbers of the dynamical forcing and thus asymmetry of the vertical velocity distribution.

In section 3.7, we summarize our results and discuss future work.

3.3 Moist QG Omega Equation Inversions applied to the Idealized GCM Simulations

The goal of this section is to understand the different sensitivity of λ to warming between modal and macroturbulent regimes by applying the moist QG omega equation in pressure coordinates,

$$\nabla^2(r(\omega)\sigma\omega) + f_0^2\omega_{pp} = \text{RHS}, \tag{3.2}$$

to the idealized GCM output. A derivation is given in the appendix 3.8.1. Here, ω is the vertical velocity in pressure coordinates, ∇ is the horizontal gradient, f_0 is the Coriolis parameter evaluated at the center of the domain used for the inversion, $\sigma = -\frac{RT}{p\theta}\theta_p$ is the static stability parameter with temperature T, potential temperature θ, pressure p, and gas constant for dry air R, and the right-hand side (RHS) of the moist omega equation is given by the dynamical forcing

$$\text{RHS} = -2\nabla \cdot \mathbf{Q} + f_0\beta\frac{\partial v_g}{\partial p}. \tag{3.3}$$

where β is the meridional derivative of the Coriolis parameter, ∇ is the horizontal gradient, and the Q-vector $\mathbf{Q}$ is given by

$$\mathbf{Q} \equiv (Q_1, Q_2) = \left(-\frac{R}{p}\frac{\partial \mathbf{u_g}}{\partial x} \cdot \nabla T, -\frac{R}{p}\frac{\partial \mathbf{u_g}}{\partial y} \cdot \nabla T\right) \tag{3.4}$$

following the form in Holton (2004), where $\mathbf{u_g} \equiv [u_g, v_g]$ is the geostrophic wind vector. In the definition of the RHS, we have ignored the contributions from radiation and friction. The static stability reduction factor $r(\omega)$ is given by

$$r(\omega) = \begin{cases} r, & \omega \leq 0 \\ 1, & \omega > 0 \end{cases} \tag{3.5}$$

where r takes the form

$$r = \frac{\theta}{\theta^*}\frac{\Gamma_m}{\Gamma_d}\frac{\frac{\partial \theta^*}{\partial p}}{\frac{\partial \theta}{\partial p}}, \tag{3.6}$$

under the assumption of saturated ascent (Fantini 1995). Here, θ^* is the saturated equivalent potential temperature, Γ_m is the moist adiabatic lapse rate and Γ_d is the dry adiabatic lapse rate. The nonlinear character of the $r(\omega)$ factor expresses the fundamental asymmetry that is introduced by considering the effects of moisture on the dynamics: while the ascending air is assumed saturated, releases latent heat upon condensation, and feels a reduced static stability, the descending air after irreversible fall-out of condensate during precipitation is subsaturated and feels the full static stability. This parametrization has been used in theoretical studies with semigeostrophic equations in Emanuel et al. (1987) and subsequently with quasigeostrophic equations by Fantini (1995) and Zurita-Gotor (2005) to study the modifying effects of moisture on canonical dynamical examples such as baroclinic waves and fronts. The reduction factor r calculated from Eq. (3.6) is a strong function of the vertical coordinate and approaches values of 1 in the upper troposphere (Whitaker and Davis 1994). We refer to the combined product of $r(\omega)\sigma$ as the moist static stability, and to the RHS as the dynamical forcing or right-hand side of the moist omega equation.

We leave the time-evolution of the flow to the higher order dynamics of the idealized GCM of O'Gorman et al. (2018) and use the GCM output of the moist static stability and the dynamical forcing at every time step to invert Eq. (3.2) for ω. For the reduced stability simulations, r was imposed. It is a function of the vertical only and follows the profile given on page 215 in O'Gorman et al. (2018), which makes r constant throughout most of the troposphere but allows it to smoothly transition to 1 in the stratosphere. For the global warming simulations, r is calculated from the temperature and pressure fields using Eq. (3.6) and varies horizontally, vertically and in time. As the climate warms, r gets smaller because the thermal stratification in the midlatitudes approaches a moist adiabat. At each vertical level, we set $r = 0$ if $r < 0$ and $r = 1$ if $r > 1$ to ensure the inversions are well posed.

Applying the inversion to both the most unstable modes and macroturbulent state of the idealized GCM simulations then allows us to assess the magnitude of the contributions from the moist static stability and dynamical forcing to the asymmetry parameter and to identify which contribution is weaker in the macroturbulent state

leading to a reduced asymmetry.

The GCM is based on a spectral version of the Geophysical Fluid Dynamics Laboratory (GFDL) atmospheric dynamical core (see Frierson et al. 2006, Frierson 2007 and O'Gorman and Schneider 2008). The default resolution is T85 ($\approx 1,4°$) with 30 vertical levels, which is the resolution used for both the global warming and reduced stability simulations. A thermodynamic mixed-layer ocean of depth 0.5m forms the lower boundary condition and no horizontal heat transport or sea ice is included. Moist convection is parametrized using the scheme of Frierson (2007). For the 'global warming simulations', long-wave radiation is modelled using a two-stream grey scheme with no seasonal or diurnal cycles of short-wave radiation and with no cloud or water vapour radiative effects. The climate is varied by changing the absorption coefficient α ($\alpha = 1.0$ corresponds to the control climate with $T_{surf} \approx 287$K) modifying the optical thickness of the atmosphere. The most unstable modes were calculated through repeated rescaling of perturbations to small amplitude, assuming upward motion to be saturated, and using a basic state equal to the zonal and time-mean of a fully nonlinear simulation for that climate (but with mean meridional and vertical winds set to zero). As mentioned, for the reduced stability simulations, radiation, large scale condensation and moist convection scheme were turned off and latent heating was parametrized by reducing the static stability in updrafts and not downdrafts. The mean state of the simulations was held close to that of the control simulation ($\alpha = 1.0$) by using a strong relaxation. The most unstable mode was calculated under the reduced stability parametrization following the small-amplitude approach for the global warming simulations. Further details can be found in O'Gorman et al. 2018.

3.3.1 Numerical Approach to Inverting the Moist Omega Equation

The moist quasigeostrophic omega equation (Eq. 3.2) has been solved before in the context of small amplitude baroclinic modes in a quasigeostrophic model (Fantini 1995). Here, we go further and solve the moist omega equation using output from a

GCM both in the regime of small-amplitude modes and fully macroturbulent flows. Solving Eq. (3.2) is a difficult task due to the nonlinearity of $r(\omega)$ which represents latent heating as an internal part of the dynamics rather than as an external forcing in the dry omega equation. We solve the equation iteratively as

$$\nabla^2(\sigma(p)\omega^{n+1}) + f_0^2\omega_{pp}^{n+1} = \text{RHS} + \nabla^2((1 - r(\omega^n))\sigma(p)\omega^n) \tag{3.7}$$

where ω^n is the solution at iteration n. We start with the dry solution obtained for $r(\omega) = 1$ everywhere as an initial guess. The domain spans latitudes 25°-65° with Dirichlet boundary conditions $\omega = 0$ on all boundaries, except at the lower boundary where we use $\omega = \omega_{GCM}$ with ω_{GCM} the vertical velocity taken from the idealized GCM. We continue iterating until $\text{rms}(\omega^{n+1} - \omega^n) \leq 10^{-4}$. At each iteration step, the equation is inverted using a 3-D variant (Zedan and Schneider 1983, Ferziger and Perić 2002) of the strongly implicit method (Stone 1968). The iterative scheme behind Eq. (3.7) has been written in such a way as to suggest a similarity to the repeated application of an omega-equation with explicit heating term $-\frac{\kappa}{p}\nabla^2 J = \nabla^2((1 - r(\omega^n))\sigma\omega^n)$ on the RHS where J is the latent heating, and κ is the ratio of the gas constant to specific heat capacity at constant pressure (see also Eq. 3.23). We have found that this form improves convergence of the inversions. While σ can in general be a function of the horizontal and vertical, we have found it useful for numerical stability to average T and θ horizontally before calculating σ (this is not done when calculating r in the global warming simulations). Hence, the background stratification that enters Eq. (3.2) for our inversions is only allowed to vary in the vertical. It is recalculated at each time-step and so can vary in time. Because the moist static stability is a product of $r(\omega)\sigma(p)$, and ω is a three dimensional field, the moist static stability will also remain a three-dimensional field. The equation is solved on a sphere.

Horizontal winds, vertical velocity, and temperature from the GCM output were interpolated from sigma to pressure coordinates and replaced with NaN wherever the interpolated pressure was below the surface pressure. Inversions were started at the

lowest pressure level where no NaN values were encountered in the domain. The geostrophic component of the wind was calculated as the rotational part of the full horizontal wind field, to minimize the influence of gravity waves (Nielsen-Gammon and Gold 2008), by inverting the relative vorticity on a global spherical grid in pressure coordinates.

Inversions with random initial guesses were also tried and the solutions were found to be insensitive to the choice of the initial guess. We have found it necessary to include $\omega = \omega_{GCM}$ as the lower boundary condition to better capture the macroturbulent values of λ in the global warming simulations, which were underestimated with the simpler boundary condition $\omega = 0$. We do so for the modal inversions and for the macroturbulent inversions in the reduced stability simulations for consistency, even though it did not substantially improve the agreement in these cases. Stricter convergence criteria rms$< 10^{-6}$ have also been experimented with but the solutions and values of λ were visually indistinguishable. Although the GCM domain is periodic in the zonal direction, the $\omega = 0$ boundary condition in the zonal direction has been adopted for implementational simplicity since the solver was developed from a pre-existing code with Dirichlet boundary conditions used in Li and O'Gorman (2020). Since we are interested in the statistics of λ and are considering averages over a large domain, the statistics are expected to be insensitive to what happens near the horizontal boundaries. The goodness of the agreement between the inverted and GCM vertical velocities and their asymmetries calculated over the domain (see section 3.3.2) give us confidence that the periodic boundary effects can be neglected for the purpose of this study.

3.3.2 Results of the Inversions

We begin by comparing the GCM and inverted vertical velocity field at 500hPa for the most unstable mode and macroturbulent regime of the global warming simulation at a global-mean surface air temperature of 288K (the reference simulation that is most similar to the current climate) at a single instant in time. A midtroposphere level is chosen because that is roughly where the vertical velocity is strongest. Two-

dimensional fields are shown in Fig. (3-1) and cross sections at 50° N latitude in Fig. (3-2). Focusing on the modes, we observe that inverted and GCM vertical velocity field are in near perfect agreement, except close to the boundaries where a different boundary condition was implemented (see Fig. 3-2a). Focusing on the macroturbulent fields, we observe that the agreement between inverted and GCM vertical velocity field is less good, and this is as expected since the flow is in a larger Rossby number state and was calculated without assuming upward motion to be saturated. Nevertheless, the inverted vertical velocity is able to capture most of the large scale ascent and descent patterns well, as confirmed by the cross section shown in Fig. (3-2b). Similar results were found in the reduced stability simulations (not shown).

We now compare the statistics of the asymmetry parameter λ for inverted and GCM vertical velocities in both the reduced stability and global warming simulations (Fig. 3-3). The basic behavior of the idealized simulations that we are trying to capture and understand is that in response to increasing global-surface temperature or decreasing reduction factor λ increases strongly for the most unstable modes but increases only slightly in the macroturbulent regime (Figure 3-3 a and c).

We show results for full inversions that include latent heating through $r(w)$ and thus the asymmetry can result from both latent heating and the RHS (Fig. 3-3 a,c). This is shown to confirm that the moist QG omega equation is able to capture the behavior of λ in the idealized GCM. We also show inversions in which we artificially set $r(w) = 1$ and hence the asymmetry in the inverted vertical velocity must only come from the RHS (Fig. 3-3 b, d). This is shown to reveal differences in the dynamical contributions to λ in the modal and macroturbulent regime. λ was calculated between $40° - 60°$ latitude for the global warming simulations and between $25° - 65°$ in the reduced stability simulations and then averaged in time, meridionally over the latitude band and vertically over the troposphere. Following O'Gorman et al. (2018), a wider latitude band is chosen for the reduced stability simulations because the unstable modes are not necessarily localized in the $40° - 60°$ latitude band. The tropopause was defined as the highest level at which the domain-mean lapse rate is greater than

2Kkm^{-1}.

We focus first on the results of the full inversion that includes latent heating through $r(w)$ (Fig. 3-3 a, c). We see that λ of the inverted vertical velocity field (which we will refer to as QG λ) is in close to perfect agreement with λ of the GCM vertical velocity field for the modes in both types of simulations. For the macroturbulent regime, QG and GCM λ are in reasonably good agreement, with QG λ becoming slightly larger than the GCM λ at low values of r and high global-mean surface air temperatures. In the dry limit of $r = 1$, $\lambda = 0.5$ for the modes indicating a symmetric vertical velocity distribution, whereas λ is slightly greater than 0.5 for the macroturbulent regimes, indicating that even a dry flow has up-down asymmetry at finite amplitude (cf. discussion in O'Gorman et al. (2018)). Despite the limitations in applying the QG omega equation to finite amplitude flows with a simplified representation of moist physics, we conclude that the QG omega equation is able to capture the different behavior of λ between unstable modes and macroturbulence in the idealized GCM.

Focusing next on the inversions in which $r(w) = 1$ (Fig. 3-3 b, d), we see that while the vertical velocity field remains asymmetric in the modal regime, the vertical velocity field is close to symmetric in the macroturbulent regime in both types of simulations. The difference in λ between modal and macroturbulent regimes becomes more pronounced in the limit of high temperature or low values of r. For example, for small values of r in the reduced stability simulations, we find $\lambda \sim 0.8$ for the modes versus $\lambda \sim 0.53$ in the macroturbulent regime. For reference, the value of the vertically averaged skewness of -RHS is equal to skewness= 0.1 in the macroturbulent phase, and skewness=5.9 in the modal phase at $r = 0.01$. We conclude that while both $r(\omega)$ and RHS contribute to the asymmetry of the vertical velocity distribution in the modal phase leading to large asymmetries, $r(\omega)$ is the primary contributor to the asymmetry of the vertical velocity distribution in the macroturbulent phase leading to substantially reduced asymmetries.

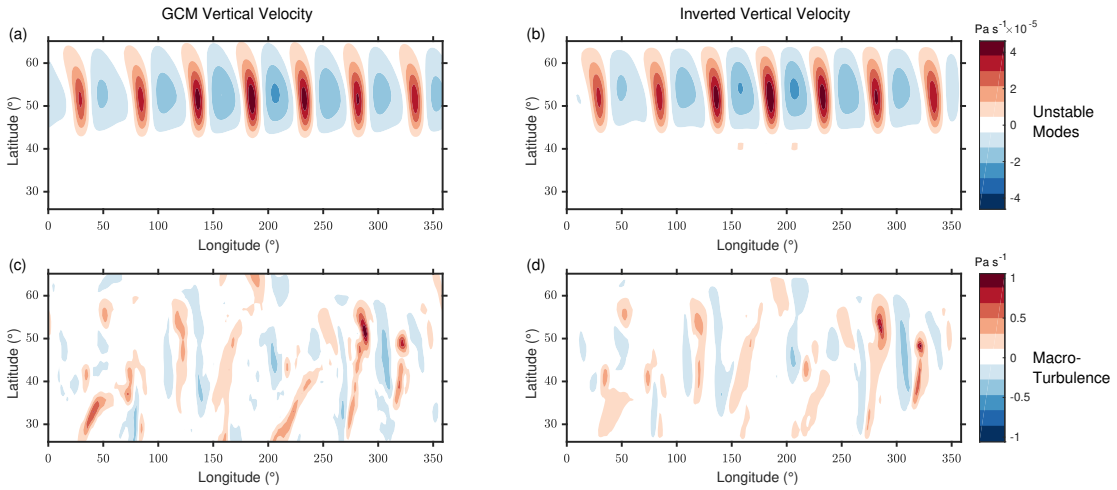

Figure 3-1: Comparison of the instantaneous GCM vertical velocity field to the inverted vertical velocity field ($-\omega$, red indicates upward motion), obtained from inversion of Eq. (3.2), at 500hPa. Results are shown for unstable modes (a,b) and the macroturbulent regime (c,d) of the global warming simulations of O'Gorman et al. (2018) at a global-mean surface air temperature of 288K. The modes were calculated by O'Gorman et al. (2018) through repeated rescaling of the equations to small amplitude and hence their magnitude is arbitrary. The time instant chosen for comparison was arbitrary.

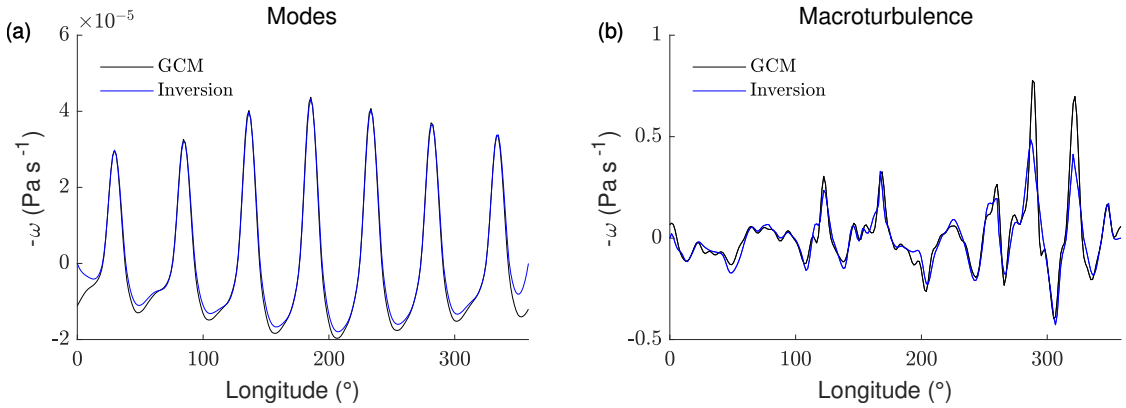

Figure 3-2: Cross section of the GCM (black) and inverted (blue) vertical velocity fields shown in Fig. (3-1) at latitude 50° for the modes (a) and the macroturbulent regime (b). The amplitude of the mode is arbitrary.

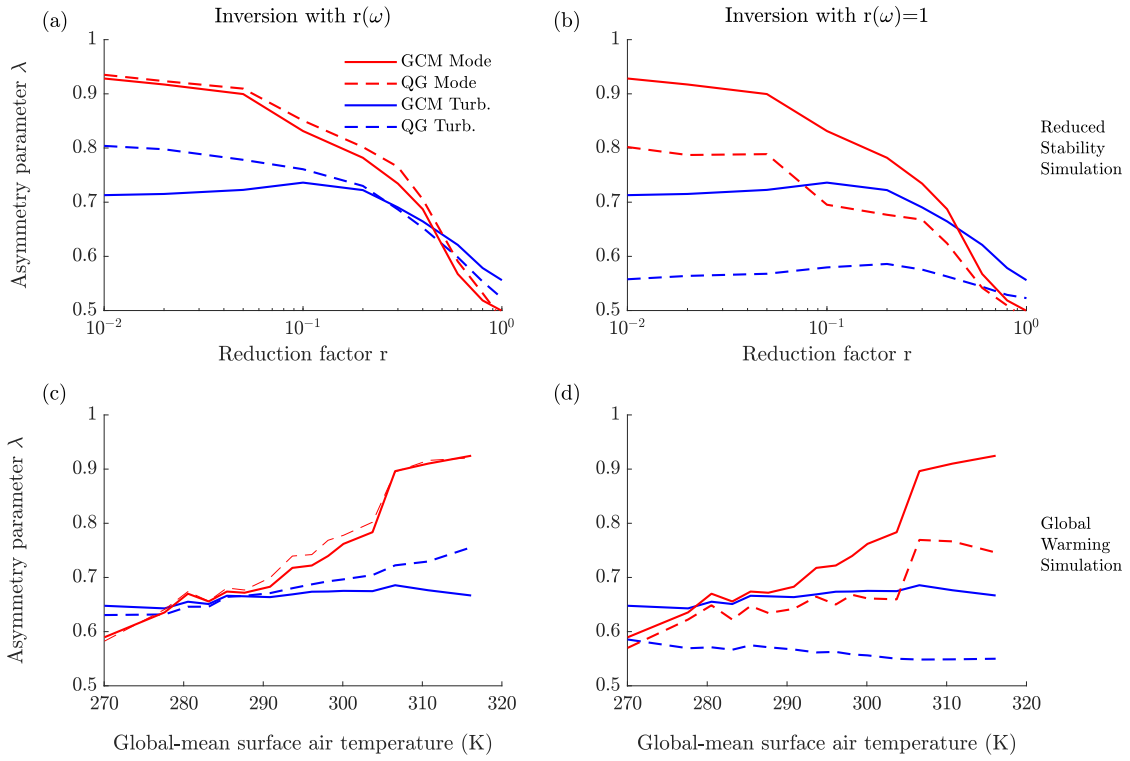

Figure 3-3: Comparison of the asymmetry parameter λ for GCM vertical velocities (solid lines) and the inverted vertical velocities (dashed lines), calculated from the inversion of Eq. (3.2). Results are shown for the modal (red) and macroturbulent (blue) regimes in the reduced stability simulations (a,b) and global warming simulations (c,d) from O'Gorman et al. (2018). In (a,c) $r(\omega)$ was used in the inversion of Eq. (3.2), whereas in (c,d) $r(\omega) = 1$ was used in the inversions. Hence, in (a,c) the asymmetry of the vertical velocity distribution comes from both $r(\omega)$ and the RHS, whereas in (c,d) the asymmetry only comes from the RHS. λ was calculated between $40° - 60°$ latitude for the global warming simulations and between $25° - 65°$ in the reduced stability simulations and then averaged in time and vertically over the troposphere.

3.4 Understanding Asymmetry Behavior using 2-layer moist QG

We next use a 2-layer moist QG framework to better understand the asymmetry behavior in the modal and macroturbulent regimes. We begin by developing an understanding for why the RHS is skewed in the modal regime in section 3.4.1, before distilling the insights of the 3-D inversions into a toy-model for λ in the macroturbulent regime in section 3.4.2.

The two-layer moist QG equations on an f-plane with equal layer height take the nondimensional form

$$\partial_t \nabla^2 \phi + J(\phi, \nabla^2 \phi) + J(\tau, \nabla^2 \tau) = 0, \tag{3.8}$$

$$\partial_t \nabla^2 \tau + J(\phi, \nabla^2 \tau) + J(\tau, \nabla^2 \phi) + w = 0, \tag{3.9}$$

$$\partial_t \tau + J(\phi, \tau) + r(w)w = 0, \tag{3.10}$$

with barotropic and baroclinic stream function $\phi = \frac{\psi_1+\psi_2}{2}$ and $\tau = \frac{\psi_1-\psi_2}{2}$ where ψ_1 refers to the streamfunction in the upper layer and ϕ_2 to the streamfunction in the lower layer, and with Jacobian $J(A, B) = A_x B_y - A_y B_x$. These equations are obtained from Eqs. (2.36-2.38)after setting the boundaries at top and bottom to be horizontal $h_1 = h_2 = 0$ and neglecting the radiative cooling term. The equations have been nondimensionalized assuming an advective time scale and with the deformation radius $L_D = NH/(\sqrt{2}f)$ as the length scale where H is the layer height.[2] The β effect is neglected here for simplicity.

3.4.1 Behavior of RHS for Moist Unstable Modes

To study the asymmetry of the vertical velocity in the limit of small amplitude perturbations growing on a basic state, we linearize the advective terms of the two layer

[2]Discretizing the continous thermodynamic equation leads to a deformation radius involving N, rather than a reduced gravity, at the mid-tropospheric level.

moist QG equations around a zonally uniform basic shear state in thermal wind balance $\tau_0 = -y$, $\phi_0 = 0$, $w_0 = 0$. We also assume the perturbations to be independent of the y direction. This yields the equations

$$\partial_t \phi_{xx} + \tau_{xxx} = 0, \tag{3.11}$$

$$\partial_t \tau_{xx} + \phi_{xxx} + w = 0, \tag{3.12}$$

$$\partial_t \tau - \phi_x + r(w)w = 0, \tag{3.13}$$

where τ, ϕ and w now refer to small-amplitude perturbations about the basic state.

Eqs. (3.11, 3.13, 3.14) have been studied in quasigeostrophic (Zurita-Gotor 2005) and semigeostrophic (Emanuel et al. 1987) form to analyze the effects of latent heating on the growth rate and length scale of the most unstable modes of baroclinic instability. It was found that latent heating increases the growth rate and shifts the most unstable mode to smaller length scales. Here, we focus on the effect of latent heating on the asymmetry of the vertical velocity of the most unstable moist modes.

To calculate the fastest growing modes for a given static-stability reduction factor $0 \leq r \leq 1$, we solve Eqs. (3.11-3.13) numerically. To this end, we discretize the equations using second-order central finite differences in a periodic domain in x of size $L = 8\pi$ with grid spacing $\Delta x = 0.13$. The equations are solved using the same procedure as outlined in section (2.3.2) but noting that here we do not tilt the upper and lower boundaries. We refer the reader to the paper for more detail and only summarize the basics here. The barotropic and baroclinic vorticity equations (Eqs. 3.11,3.12) are integrated forward in time and the system of equations is closed by calculating the vertical velocity w at each time step from the nonlinear omega equation,

$$(r(w)w)_{xx} - w = 2\phi_{xxx}, \tag{3.14}$$

which is formed by eliminating the time derivatives between Eq. (3.12) and (3.13).

The dynamical fields are rescaled to avoid large numbers, which could cause problems with the numerical representations, and the equations are run forward in time until the solution has converged to a normal mode.

An example vertical velocity profile of the most unstable moist mode in this system at $r = 0.1$ is shown in Fig. (3-4b). The solution consists of a periodic wave whose ascent length is reduced compared to the descent length. This is consistent with the structure of the most unstable mode that was found in the idealized GCM calculations (see Fig. 3-2a).

We repeat the calculation for different values of r and compare the asymmetry of the most unstable mode in this 1-D system to the asymmetry for the modes of the 3-D reduced stability GCM simulations in O'Gorman et al. (2018) (see Fig. 3-4a). The reduced stability simulations are chosen for ease of comparison to our two-layer model, since a constant reduction factor is applied throughout the troposphere in these simulations. In the global warming simulations, r varies with altitude which is more difficult to capture in a two-layer setting.

Looking at Fig. (3-4a), we see that the asymmetry of the most unstable modes of the 1-D theory agrees remarkably well with that found in the idealized GCM experiments given the simplicity of the two-layer setup. The modes become very skewed as $r \to 0$ which can also be confirmed by looking at the w profile of the most unstable mode from the 1-D theory at $r = 0.1$ (Figure 3-4b). The ascent length is greatly reduced compared to the descent length, in line with the results of Emanuel et al. (1987) and Zurita-Gotor (2005). The skewness of -RHS in 1-D theory is equal to skewness= 2.1.

We can now use the two-layer moist QG framework to explain why the RHS of the moist omega equation imparts so much asymmetry during the modal regime, as discussed in section 3.3. Combining Eqs. (3.11-3.12), it is possible to write an explicit equation for the RHS= $2\phi_{xxx}$ of the moist omega equation in the modal regime

$$\partial_{tt} 2\phi_{xxx} = (2\phi_{xxx})_{xx} + 2w_{xx}, \tag{3.15}$$

which forms a complete set of equations together with the moist omega equation (Eq. 3.14). We consider an initial value problem which is solved in time until the solution converges to a mode starting from initial conditions in which the RHS is unskewed initially. We observe from Eq. (3.15) that the RHS satisfies a wave-equation in the modal regime with $2w_{xx}$ as its source term. When the atmosphere is dry and thus $r = 1$, $2w_{xx}$ is of the same magnitude in ascending and descending regions. If the RHS is unskewed initially, it will thus remain so in time by Eqs. (3.14, 3.15). However, when the atmosphere is moist and thus $r < 1$, the moist omega equation implies that w_{xx} becomes different in magnitude between ascending and descending regions even if the RHS is unskewed. An example of a w profile in this situation is given by solutions to the moist omega equation with an unskewed RHS that will be considered in the next section (see Fig. 3-5b). For brevity, from now on we will refer to the extent to which w_{xx} is greater in magnitude in the ascent region compared to the descent region as the asymmetry of w_{xx}, and similarly for the asymmetry of RHS. By Eq. (3.15) the asymmetry of w_{xx} is imparted to the RHS such that RHS also becomes more asymmetric. The smaller r, the more asymmetric w_{xx} and hence the RHS, which explains the increased asymmetry imparted to the vertical velocity by the RHS in warm climates or for low values of r in section 3.3. Since the RHS forces the omega equation, its asymmetry will be imparted to the asymmetry of w and hence also that of w_{xx}. A feedback is established. For an initial value problem starting with a symmetric RHS, the asymmetry of the RHS is thus expected to grow before equilibrating to a constant value eventually when the modal structure is reached and all terms in Eq. (3.15) grow exponentially at the same rate.

3.4.2 Toy model for Moist Macroturbulence

In the macroturbulent phase, the full nonlinearities in Eqs. (3.8-3.10) are retained and the moist QG omega equation is instead given by

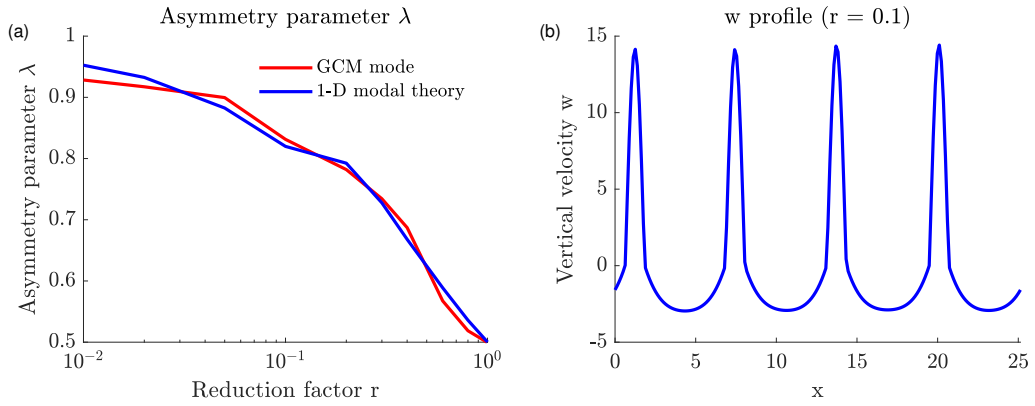

Figure 3-4: (a) Comparison of the asymmetry parameter λ for the most unstable modes predicted by 1-D moist baroclinic theory in a two-layer QG model, and for the most unstable modes calculated using a reduced stability parameterization for the GCM simulations of O'Gorman et al. (2018). The λ of the modes in the reduced stability GCM simulations is averaged over the tropophere and was also shown in Fig. (3-3a). (b) Vertical velocity profile of the most unstable mode of 1-D moist baroclinic theory at $r = 0.1$. The two-layer moist baroclinic modes were calculated by time-marching Eqs. (3.11, 3.12, 3.14) on a periodic domain of size $L = 8\pi$ with grid spacing $\Delta x = 0.13$.

$$\nabla^2(r(w)w) - w = 2J(\tau, \nabla^2\phi) - 2J(\phi_x, \tau_x) - 2J(\phi_y, \tau_y), \tag{3.16}$$

which can be derived by eliminating time derivatives in Eqs. (3.9-3.10). It is hard to make any general theoretical statements about the RHS of this equation given the macroturbulent nature of the flow. Unlike in modal theory, scrambling by the nonlinear advective terms means that a simple amplifying feedback between the asymmetry of the RHS and w is no longer expected, and this is supported empirically by both the inversions for the reduced stability and global warming simulations which showed that the RHS was unskewed and made only negligible contributions to the asymmetry of the vertical velocity distribution. Motivated by this result, we study a simple 1-D toy-model of the moist two-layer QG omega equation in the macroturbulent phase given by

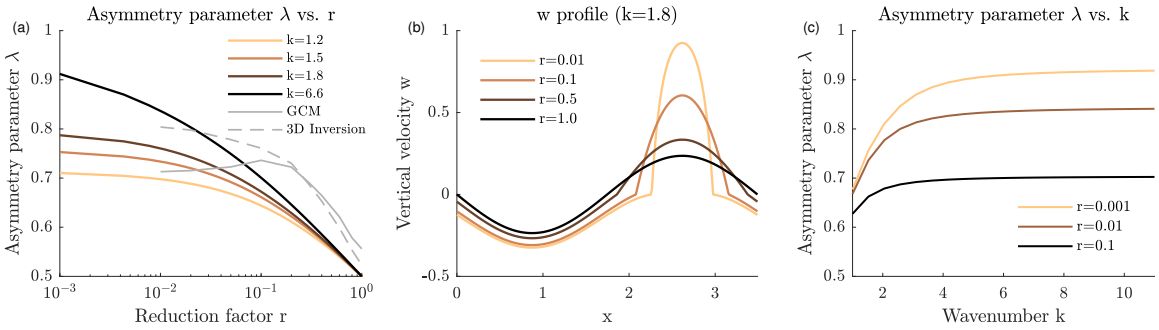

Figure 3-5: (a) Asymmetry parameter λ for the vertical velocity field predicted by the 1-D toy model (Eq. 3.17) for different wavenumbers k as a function of the reduction factor r along with the asymmetry parameter for the reduced stability GCM runs and the 3-D moist QG omega inversions (gray lines, same as in Fig. 3-3a). (b) Corresponding vertical velocity profiles at $k = 1.8$ for different values of r. (c) Asymmetry parameter λ for the vertical velocity field predicted by the 1-D toy model for different values of the reduction factor r as a function of k.

$$(r(w)w)_{xx} - w = \sin(kx), \tag{3.17}$$

with the dynamical forcing on the RHS described by an unskewed sinusoidal function with non-dimensional wavenumber k. Since we currently do not possess a theory for the power spectrum of the RHS, the wavenumber k is taken here as an externally imposed parameter in addition to the reduction factor r. Although the sinusoidal forcing is clearly a gross simplification of the true RHS forcing, we argue that it is nonetheless useful to illustrate some of the controls on λ implied by the moist omega equation with an unskewed RHS forcing at different length scales.

We invert Eq. (3.17) numerically for a given wavenumber k and reduction factor r on a domain of length L$= 2\pi/k$ using 300 evenly-spaced grid points. The solution technique for the moist omega equation is the same as that outlined in section 3.4.1. Results for λ are shown in Fig. (3-5a), and a selection of vertical velocity profiles at fixed $k = 1.8$ and varying r are shown in Fig. (3-5b). The value of $k = 1.8$ has been chosen here for comparison to the reduced stability GCM simulations since it is corresponds to the typical wavenumber found for these simulations at $r = 0.01$. The typical wavenumber was estimated by calculating the centroid wavenumber of

the 1-D zonal w power spectrum $P(k)$ at 500hPa,

$$k_{centroid} = \frac{\sum_{k'} k' P(k')}{\sum_{k'} P(k')}, \tag{3.18}$$

averaging $k_{centroid}$ across the latitude band $25^\circ - 65^\circ$ of the reduced stability simulation, and nondimensionalizing by the deformation radius $L_D = \sqrt{\sigma_{500}}\Delta p/(2\sqrt{2}f)$, where σ_{500} is the static stability factor in pressure coordinates estimated from the reduced stability simulations at 500 hPa, and $\Delta p = 800$ hPa and $f = 10^{-4}\text{s}^{-1}$ were chosen as typical values for the tropopause height and Coriolis parameter, respectively.[3] Focusing on the vertical velocity profile at $k = 1.8$ (see Fig. 3-5b), we see that although the ascent length shrinks as r becomes smaller, the ascent length does not collapse and the vertical velocity profiles do not become very asymmetric, especially compared to the profile of the mode predicted by 1-D theory at $r = 0.1$ (see Figure 3-4b). Looking at the corresponding behavior of $\lambda(r)$ at $k = 1.8$ in Fig. (3-5a), we confirm that the toy model asymptotes to $\lambda \simeq 0.80$ as $r \to 0$ and has a value of $\lambda = 0.76$ at $r = 0.01$. By comparison the 1-D modal theory asymptotes to $\lambda = 1$ as $r \to 0$ (this limit is known from the theory of moist baroclinic modes which predicts vanishing updraft length in this limit Emanuel et al. 1987, Zurita-Gotor 2005) and has a value of $\lambda = 0.95$ at $r = 0.01$ (see Fig. 3-4a). Thus the asymmetries are much higher for modal theory than for the toy-model. The value of $\lambda = 0.76$ predicted by the toy-model at this wavenumber is in reasonably good agreement with that found for the reduced stability GCM simulations $\lambda = 0.71$, and the slight overestimate is consistent with the overestimate found for the 3-D moist QG omega equation inversions in the reduced stability simulations which gave $\lambda = 0.80$ for $r = 0.01$ (Fig. 3-5a, gray lines). We note however that the agreement between the toy-model and GCM asymmetry is not exact. In particular, the toy-model underestimates the GCM asymmetry at large r values ($r > 0.1$), and the toy-model asymmetry does not equilibrate

[3]Note the extra factor of 2 in the definition of the deformation radius because H in our two-layer theory is the layer height and not the tropopause height.

as quickly as r is lowered[4]. The underestimate at larger r values is likely a result of the simplified nature of the RHS forcing (completely unskewed, and single sinusoid) since the full 3-D inversion does a good job at reproducing the GCM asymmetry in this range. The slower equilibration of λ as r is lowered in the toy-model points to a potential deficiency of the moist QG omega framework at capturing all the controls on the vertical velocity field in the GCM, since the full 3-D moist QG omega inversions also show lack of complete equilibration at $r = 0.01$.

Interestingly, looking at Fig. (3-5c), we also note that for a fixed value of r the toy-model implies that λ increases as the wavenumber k is increased (i.e. the forcing moves to smaller length scales), particularly at low values of r. Hence, while the asymmetry parameter asymptotes in the low r limit to values of λ similar to those in the idealized GCM simulations for values of k that are roughly consistent with those found in the simulations, the toy model surprisingly predicts that high values of $\lambda \sim 0.9$ comparable to the modal regime could be reached even in the macroturbulent flow with unskewed RHS provided that r is sufficiently low and the wavenumber of the forcing is sufficiently large ($k > 6$). This intriguing implication will be pursued further in section 3.6 where we present moist simulations with a highly asymmetric vertical velocity field in the macroturbulent regime despite a near symmetric RHS. But first, we will apply the toy-model theory to the seasonal cycle of λ observed in the current climate and contrast it with the predictions from moist baroclinic modes.

3.5 Applying the Toy-Model to the Seasonal Cycle of λ in Reanalysis

We compare the theoretical predictions from the 1-D modal theory and the 1-D toy model to the seasonal cycle of λ found in ERA5 reanalysis at 500hPa in both the Northern Hemisphere (NH) and Southern Hemisphere (SH) (Fig. 3-6). The vertical velocity and temperature data used are 6-hourly fields with grid spacing 0.25°

[4]As a result we chose to plot the asymmetry for the toy-model down to smaller $r = 0.001$ values than were simulated in the idealized GCM.

spanning the latitude band $30° - 70°$ and years $2009 - 2018$. For comparison, we also show the seasonal cycle of λ in ERAI and NCEP2 reanalysis, with a grid spacing of $0.75°$ and $2.5°$ respectively, since the amplitude of the seasonal cycle was found to increase with increasing reanalysis resolution. The asymmetry parameter λ in reanalysis has been calculated at each latitude based on zonal averages and averaged over the latitude band and over the 10 years for each month. For the theoretical predictions, r was calculated from the ERA5 temperature field at 500hPa using Eq. (3.6), and then averaged over the horizontal domain and over the 10 years for each month. The wavenumber k was calculated again as the centroid wavenumber of the 1-D zonal power spectrum of w in ERA5 at 500hPa using Eq. (3.18), and then averaged over the latitude band and over the ten year period for each month. The wavenumber k was then nondimensionalized by the deformation radius $L_D = \sqrt{\sigma_{500}}\Delta p/(2\sqrt{2}f)$, where σ_{500} was estimated as the domain and 10-year average from ERA5 at 500 hPa for each month, and $\Delta p = 800$ hPa and $f = 10^{-4}\mathrm{s}^{-1}$ were again chosen to reflect typical values of the tropopause depth and Coriolis parameter, respectively. Using the values of r and k for each month, the 1-D toy model and 1-D modal theory was solved as described in section 3.4 to produce the theoretical predictions seen in Fig. (3-6).

Looking at Fig. (3-6a, b), we see that λ in ERA5 reanalysis has a seasonal cycle that peaks during summer in each hemisphere. This is as expected given that r decreases as the stratification becomes closer to moist adiabatic in summer (Stone and Carlson 1979), and it is also consistent with the result that λ is larger in summer compared to winter in extratropical cyclones (Tamarin-Brodsky and Hadas 2019). The seasonal cycle is more pronounced in the NH varying between values of $\lambda = 0.59$ and $\lambda = 0.69$, than in the SH where it varies between $\lambda = 0.62$ and $\lambda = 0.64$. Comparing the behavior of λ in ERA5 to ERAI and NCEP2 reanalysis, we note that λ decreases in both the northern and southern hemispheres as we go to reanalysis products with coarser resolution, and this is most pronounced during the hemispheric summer. As a consequence, the amplitude of the seasonal cycle decreases with coarser resolution and this is particularly evident in the NH. While a seasonal cycle is still

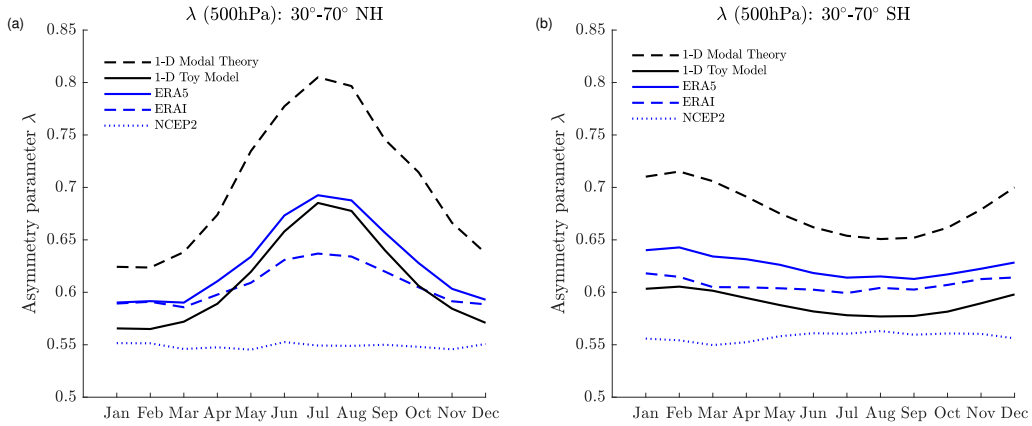

Figure 3-6: (a) Comparison of the seasonal cycle of the asymmetry parameter λ at 500hPa in the Northern Hemisphere (NH) from ERA5 reanalysis which has a grid spacing of 0.25°, to the predictions from the 1-D toy model and 1-D modal theory. For comparison, we also show the seasonal cycle of λ in ERAI reanalysis which has a grid spacing of 0.75°, and NCEP2 reanalysis which has a grid spacing of 2.5°. 6-hourly fields were used for all reanalysis data. (b) Same but for the Southern Hemisphere (SH).

found for ERAI, λ remains close to constant throughout the year for NCEP2. A dependence of λ on resolution has also been found in the idealized GCM simulations O'Gorman et al. (2018), but in those simulations it was found that vertically averaged λ was already converged at a resolution of T127, which is coarser than the ERAI resolution of T255. The discrepancy in convergence resolution may arise because different numerical details (e.g., use of a semi-Lagrangian scheme in ERAI) lead to a coarser effective resolution in reanalysis versus the GCM, and additionally there may be more sensitivity to resolution of λ at 500hPa compared to the vertical average λ (Booth et al., 2015). The question still remains whether future reanalysis products with much higher resolution than ERA5 could show a substantially larger seasonal cycle of λ. We do not anticipate this to be the case because Booth et al. (2015) found that vertically averaged λ did not increase from a grid spacing of 50km to 3.125km in simulations of a moist baroclinic lifecycle, and λ at $z = 5$km only increased slightly over this range of grid spacings.

Even though a seasonal cycle of λ can be found in ERA5, its magnitude remains small in both hemispheres from the point of view of modal theory given that r un-

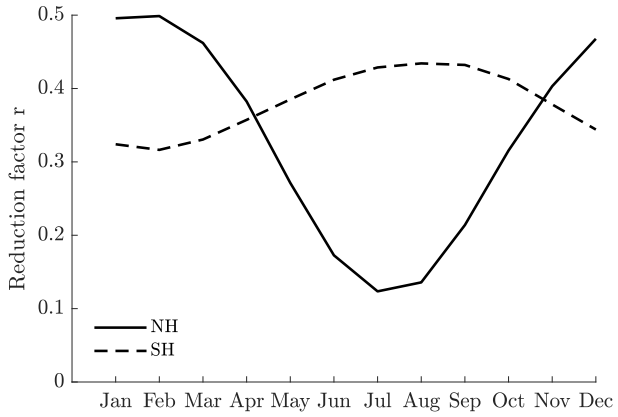

Figure 3-7: Seasonal cycle of the static stability reduction factor r in the northern (solid) and southern (dashed) hemisphere at 500hPa in ERA5 reanalysis. The reduction factor has been averaged between latitudes $30° - 70°$. $r = 1$ corresponds to a dry atmosphere, and $r = 0$ corresponds to a moist atmosphere with a moist adiabatic lapse rate. In both hemispheres r is smallest during the summer, but the seasonal cycle is more pronounced in the NH.

dergoes large variations between winter and summer months ($0.12 < r < 0.5$ in the NH and $0.32 < r < 0.43$ in the SH, Fig. 3-7). Indeed, 1-D modal theory consistently overpredicts λ in both hemispheres reaching peak values of $\lambda = 0.80$ in the NH and $\lambda = 0.71$ and in the SH. This is in line with the results of the idealized GCM simulations which showed that variations of λ in the macroturbulent state with warming are considerably smaller than what moist modal theory predicts. In contrast to the modal theory, the seasonal cycle in reanalysis is better captured by the 1-D toy model, particularly in the NH. From the point of view of the 1-D toy model, the seasonal cycle in λ is primarily from the variations in r because variations of k (between 5.6 and 7.7 in the NH, and between 4.2 and 4.8 in the SH) only have substantial effect on λ at smaller values of r (compare the variations of λ with k predicted by the toy-model at $r = 0.01$ and $r = 0.4$ in Fig. 3-5a).[5]

Although the close quantitative agreement in the NH is likely a bit serendipitous given the simplicity of the model and the sinusoidal RHS, we argue that the toy model, in contrast to moist modal theory, better captures the moderate sensitivity of λ to warming that is characteristic of the macroturbulent regime.

[5]This was further checked by calculating λ from the toy modal keeping k fixed over the seasonal cycle. The results in Fig. 3-6 were unaffected.

3.6 High λ States in Moist QG Turbulence

The 1-D toy model of the moist omega equation predicts that the vertical velocity field can become very asymmetric even for an unskewed RHS forcing in the low r limit provided that the wavenumber of the RHS forcing is sufficiently large. In this section, we show that such flow regimes are indeed achievable by presenting results from moist two-layer QG simulations.

We solve the moist two-layer QG Eqs. (3.8-3.10) on a doubly-periodic domain of size $L = 12\pi$ with 512x512 grid points using Dedalus, a flexible framework for numerical simulations with spectral methods (Burns et al. 2020). The system is allowed to go moist baroclinically unstable about a mean temperature gradient in thermal wind balance, which corresponds to $\bar{\tau} = -y$, $\bar{\phi} = 0$ and $\bar{w} = 0$. We set $\tau = \bar{\tau} + \tau'$, $\phi = \phi'$, $w = w'$, and add additional terms for dissipation and β as described below. Eqs. (3.8-3.10) take the form

$$\partial_t \nabla^2 \phi + J(\phi, \nabla^2 \phi) + J(\tau, \nabla^2 \tau) + \beta \phi_x = -\nabla^2 \tau_x - \frac{R}{2} \nabla^2 (\phi - \tau) - \mu \nabla^4 (\nabla^2 \phi) \tag{3.19}$$

$$\partial_t \nabla^2 \tau + J(\phi, \nabla^2 \tau) + J(\tau, \nabla^2 \phi) + w + \beta \tau_x = -\nabla^2 \phi_x + \frac{R}{2} \nabla^2 (\phi - \tau) - \mu \nabla^4 (\nabla^2 \tau) \tag{3.20}$$

$$\partial_t \tau + J(\phi, \tau) + r(w) w = \phi_x - \mu \nabla^4 \tau + \nu \nabla^{-2} \tau \tag{3.21}$$

where we have dropped all the primes for notational simplicity, and ϕ, τ and w represent perturbations about the mean state. The equations have been nondimensionalized with the deformation radius L_D (as before) and the velocity scale U which is the basic state velocity in each layer (U in the top layer, and $-U$ in the bottom layer). Eqs. (3.19-3.21) include the effects of a linear drag on the vorticity in the lower layer with nondimensional drag coefficient $R = R_{dim} L_D / U$ where R_{dim} is the dimensional drag coefficient; the β-effect with $\beta = \beta_{dim} L_D^2 / U$ where β_{dim} is

the dimensional β parameter; small-scale dissipation parametrized by a fourth-order hyper-diffusion with coefficient ν; and a large-scale radiative damping parametrized by a hypo-diffusion made up of an inverse diffusion operator with coefficient ν. The large-scale radiative damping was found to be necessary for simulations with $r < 0.4$ and thus large energy input from latent heating because the linear drag term was not enough to remove the energy at large scales and stabilize the simulations. The means of the stream functions ϕ and τ, and the mean of w are all enforced to be zero.

The system of equations differs from the moist QG equations of Lapeyre and Held (2004) primarily by always assuming upward motion to be saturated. Thus, no prognostic moisture equation is needed, and the effects of latent heating are captured in terms of a single parameter r. So far the r parametrization has been used in studies of moist baroclinic instability (Emanuel et al. 1987, Montgomery and Farrell 1991, Montgomery and Farrell 1992, Fantini 1995, Moore and Montgomery 2004, Kohl and O'Gorman 2022) with the exception of O'Gorman et al. (2018) which also considered a macroturbulent state. To our knowledge, this is the first time that the r-parametrization has been applied to macroturbulent simulations in a 2-layer model. We choose this system here for its simplicity and ease of comparison to moist baroclinic theories, but acknowledge that having a prognostic moisture equation, like in Lapeyre and Held (2004), allows for conservation properties that are more desirable when developing closure theories for PV fluxes (which is not our focus here).

We show result for simulations with $r = 1$ (a dry simulation) and $r = 0.01$ (a moist simulation with strong latent heating). We fix $\beta = 0.78$ equal to the value of Lapeyre and Held (2004).[6] This corresponds to a moderate supercriticality of $\chi = \beta^{-1} = 1.28$, where $\chi > 1$ is required for the inviscid dry model to go unstable. We pick $R = 0.11$, $\mu = 10^{-5}$, and $\nu = 0$ for $r = 1$ and $\nu = 5$ for $r = 0.01$. The simulations are started using random initial conditions for the stream functions ϕ and τ, where we have filtered out all wavenumbers with $k = \sqrt{k_x^2 + k_y^2} > 3$ to avoid having to integrate a lot of small scale noise in the initial phase of the simulation. After an initial phase of

[6]Please note that compared to Lapeyre and Held (2004), our deformation radius is defined as $L_D = NH/(\sqrt{2}f)$ instead of $L_D = NH/f$ but the magnitude of our mean flow is U instead of their $U/2$ so that the definition of $\beta = \beta_{dim} L_D^2/U$ is equivalent.

modal instability, the simulations settle into a macroturbulent state. This happens more quickly at $r = 0.01$ because the growth rate of the modes is increased by latent heating.

We begin by comparing the structure of the flow field in the two simulations. The relative vorticity in the upper and lower layer, alongside the vertical velocity are shown in Fig. (3-8).

Looking at the dry simulation (Fig. 3-8a,c,e), we see that the flow settles into the well known state of β-plane turbulence: wavy jets interspersed with vortices. The relative vorticity is weaker in the lower than upper layer because of the low level drag. The vertical velocity field has large-scale ascending and descending regions of similar size that are mostly confined to the latitudes of the jets.

In contrast to the dry simulation, we see that the flow in the moist simulation (Fig. 3-8 b,d,f) has transitioned to a state that is entirely dominated by small scale vortices, despite the presence of low level drag and β, with greatly reduced ascent lengths and strong ascending motion. In fact when β was changed down to $\beta = 0$ and up to $\beta = 1.5$ in the moist simulations at $r = 0.01$, there was no noticeable effect on the overall flow field or the asymmetry of the vertical velocity field (not shown).[7] The vortices propagate northwards in our simulations through nonlinear advection and the trails of this propagation can be seen in the form of tendrilly north-south structures in the vertical velocity field. The PV structure of the vortices consists of dipoles of positive PV anomalies in the lower layer and negative PV anomalies in the upper layer maintained by diabatic generation with meridional PV advection playing a negligbe role (not shown - discussed in section 4.2) like in a diabatic Rossby vortex (e.g., Kohl and O'Gorman 2022). A similar transition to a vortex dominated state has first been observed by Lapeyre and Held (2004) in a moist-two layer QG system using prognostic moisture. However, unlike here the authors found that the vortices had a barotropic vertical structure, and the vorticity field had a much stronger tendency towards cyclones in the lower layer, than towards anticyclones in the top layer while

[7] As explored in the next chapter, baroclinic tendencies in the PV budget are dominated by diabatic effects in these simulations so that making small changes to β like this are unimportant.

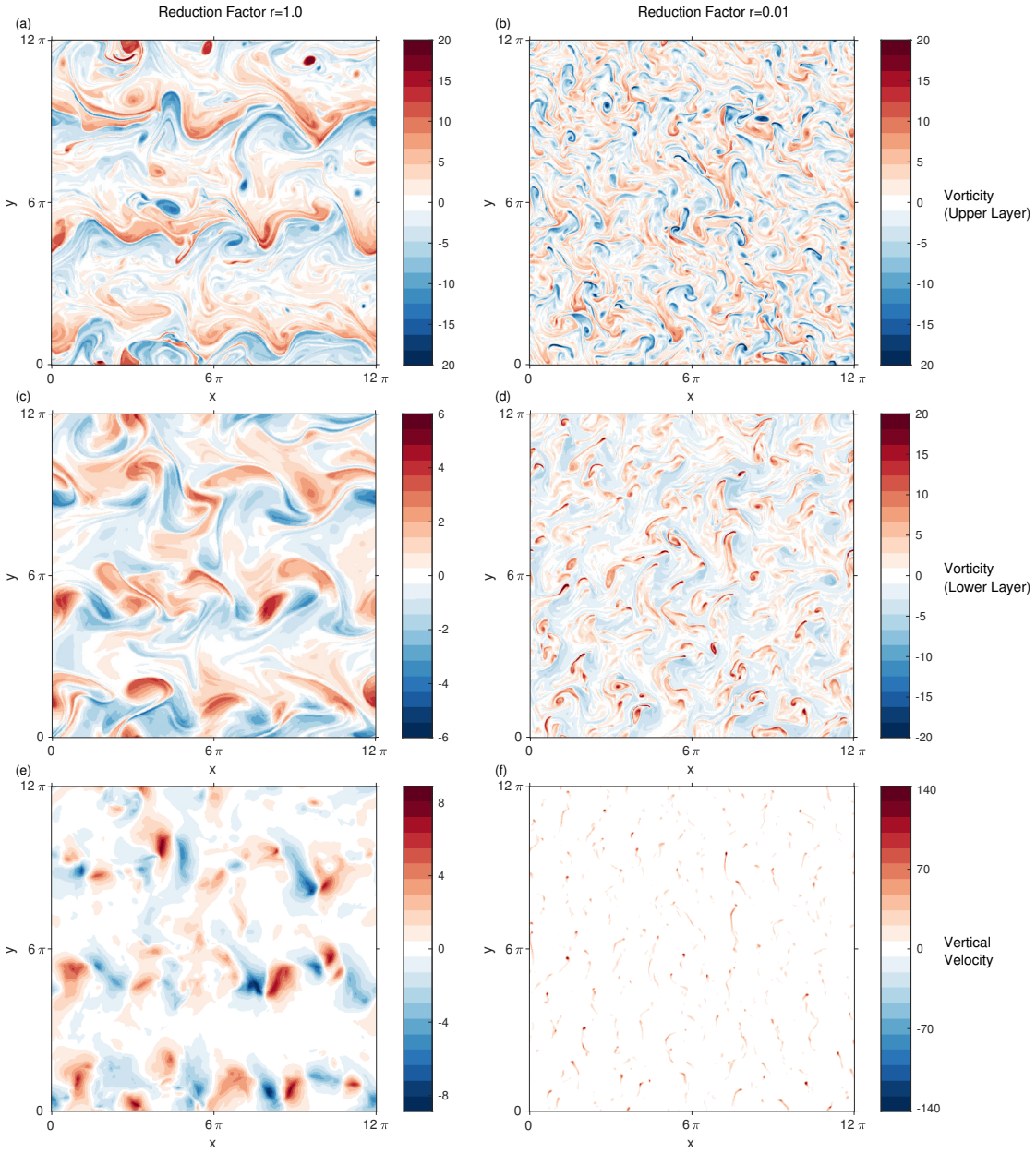

Figure 3-8: Snapshots of relative vorticity in the upper layer (a,b) and lower layer (c,d), and vertical velocity (e,f) in the moist two-layer QG simulations at $r = 1.0$ (a,c,e) and $r = 0.01$ (b,d,f). Note that vorticity in (c) has a different colobar scale from (a,b,d) and that the vertical velocity has a very different colorbar scale in (f) compared to (e). The flow transitions from a wavy jet state interspersed with vortices at $r = 1.0$ to a vortex dominated flow at $r = 0.01$. The vortices migrate poleward over time leaving a trail that can be seen in the vertical velocity.

it is roughly similar in our simulations (not shown). Although we only show the results at $r = 0.01$, we note that the transition to a vortex dominated flow happens at values of roughly $r = 0.4$. This is also the threshold that was found for DRVs to be the most unstable mode in the tilted moist 2-layer model on an infinite domain Kohl and O'Gorman (2022), but that might be coincidental because that result assumed no PV gradients in the basic state.[8] For values of r lower than 0.4, the main effect of decreasing r is to reduce the length scale of the vortices and the length scale of ascending motion.

Although much could be explored about the properties of the moist turbulent simulations in future work, our focus here is on the asymmetry of the vertical velocity field in the $r = 0.01$ simulation. Fig. (3-9) shows the value of λ versus time for the vertical velocity field, and the vertical velocity field w_{RHS} which results from solving the moist omega equation

$$\nabla^2(r(w)w) - w = \text{RHS} \tag{3.22}$$

specifying $r(w) = 1$ such that the asymmetry only comes from the RHS. Here RHS$=2\nabla^2\phi_x + 2J(\tau, \nabla^2\phi) - 2J(\phi_x, \tau_x) - 2J(\phi_y, \tau_y) + \beta\tau_x$ and we have neglected dissipative terms. The transition from modal to macroturbulent state of the simulations can be seen in the asymmetry of the w_{RHS}. After the asymmetry of w_{RHS} increases in the modal phase and reaches its peak ($t = 5$), it decreases and w_{RHS} becomes close to symmetric in the macroturbulent state of the simulation ($t > 5$). This is consistent with the decrease of the RHS contribution to the vertical-velocity asymmetry that has been observed in the idealized GCM simulations of O'Gorman et al. (2018) discussed in section 3.3. Furthermore the skewness of -RHS decreases from 9.0 to 0.4 consistent with the assumption that has been made in the development of the simple 1-D toy

[8]For the moist two-layer QG model with PV gradients no obvious threshold from wave to vortex modes was found at $r = 0.4$ (see Fig. 2-9a). However, it is possible that the finite amplitude vortices are different from the modes in this regard because meridional advection was found to be stronger relative to latent heating for the modes than the storms (not shown). This could make the fully tilted model - without PV gradients - a better analogy for the fully turbulent simulations.

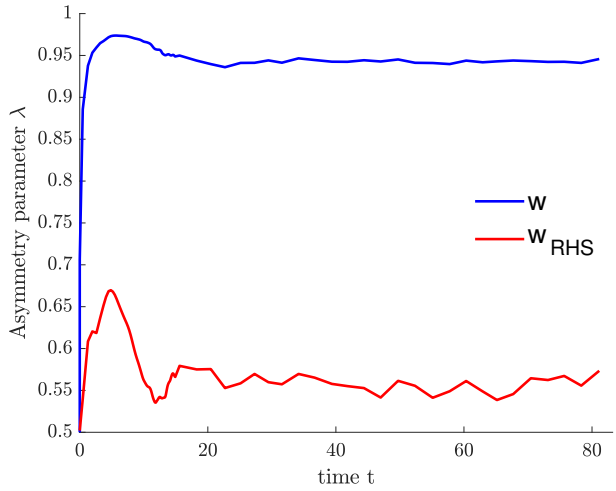

Figure 3-9: Asymmetry parameter of the vertical velocity field w versus time in the moist QG turbulent simulations at $r = 0.01$. Also shown is the asymmetry parameter for the vertical velocity field that is contributed just by the RHS of the moist omega equation Eq. (3.22) with $r(w) = 1$.

model for the macroturbulent regime in section (3.4.2). Even though the RHS makes little contributions to the asymmetry of w in the macroturbulent regime, the asymmetry remains very large in the macroturbulent phase at $\lambda = 0.94$ (Fig. 3-9). This is also confirmed by looking at the vertical velocity snapshot in Fig. 3-8f in which there are very small updraft areas and very strong updraft speeds. Diagnosing the value of the wavenumber k in these simulations from the centroid of the meridionally and time averaged zonal power spectrum of w using Eq. (3.18), we find that $k = 6.6$ which leads to a toy model prediction of $\lambda = 0.84$ for $r = 0.01$. This is a high value of λ, albeit lower than the value of $\lambda = 0.94$ found in the simulation. For $k = 6.6$ and $r \to 0$, the toy-model predicts $\lambda \simeq 0.97$ implying highly asymmetric vertical velocity distributions are possible at high values of k and low values of r.

Consistent with the predictions of the toy model, we find that high asymmetry states are indeed achievable in the macroturbulent state even for unskewed RHS forcings so long as the wavenumber of the forcing is sufficiently large. Our moist QG simulations suggest that such a flow regime is characterized by a 'vortex world' which is quite different from that observed in the idealized GCM which retains a predominantly wave-like structure even in warm and moist climates. We will address

this discrepancy in the next chapter.

3.7 Conclusions

Idealized GCM simulations of moist macroturbulence show that the asymmetry of the vertical velocity distribution is considerably smaller than what moist baroclinic instability theory predicts. This is significant given that the atmosphere is constantly in a state more akin to that of the macroturbulent simulations. Meanwhile, our theoretical understanding is based around moist modal theory which is not applicable in this regime. This makes the development of a theory for the asymmetry in the macroturbulent state desirable.

To bridge this gap in understanding, we have applied inversions of a moist QG omega equation to the idealized GCM output to identify why the asymmetry is reduced in the modal compared to macroturbulent regime. The inversions showed that while the RHS of the omega equation remains very skewed in the modal regime, it contributes negligibly to the asymmetry in the macroturbulent phase which is almost entirely determined by the reduction in static stability in ascending air on the left hand side of the moist omega equation.

The two-layer moist QG framework was then used to understand asymmetry behavior. We showed that in the modal regime, a feedback between the dynamical forcing on the RHS and w leads to large asymmetries contributed by the RHS consistent with what was found in the idealized GCM simulations. Such a feedback is not expected for the macroturbulent phase because of advective nonlinearities in the RHS of the moist omega equation. We then distilled the insights from the moist omega inversions and in particular the unskewed RHS in the macroturbulent phase, into a simple 1-D toy model of the moist QG omega equation. The toy model was solved for a given wavenumber of the dynamical forcing on the RHS of the omega equation and for a given static stability reduction factor r. In contrast to the 1-D moist modal theory, the toy model was able to reproduce the weak increase of the asymmetry with warming that has been observed in the macroturbulent regime of the idealized GCM

simulations.

The asymmetry parameter λ increases from winter to summer in reanalysis and this seasonal cycle forms a useful test ground for asymmetry theories, since the moist static stability varies a lot between seasons, particularly in the NH. We showed that whilst moist baroclinic theory overpredicts the change in λ, the toy-model better reproduces the slow change of λ over the seasonal cycle in ERA5 reanalysis. The interpretation is once again that asymmetry changes in macroturbulent flows in response to changes in moist static stability are much smaller than what moist unstable baroclinic modes suggest. The seasonal cycle of λ is considerably weaker in earlier generations of reanalysis products at coarser resolution. Results from modeling studies of resolution dependence suggest that λ should be converged or close to converged with respect to increases in resolution for the ERA5 reanalysis, but further study of the resolution dependence of λ would be helpful.

While the dynamical forcing (RHS) assumed in the toy model is highly idealized, we argue that it is nonetheless useful to illustrate the controls on the asymmetry implied by the moist QG omega equation. In particular we showed that the toy model predicts that high macroturbulent asymmetries are possible even for unskewed RHS forcing provided that r is sufficiently low and the length scale of the RHS is sufficiently small compared to the dry deformation radius. We showed that this prediction is borne out by macroturbulent simulations of the moist QG equations. When the flow is sufficiently moist, the system transitions from classic beta plane turbulence with jets and vortices, to a vortex dominated regime with highly skewed vertical velocity fields. Taking into account the shift of the dynamical forcing of the moist omega equation to smaller length scales, the vertical-velocity asymmetry in the simulation were consistent with those predicted by the toy model.

Our toy model theory is not closed since it does not predict the length scale of the RHS but rather treats it as an externally imposed parameter. Understanding what sets this length scale thus remains an important outstanding problem for future work. Progress on this question could be made by running simulations of moist primitive equations at different Rossby number and studying how higher order terms beyond

QG affect the length scale of the forcing.

3.8 Appendix

3.8.1 Derivation of the Moist QG Omega Equation

We start from the omega equation with external diabatic heating,

$$\nabla^2(\sigma\omega) + f_0^2\omega_{pp} = \text{RHS} - \frac{\kappa}{p}\nabla^2 J, \tag{3.23}$$

where J is the diabatic heating and κ is the ratio of the gas constant to specific heat capacity at constant pressure (Holton 2004). Using the r parameterization for latent heating and neglecting other diabatic heating, the thermodynamic equation is given by

$$T_t + uT_x + vT_y - r(\omega)S_p\omega = 0 \tag{3.24}$$

where $S_p = -\frac{T}{\theta}\theta_p$. Rearranging the thermodynamic equation to make the heating term explicit, we obtain

$$T_t + uT_x + vT_y - S_p\omega = -(1 - r(\omega))S_p\omega \equiv \frac{J}{c_p} \tag{3.25}$$

from which it follows that

$$J = -(1 - r(\omega))c_p S_p\omega = -\frac{p}{\kappa}(1 - r(\omega))\sigma\omega, \tag{3.26}$$

where we have used the relation $c_p S_p = \frac{p}{\kappa}\sigma$ to obtain the second equality. Plugging this expression for J into Eq. (3.23) and combining the heating term on the RHS

with the static stability term on the LHS of Eq. (3.23), we obtain the moist omega equation (Eq. 3.2) in the text in which latent heating is now represented as an internal process.

Chapter 4

Diabatic Rossby Vortex World: Finite Amplitude Effects in Moist Cyclogenesis

4.1 Introduction

The theory for the growth rate, length scale and wave-vortex transition of Diabatic Rossby Vortices (DRVs) in Kohl and O'Gorman (2022) is based around assumptions of small-amplitude disturbances. It is not clear a priori to what extent the results are able to fully describe the dynamics of DRVs throughout their life cycle from genesis to mature storms, and the conditions under which macroturbulent flows transition to a DRV dominated regime, referred to as DRV world from here on. Comparisons between DRV modes and DRV storms at finite amplitude revealed similarities but also important differences in the structure of the PV anomalies and PV generation. Most notably the negative PV anomaly and negative diabatic generation were found to be much weaker than their positive counterparts in observed storms compared to the moist-quasigeostrophic DRV modes, where positive and negative PV anomaly and generation are the same magnitude. This asymmetry in magnitude could be reconciled by taking into account higher order terms in the PV dynamics, most notably

vertical advection of perturbation PV and stretching of relative vorticity which leads to the absolute, rather than the planetary vorticity, multiplying the heating gradient. In this chapter, we explore the role of finite amplitude effects in moist cyclogenesis in a hierarchy of different models including a simple 1d model for the vertical structure of PV in DRVs, simulations of moist macroturbulence using the quasigeostrophic equations and simulations of moist macroturbulence using the primitive equations. The spirit of the simulations is to keep the representation of moist physics as simple as possible by sticking to the reduced stability parametrization from modal theory, while gradually introducing higher order terms in the PV dynamics beyond that of small-amplitude modal theory. In section 4.2, we begin by analyzing the PV structure and PV budget of the storms in the strong latent heating regime of the moist quasigeostrophic (QG) simulations presented in thesis chapter 3. In the next section 4.3, we study moist primitive equation simulations at a high and a low Rossby number regime to study the effect that higher-order effects beyond QG have on the structure of diabatically driven storms, and the overall character of the macroturbulent circulation. In section 4.4, we distill higher order effects into a toy model of the vertical structure of PV in DRVs that is solved to reproduce much of the variety of the PV structure of DRV storms that has been seen in reanalysis in chapter 2 and idealized simulations from this chapter. We summarize our results in section 4.5 and discuss future work.

4.2 DRVs in Simulations of Moist Quasigeostrophic Turbulence

A natural extension of the 2-layer moist quasigeostrophic theory of DRV modes is to run simulations of moist quasigeostrophic turbulence. The simulations have been described in thesis chapter 3, and only some of the salient results will be repeated here. As the reduction factor is decreased, or the latent heating is increased, the flow transitions from the well-known state of beta plane turbulence with wavy jets

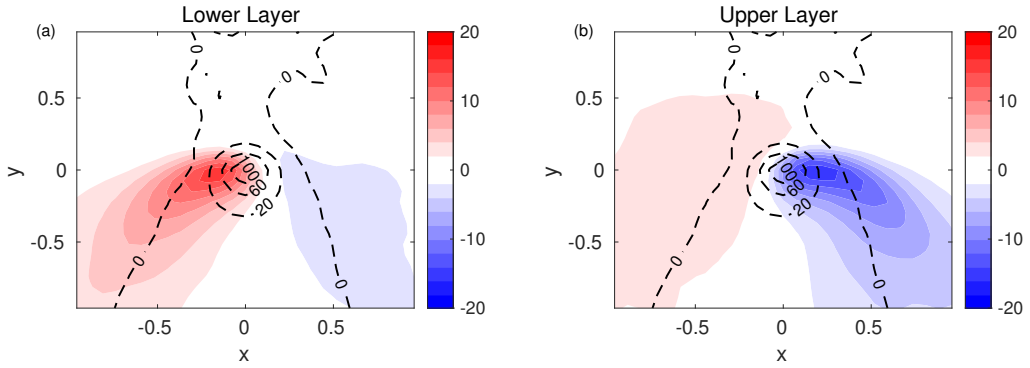

Figure 4-1: Storm composite of the PV anomaly (shading) in (a) the lower layer, and (b) the upper layer of the moist QG turbulence simulations at $r = 0.01$. The vertical velocity is also shown (dashed contour). Composites were created by averaging over the 10 strongest vertical velocity maxima at each simulation output between $t = 22 - 71$ (41 outputs in total) when the simulation had reached a macroturbulent state.

interspersed with vortices to an entirely vortex dominated flow in which the vortices propagate poleward without being confined to a particular latitude band. In this vortex regime, the vertical velocity field is characterized by strong and narrow updrafts with significant asymmetry despite a nearly unskewed dynamical forcing on the RHS of the moist omega equation. Changes in the β-parameter had no significant effect on the dynamics in the strong latent heating regime that we investigated ($r = 0.01$). Here we take a closer look at the PV structure and dynamical balances of the vortices in the strong latent heating regime.

Fig. 4-1 shows the storm composite of PV anomaly and vertical velocity field in the upper and lower layer of the moist QG runs at $r = 0.01$. Composites were created by averaging over the 10 strongest vertical velocity maxima at each simulation output between $t = 22 - 71$ (41 outputs in total) when the simulation had reached a macroturbulent state. The PV takes on the typical dipole structure of DRV modes with a positive PV anomaly in the lower layer and a negative PV anomaly in the top layer. The PV anomalies are displaced horizontally such that the updraft occurs east of the low level positive PV anomaly and west of the upper level negative PV anomaly.

Further insights into the dynamical balances maintaining the storms can be ob-

tained by studying the tendencies in the PV budget. In the lower layer, the PV budget is given by

$$\partial_t q_2 = q_{2x} - v_2 \bar{q}_{2y} - J(\psi_2, q_2) + (1 - r(w))w - R\nabla^2 \psi_2, \tag{4.1}$$

where $q_2 = \nabla^2 \psi_2 + 0.5(\psi_1 - \psi_2)$ is the potential vorticity in the lower layer (total, not the deviation from the zonal mean), $\partial_t q_2$ is the time tendency of the PV in the lower layer, q_{2x} is PV advection by the mean zonal wind, $-v_2 \bar{q}_{2y}$ is the advection of the mean PV gradient by the meridional wind ($\bar{q}_{2y}$ includes contributions from both the mean temperature gradient and β), $-J(\psi_2, q_2)$ is the nonlinear advection, $(1-r(w))w$ is the diabatic PV tendency, and $-R\nabla^2\psi_2$ is the drag term. We have ignored the large scale radiative forcing and hyperdiffusion terms which were found to be small. The composite of the PV tendencies in the lower layer are shown in Fig. 4-2 centered on the vertical velocity maximum. The PV tendencies are dominated by mean zonal PV advection, nonlinear advection and diabatic heating. Both the drag term, and the meridional advection of mean meridional PV gradients play a negligible role. This confirms the strong diabatic character of the storms in this regime of the simulations.

We note that the updraft velocity becomes very large compared to horizontal geostrophic velocities for the simulations at $r = 0.01$, and the ratio w/v of nondimensional velocities is of the order of $\mathcal{O}(50)$. This is inconsistent with QG scaling $u_{ag}/u_g = \epsilon w/v$, where u_{ag}/u_g is the ratio of dimensional ageostrophic to geostrophic horizontal winds, unless the Rossby number ϵ is very small so that $u_{ag}/u_g << 1$. However, a transition to DRV world in the moist QG system is also found at $r = 0.1$, in which case it is found that $w/v = \mathcal{O}(5)$ which would allow for a reasonable Rossby number.

Fig. 4-3 also shows a cross-section through the PV tendencies of Fig. 4-2 averaged between $-0.2 < y < 0.2$. From left to right, we observe that in the descending part of the solution to the west ($-1 < x < -0.3$), where the diabatic generation is zero, the PV tendency is given by the sum of mean zonal and nonlinear advection (with

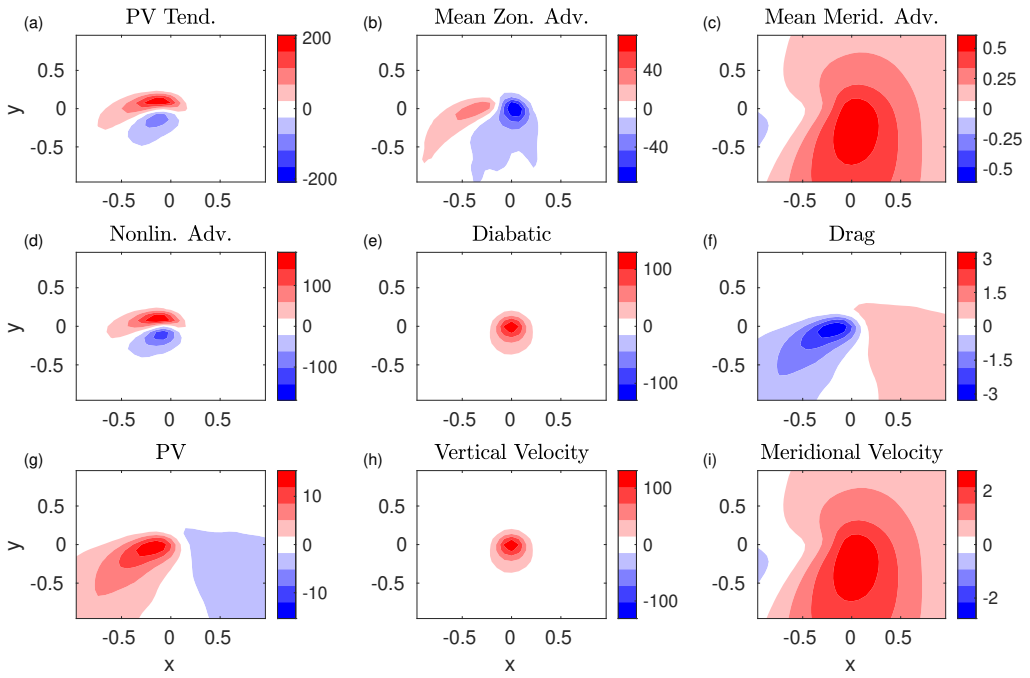

Figure 4-2: Composite of the PV tendencies in the lower layer showing (a) PV tendency q_{2t}, (b) mean zonal advection q_{2x}, (c) mean meridional advection $-v_2\bar{q}_{2y}$, (d) nonlinear advection $-J(\psi_2, q_2)$, (e) diabatic generation $(1-r(w))w$, (f) drag $-R\nabla^2\psi_2$ for the storms in the 2-layer moist QG turbulent simulation at $r = 0.01$. Also shown are (g) the low-level PV q_2, (h) midlevel vertical velocity w, and (i) low-level meridional velocity v_2 to help interpretation. In this latent heating drive regime of the simulations, diabatic effects dominate over mean meridional advection, which remains small. This is also true in the upper level where the mean PV gradient is stronger (not shown). Composites were created by averaging over the 10 strongest vertical velocity maxima at each simulation output between $t = 22 - 71$ (41 outputs in total) when the simulation had reached a macroturbulent state.

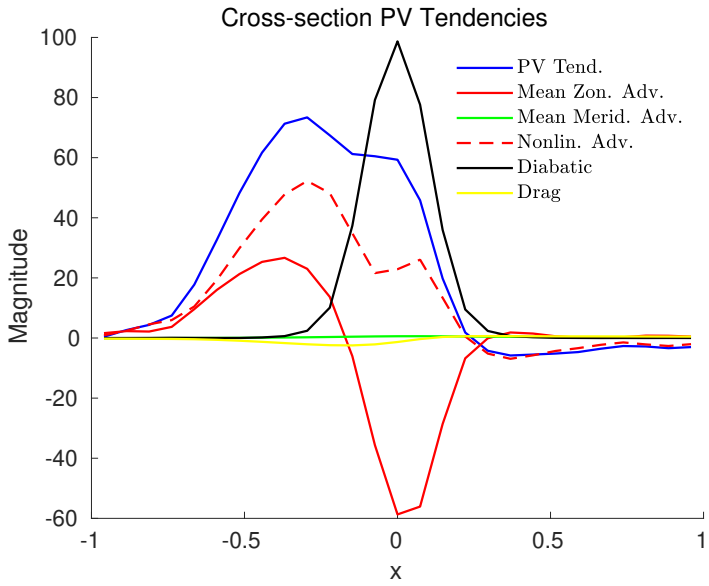

Figure 4-3: Slice through the PV tendencies shown in Fig. (4-2) averaged between $-0.2 < y < 0.2$.

nonlinear advection the slightly more dominant contribution). In the ascending part of the solution ($-0.3 < x < 0.3$), the PV tendency is the result of a three way balance between diabatic generation, zonal and nonlinear advection. Here mean zonal PV advection plays a more dominant role than nonlinear advection. To the east of the ascent area ($0.3 < x < 1$), a negative PV tendency is caused by nonlinear advection with all other terms being negligible.

The dynamical balances governing the storms in this regime of the simulation are very similar to that of the DRV mode, with the additional effect of nonlinear advection, which leads us to the conclusion that they are indeed DRVs. Looking at the structure of the nonlinear advective tendency in Fig. 4-2d, we see that it propagates the solutions poleward. This strong poleward self advective tendency breaks the latitudinal confinement and is not found as strongly for the DRV storms in the current climate, which have a more zonal propagation. However, it is found for the DRV storm in the warm climate regime of idealized simulations (its PV structure was discussed in chapter 2). Self-advection relies on the interaction between lower and upper positive PV anomalies.[1] We speculate that such poleward self-advection

[1]The self-advection by two opposite signed QG PV anomalies in different layers is like that of 'hetons' as discussed in Hogg and Stommel (1985).

is weaker in DRVs in the current climate, because of reduced upper level negative PV anomalies.

Similar results for the vertical PV structure and the dynamical balances have been found by compositing on the low level PV anomaly, rather than the vertical velocity, with the exception that the upper level negative PV anomaly is weakened compared to the low level PV anomaly, and the PV tendency points northwestward instead of northward (not shown).

4.3 DRVs in Turbulent Simulations of Moist Primitive Equation

We now investigate strong diabatic storms in a set of more realistic simulations using the moist primitive equations. After nondimensionalization, the governing parameter that will be investigated is the Rossby number. Switching between high and low Rossby number regimes, while maintaining strong latent heating, will allow us to investigate the role of higher order terms in the PV dynamics beyond QG.

4.3.1 Model Formulation

The moist primitive equations in Boussinesq form, with constant planetary vorticity and r-parametrization take the form

$$\frac{D\mathbf{u}}{Dt} + \mu_u \nabla^2 \nabla^2 \mathbf{u} + f_0 \mathbf{k} \times \mathbf{u} = -\nabla\phi - R\,\mathbf{u}, \tag{4.2}$$

$$\frac{D\theta}{Dt} + \mu_\theta \nabla^2 \nabla^2 \theta = (1-r) w \theta_z - \alpha\,(\theta - \theta_r), \tag{4.3}$$

$$u_x + v_y + w_z = 0, \tag{4.4}$$

$$\frac{g}{\theta_0}\theta = \phi_z, \tag{4.5}$$

$$\frac{D}{Dt} = \partial_t + u\partial_x + v\partial_y + w\partial_z, \tag{4.6}$$

$$\theta_r = \frac{z\theta_0 N^2}{g} - \frac{\theta_0}{g}\frac{fU}{H}\frac{L_y}{2\pi}\cos\left(\frac{2\pi}{L_y}y\right), \tag{4.7}$$

where $\mathbf{u} = (u, v)$ is the horizontal velocity field, w is the vertical velocity field, ϕ is the geopotential height, θ is the potential temperature, θ_0 is the reference potential temperature, θ_r is a zonally uniform reference state that is constant in time, f_0 is the constant rotation rate, $r(w)$ is the nonlinear reduction factor, α is a relaxation constant, g is the gravitational constant, H is the tropospheric height, U/H is the shear implied by thermal wind for the reference θ_r profile, N is a constant static stability, L_y is the domain length in the meridional direction, and μ are coefficients for horizontal hyperdiffusion.

The equations are being forced by relaxing θ at a rate α to a reference state θ_r which corresponds to a constant static stability in the vertical and a cosinusoidal function in the meridional direction. The cosinusoidal forcing is chosen to allow the equations to be solved on a doubly periodic domain in the horizontal using the spectral solver Dedalus (Burns et al. 2020). In the vertical, the domain is bounded by vertical plates at $z = 0, H$ with boundary condition $w = 0$, where H now represents the full tropospheric depth. A linear drag and small-scale dissipation is applied in the momentum equations. The β-plane term is neglected here, since it would introduce a linear term in the momentum equations that cannot be represented by the doubly-periodic solver. While it would be possible to solve a system of equations with the solver where the Coriolis parameter $f \propto \sin(2\pi y)$ is allowed to vary fully with latitude, we stick to the $f = f_0$ configuration for simplicity, and to avoid introducing Hadley

cells.

Anticipating that the average stratification does not scale in the same way as the deviations from it, we let

$$\theta = \bar{\theta}(z) + \theta'(x, y, z, t) \tag{4.8}$$

$$\theta_r = \bar{\theta}_r(z) + \theta'_r(y) \tag{4.9}$$

with $\bar{\theta}(z) = \bar{\theta}_r(z) = \frac{z\theta_0 N^2}{g}$ and $\theta'_r = -\frac{\theta_0}{g}\frac{fU}{H}\frac{L_y}{2\pi}\cos\left(\frac{2\pi}{L_y}y\right)$.[2] This gives

$$\frac{D\theta'}{Dt} + w\bar{\theta}_z + \mu_\theta \nabla^2\nabla^2\theta' = (1-r)w\bar{\theta}_z + (1-r)w\theta'_z - \alpha\,(\theta' - \theta'_r). \tag{4.10}$$

We then let $\phi = \bar{\phi} + \phi'$ where $\bar{\phi}$ is hydrostatically balanced by $\bar{\theta}$, and the hydrostatic equation becomes

$$\frac{g}{\theta_0}\theta' = \phi'_z. \tag{4.11}$$

Next, we nondimensionalize the equations using QG scaling but keeping all terms $x, y \sim L_D$ with deformation radius $L_D = NH/{f_0}^3$, $z \sim H$, $t \sim L_D/U$, $\mathbf{u}, \mathbf{v} \sim U$, $w \sim \epsilon UH/L_D$ where $\epsilon = U/f_0 L_D$ is the Rossby number, $\phi \sim f_0 U L_D$, $\theta' \sim \theta_0 f_0 U L_D/gH$ to obtain the nondimensionalized equations

[2] An alternative decomposition based on $\theta = \bar{\theta}(z,t) + \theta'(x,y,z,t)$, which is closer in spirit to the work of Solomon and Stone (2001), is given in appendix (4.6.1) for future reference.

[3] The definition of the deformation radius is different here from the QG system discussed in sections 3.6, 4.2 because H now refers to the full tropospheric height, and we have dropped the $\sqrt{2}$.

$$\epsilon \frac{D\mathbf{u}}{Dt} + \widetilde{\mu_u}\nabla^2\nabla^2\mathbf{u} + \mathbf{k}\times\mathbf{u} = -\nabla\phi' - \widetilde{R}\,\mathbf{u}, \tag{4.12}$$

$$\frac{D\theta'}{Dt} + w + \widetilde{\mu_\theta}\nabla^2\nabla^2\theta' = (1-r)w + \epsilon(1-r)\theta'_z - \widetilde{\alpha}\,(\theta' - \theta'_r), \tag{4.13}$$

$$u_x + v_y + \epsilon w_z = 0, \tag{4.14}$$

$$\theta' = \phi'_z, \tag{4.15}$$

$$\frac{D}{Dt} = \partial_t + u\partial_x + v\partial_y + \epsilon w\partial_z, \tag{4.16}$$

$$\theta'_r = -\frac{\widetilde{L_y}}{2\pi}\cos\left(\frac{2\pi}{\widetilde{L_y}}y\right), \tag{4.17}$$

with nondimensional numbers $\epsilon = \frac{U}{f_0 L_D} = \frac{U}{NH}$, $\widetilde{R} = \frac{1}{f_0}R$, $\widetilde{\alpha} = \frac{L_D}{U}\alpha$, $\widetilde{L_y} = \frac{1}{L_D}L_y$, $\widetilde{\mu_u} = \frac{1}{f_0 L_D^4}\mu_u$,$\widetilde{\mu_\theta} = \frac{1}{UL_D^3}\mu_\theta$.[4] The equations are solved using a spectral solver with adaptive time stepping (Burns et al. 2020) on a doubly periodic square domain of side $\widetilde{L_y} = 6\pi$, with vertical plates at $z = 0$ and $z = 1$ and $128 \times 128 \times 10$ grid points. Chebyshev polynomials are used as basis functions in the vertical (the grid spacing is uniform in the interior but slightly smaller towards the boundaries). The simulations are initialized with random conditions for all fields, after filtering out all wavenumbers with $k = \sqrt{k_x^2 + k_y^2} > 3$ to avoid having to integrate a lot of small scale noise in the initial phase of the simulation. The relaxation coefficient is fixed at $\alpha = 0.2$, and the diffusion coefficients at $\mu_u = \mu_\theta = 5 \times 10^{-5}$. In the following simulations, we explore a high Rossby number regime with $\epsilon = 0.4$ and a low Rossby number regime with $\epsilon = 0.01$ while keeping the latent heating strong at $r = 0.01$. For the high Rossby number runs we choose the drag to be $R = 0.11$ and for the low Rossby number runs we choose $R = 0.0018$. The drag needs to be smaller in the low Rossby regime so that the ratio of $t \sim \epsilon/R$ remains approximately constant, and the QG limit is properly

[4]We will see from the numerical simulations that scaling the length scales like the deformation radius remains a reasonable choice for the size of the potential vorticity anomalies even in the presence of strong latent heating. This can be intuited theoretically by remembering from DRV theory that while the ascent length vanishes as $r \to 0$ for the DRV modes, the DRV PV anomaly in the descent area is sustained by a balance of growth and zonal advection leading to an exponential decay length L_D/σ (section 2.3.3). But since the growth rate $\sigma = 1.62$ remains finite in the limit of $r \to 0$, the size of the PV disturbance also remains finite in this limit, at roughly $0.62L_D$ which is close to L_D.

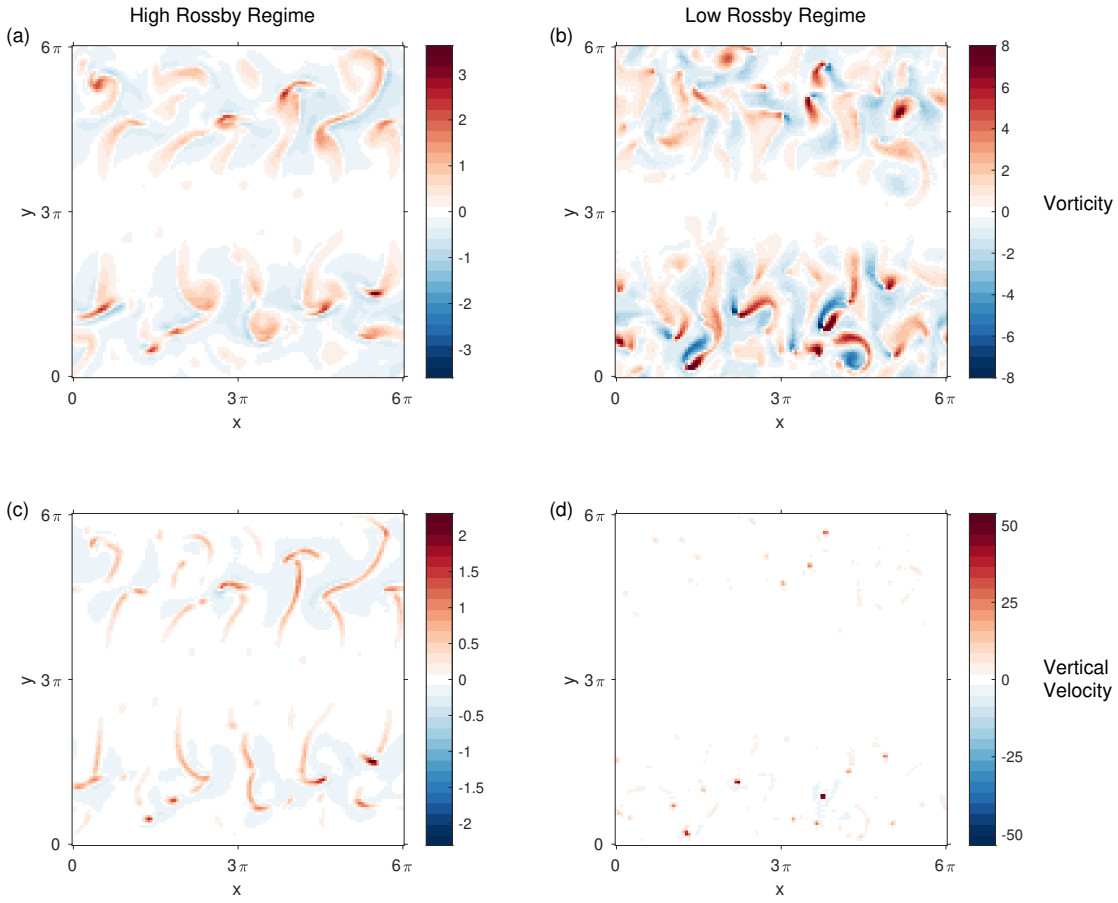

Figure 4-4: Snapshots of the relative vorticity and vertical velocity at midlevel for (a,c) a high Rossby number ($\epsilon = 0.4$), and (b,d) a low Rossby number ($\epsilon = 0.01$) run in the moist primitive equation simulations at $r = 0.01$. As the Rossby number is lowered, the wave-like pattern of the flow gets disrupted by vorticity dipoles which propagate poleward and are associated with isolated vertical velocity maxima.

recovered as ϵ tends to zero.

4.3.2 Simulation Results

Fig. 4-4 shows snapshots of the relative vorticity and vertical velocity at midlevel ($z = 0.5$) in the macroturbulent phase of the simulations for the high and low Rossby number regime. The reference potential temperature in both simulations is at a maximum at $y = 3\pi$ and minimum at $y = 0$ and $y = 6\pi$. This gives rise to two baroclinic zones centered on $y = 1.5\pi$ and $y = 4.5\pi$, that are associated with an easterly and a westerly jet respectively. The jets are unstable due to the condition

that vertical shear and meridional PV gradients are of the same sign at the lower boundary. As a result vortices form within the two baroclinic zones.

In the high Rossby number regime (Fig. 4-4 a and c), the flow is organized along the baroclinic zones taking on a wave-like pattern both in terms of vorticity and vertical velocity. The vertical velocity field is made up of large scale frontal bands, interspersed with isolated maxima, that resembles the midlatitude vertical velocity field. The vertically averaged asymmetry parameter is $\lambda = 0.75$ which is similar to what was found in the reduced stability simulations of O'Gorman et al. (2018) at $r = 0.01$. The flow does not show signs of transition to a vortex dominated regime despite the fact that latent heating is strong.

In the low Rossby number regime on the other hand (Fig. 4-4 b,d), the character of the flow changes dramatically. The vorticity fields loses its wave-like structure and becomes disrupted by vorticity dipoles, associated with strong isolated vertical velocity maxima, which continuously spawn and propagate poleward (towards $y = 0$, and $y = 6\pi$). Similarly, the vertical velocity field breaks up into isolated vertical velocity maxima, associated with the vorticity dipoles, and is characterized by a large asymmetry $\lambda = 0.88$. The simulations show clear signs of transition to a vortex dominated regime similar to the strong latent heating regime of the moist QG simulations.

Next we turn to the PV structure of the storms for the high and low Rossby number simulations. We calculate the Ertel PV

$$Q = [1 + \epsilon(v_x - u_y)]\theta_z - \epsilon^2 v_z \theta_x + \epsilon^2 u_z \theta_y, \tag{4.18}$$

with $\theta_z = 1 + \theta'_z$, and subtract the zonal mean to define the PV anomalies. We also calculate the PV tendency from latent heating

$$Q_t = \epsilon(1 + \epsilon\zeta)\dot{\theta}_z, \tag{4.19}$$

where $\zeta = v_x - u_y$ and $\dot{\theta} = [(1 - r(w))w\theta_z]$, and we have ignored contributions due

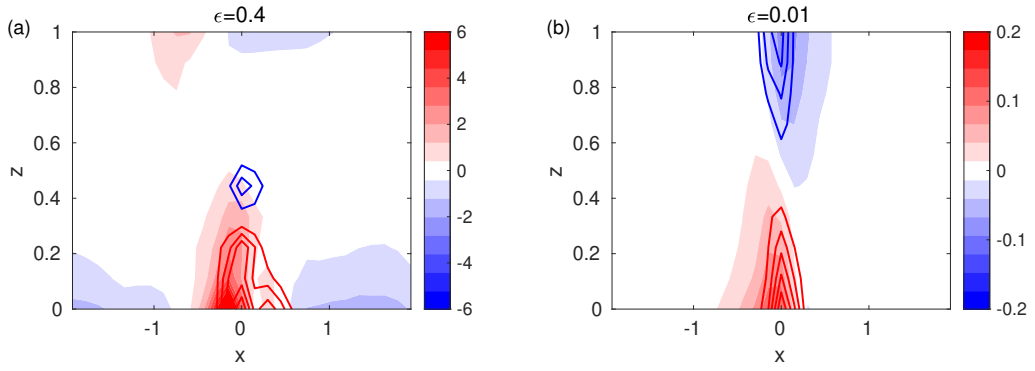

Figure 4-5: Storm composite of Ertel PV anomaly (shading) and PV tendency from latent heating (contours) (a) the high Rossby number simulations and (b) the low Rossby number simulations. The contour interval is (a) 2.30, and (b) 0.14. The zero contour line for the PV tendencies is not shown. Composites were made over the 10 strongest vertical velocity maxima for each simulation output between $t = 28 - 63$.

to horizontal gradients of the heating profile. The nondimensional form of the PV and PV tendency from latent heating are derived in the appendix (4.6.2). We then composite PV anomalies and PV tendencies over the 10 strongest vertical velocity maxima between $y = 3\pi - 6\pi$ at each simulation output between $t = 29 - 64$ (for a total of 25 outputs). The results are shown in Figure 4-5 for the high and low Rossby number runs.

While the low Rossby number storms show a clear dipole structure both in terms of PV anomaly and PV tendency, the high Rossby number storms are made up of a strong low level positive PV anomaly only. No strong negative PV anomaly is visible at the location of negative diabatic PV generation, although a weaker positive and negative PV anomaly signal is visible at the top boundary. Negative diabatic generation is weaker compared to positive diabatic generation. If vertical PV advection is added to the diabatic PV generation, the negative generation in the high Rossby number storms is entirely cancelled, while a clear negative generation persists for the low Rossby number storms (not shown). While diabatic generation extends throughout the entire model domain in the low Rossby number runs, it remains confined to the lower part of the domain at high Rossby number. Interestingly, the PV structure of the low Rossby number storms resembles that of the DRV mode from theory, and the DRV mode and storm from warm climate simulations (Figs. 2-3,

2-7)[5], while the PV structure of the high Rossby number storms resemble that of DRVs from reanalysis in the current climate (Fig. 2-10). The Rossby number is low for small-amplitude modes, and high for storms in reanalysis and hence a similarity between low Rossby numbers storms and DRV modes in warm climate simulations, and between high Rossby number storms and DRV storms in reanalysis is expected. The similarity between the low Rossby number storm and the DRV storm in warm climate simulations has less to do with the Rossby number[6], and more to do with the vertical profile of heating being less bottom heavy in the small-Rossby number runs (as discussed further in section 4.4).

4.3.3 Discussion

The simulations give a clear indication that changes in the Rossby number bring about important changes both in terms of the PV structure of individual storms and in terms of the overall state of the moist macroturbulent simulation. In particular, low Rossby numbers appear to make the simulations more like DRV world in which diabatically maintained PV dipoles continuously spawn and propagate meridionally disrupting the zonal confinement of the flow.

The Rossby number in these simulations also has an effect on the mean stratification, which becomes strongly bottom intensified at higher Rossby number. This raises the question of whether the different dynamical behavior comes about directly through higher-order terms in the PV dynamics becoming more important, or indirectly through changes in the mean state. In a second set of experiments, we tested this hypothesis by relaxing the zonal mean of the thermodynamic equation at 20α, while keeping the relaxation at α for the non-zonal mean thermodynamic equation. Bottom intensification of the mean stratification was prevented, but we found that

[5]For the warm climate DRV storm, the negative PV anomaly is stronger than the low level positive PV anomaly and concentrated at the tropopause (unlike in Fig. 4-5b). However, this asymmetry is likely due to the fact that the background static stability, and hence the background PV profile, increases strongly towards the tropopause in the real atmosphere, whereas the reference stratification in our simulations is taken to be constant. This modifies the PV structure due to the possibility of advection of mean vertical PV gradients. For further discussion see section (4.4).

[6]The Rossby number is much larger for the DRV storm than the DRV mode in the ideaelized GCM.

the transition to a vortex dominated flow still persists at low Rossby numbers (not shown). We therefore conclude that higher order terms in the PV dynamics are the main cause behind the different behavior of the two simulations.

4.4 Vertical Structure of PV in Finite Amplitude DRVs

We study a 1-D toy model for the vertical structure of PV in the ascent region of a DRV in order to understand why the PV structure is different at high versus low Rossby number. This will help to bridge the gap between the theory of DRV modes and storms, although we emphasize that it is not a full model because the ascent profile w will be taken as given. The model is inspired by the work of Schubert and Alworth (1987) on the PV evolution within tropical cyclones and consists of the thermodynamic equation with reduced stability parametrization of latent heating and the PV equation

$$\theta'_t + w\bar{\theta}_z + \epsilon r w\theta'_z = \dot{\theta}, \tag{4.20}$$

$$Q_t = \epsilon\frac{Q\dot{\theta}_z}{\bar{\theta}_z + \epsilon\theta_z} - \epsilon w Q_z, \tag{4.21}$$

where $\bar{\theta}_z$ represents a background stratification that is assumed constant in time, $\dot{\theta} = (1-r)w\bar{\theta}_z + \epsilon(1-r)w\theta'_z$ is the heating rate, and we focus on a single vertical column in a region of maximum heating $\dot{\theta}_x = \dot{\theta}_y = 0$, approximate the PV as $Q = (1+\epsilon\zeta)\theta_z$, which ignores the terms $\epsilon^2 v_z\theta_x$ and $\epsilon^2 u_z\theta_y$, and ignore any horizontal PV transport. A derivation is given in the appendix (4.6.2). The toy model is solved in time choosing a constant Rossby number of $\epsilon = 0.4$ for the storms and $\epsilon = 0.01$ for the modes. The integration is started from the initial conditions $\theta = 0$ and $Q = \bar{\theta}_z$, where we consider separately the case of a constant background stratification $\bar{\theta}_z = 1$ and an exponential stratification $\bar{\theta}_z = 1 + 9e^{\frac{(z-1)}{0.1}}$ which is close to one at

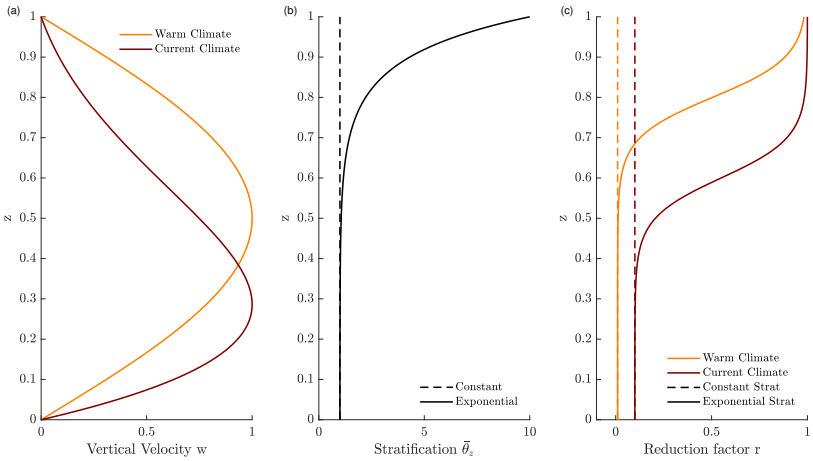

Figure 4-6: Vertical profiles of (a) the vertical velocity w, (b) the background stratification $\bar{\theta}_z$ and (c) the reduction factor r used for integration of the toy model. The bottom heavy vertical velocity profile is representative of storms in the current climate, and the symmetric vertical velocity profile is representative of storms in the warm climate. In the case of a constant background stratification, a constant reduction factor is chosen with values of $r = 0.1$ for the current climate and $r = 0.01$ for the warm climate (global mean surface air temperature of 311K). In the case of an exponential stratification, r is the same as for a constant stratification at lower levels, but is allowed to transition smoothly towards $r = 1$ at $z_T = 0.6$ in the current climate and $z_T = 0.8$ in the warm climate.

the surface ($z = 0$) and is equal to 10 at the tropopause ($z = 1$). The constant stratification case is chosen to represent the set-up considered in the small-amplitude DRV theory in section (2.3), and the moist primitive equation simulations in section (4.3). The exponential stratification case is chosen to allow for closer comparison to the idealized GCM simulations of O'Gorman et al. (2018), and the DRV storms in reanalysis where the stratification increases strongly towards the tropopause leading to an important role for vertical advection of the mean PV profile. The vertical velocity profile is fixed in time, and we consider a symmetric profile $w = \sin(\pi z)$ and a bottom heavy profile $w = \sin(\pi z)e^{-(z-1)/0.4}$ that we normalize by its maximum value. The symmetric profile is meant to be representative of a warm climate (global mean surface temperature of 311K) and the bottom heavy profile representative of the current climate, as was found for the DRV storms in idealized simulations in a warm climate and in ERA5 that were discussed in section (2.5). The two profiles are shown in Fig. 4-6a.

For the calculations with a constant background stratification, a vertically constant profile is chosen for r with a value of $r = 0.01$ for the warm climate and $r = 0.1$ for the current climate. For the calculations with an exponential stratification, we let the reduction factor vary vertically $r(z) = r + 0.5(1 - r)(1 - \tanh[(z_T - z)/\delta z])$ such that r tends smoothly towards 1 over a vertical distance $\Delta z = 0.1$ as z_T is approached. For the warm climate we choose $z_T = 0.8$ and for the current climate we choose $z_T = 0.6$ to represent the fact that the moist static stability is closer to moist neutral over a larger vertical extent in a warm climate. The different vertical profiles of stratification and reduction factor are shown in Fig. 4-6b,c. It is necessary to choose a more realistic vertically varying reduction factor in the case of a more realistic exponential stratification because the definition of r (Eq. 3.6) involves a normalization by θ_z (otherwise the latent heating would maximize near the tropopause). With the r profile chosen, even though the stratification increases towards the tropopause, $r \to 1$ such that the heating rate remains small.

The equations are solved in time until $t = 0.6$, which corresponds roughly to $t = 0.6L_D/U = 17$h using typical scales $L_D = 1000$km and $U = 10$m/s. The resulting PV anomaly profiles are shown in Fig. 4-7 where we have defined PV anomalies with respect to the initial PV profile. We focus first on the case of a constant background stratification (Fig. 4.20a-c). The warm climate mode forms the typical PV dipole structure of the small amplitude DRV theory (Fig. 4-7a). It is antisymmetric about the altitude of maximum ascent $z = 0.5$. In contrast to that, the PV anomalies for the warm climate storm have stronger positive than negative PV anomaly (Fig. 4-7b). This is because of the nonlinear feedback between the PV and the heating gradient in the first term on the right-hand side of Eq. (4.21) which amplifies the generation of positive PV anomalies but weakens the generation of negative PV anomaly. For the mode, this feedback is negligible because the PV anomalies are too weak, but for the storm it is important because the magnitude of the PV anomalies is larger. We also note that vertical advection has begun to move the positive PV anomaly upwards so that the change from positive to negative PV anomaly no longer occurs at about $z = 0.5$ but instead at $z = 0.6$. If the integration is continued, the positive

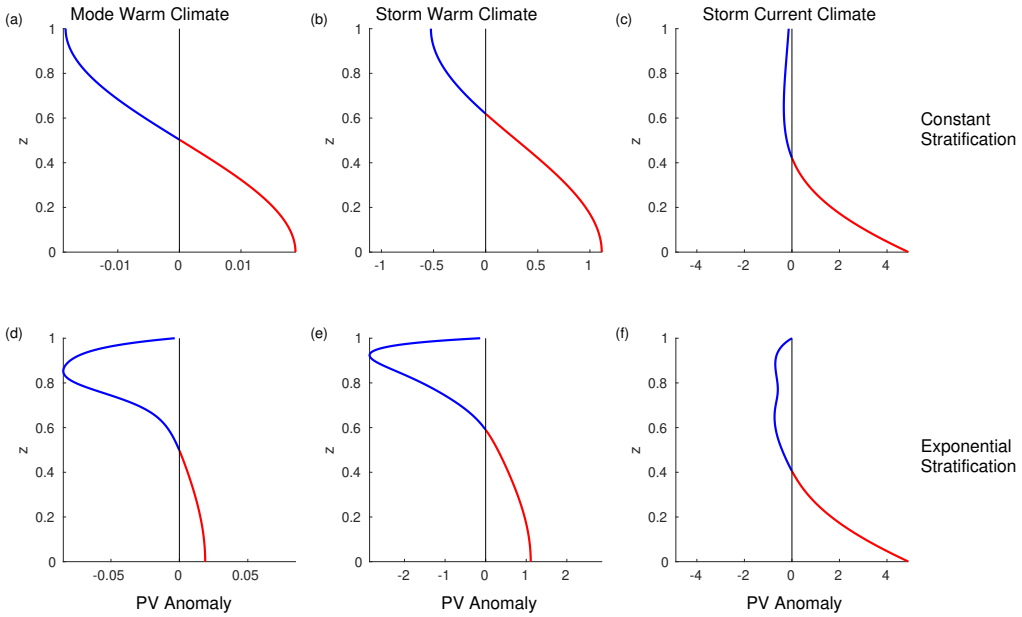

Figure 4-7: PV anomaly profiles produced by integrating the toy-model Eqs. (4.20-4.21) for (a,b,c) a constant background stratification, and (d,e,f) an exponential stratification until $t = 0.6$. For the warm climate, $r = 0.01$ and the symmetric w-profile shown in Fig. 4-6 were chosen. For the current climate, $r = 0.1$ and the bottom heavy profile from Fig. 4-6 were chosen. A Rossby number of $\epsilon = 0.4$ is chosen for the storms and $\epsilon = 0.01$ for the modes. The PV anomalies are defined with respect to the initial conditions corresponding to a constant PV profile for a,b,c and an exponential PV profile for d,e,f.

PV anomaly would keep being advected vertically and gradually begin to fill up the entire vertical column until no negative PV anomaly is left (not shown). This limit is spurious however, since the assumption of a sustained vertical velocity profile would break down. Looking at the storm in the current climate (Fig. 4-7c), we notice that the positive PV anomaly has grown even larger than for the storm in the warm climate. The PV structure is highly asymmetric in magnitude between positive and negative PV anomalies with the surface PV anomaly about 14 times stronger than the negative PV anomaly aloft. This is because the bottom heavy vertical velocity profile implies a bottom heavy heating rate. The vertical gradient of the heating rate, tied to PV generation, will be larger below the heating maximum, leading to stronger positive generation, and weaker above the heating maximum, leading to weaker negative PV generation. This signal then gets amplified by the nonlinear feedback between PV and the heating gradient. We note that due to the nonlinearity of this feedback, the strength of the low level PV anomaly that is reached at the end of the integration is very sensitive to the magnitude of the Rossby number, the bottom-heaviness of the heating rate and the time over which the heating acts (here given by the integration time). For the current climate storm for instance, doubling of the Rossby number to $\epsilon = 0.8$ leads to a surface PV anomaly that is about 8 times larger (not shown). This sensitive dependence of the PV asymmetry on the Rossby number and the bottom-heaviness of the heating profile explains very well the differences found between the PV structure of the winter and summer DRV example discussed in section (2.5). In that case, the winter storm was found to be more asymmetric in terms of the magnitude of positive versus negative PV anomalies (no clear negative PV identifiable) because it was a stronger storm, implying a higher Rossby number, and it had a more bottom heavy heating profile.

We now turn to the calculations with an exponential background stratification (Fig. 4-7d-f). Looking at the warm climate mode (Fig. 4-7a), we note that the negative PV anomaly is now stronger than the positive PV anomaly even in the low Rossby number case. This is because of vertical advection of mean PV which is zero in the case of a constant background stratification but nonzero in the case of

an exponential stratification. Low PV air is advected vertically into a region that had strong PV initially, and hence a strong negative anomaly is produced. In the small-amplitude moist QG theory of Kohl and O'Gorman (2022), vertical advection of mean PV is not included and hence positive and negative PV anomalies are of the same magnitude. Looking at the structure of the warm climate DRV storm (Fig. 4-7e), we notice that unlike in the constant stratification case positive PV anomalies are now weaker than negative PV anomalies. Again the reason is vertical advection of mean PV which concentrates a strong negative PV anomaly at the tropopause, similar to what has been found for the DRV storm in the warm climate simulations of O'Gorman et al. (2018). This highlights the importance of taking into account the reference state in the definition of the PV anomalies when making comparisons of the PV structure. If we integrate further in time, the positive PV anomaly in the warm climate storm will eventually outgrow the negative PV anomaly again (not shown). Looking at the storm in the current climate, we notice that the presence of an exponential stratification has not altered the PV structure significantly. We still find a strong positive low level PV anomaly with weak upper level negative anomaly. This is because bottom heaviness of the vertical velocity profile, and shallower depth z_T of the reduction factor leave the upper levels quasi undisturbed. Increasing z_T, it is possible to produce slightly stronger negative PV anomalies at the tropopause but these anomalies remain small compared to the surface anomaly for the parameters explored (not shown).

4.5 Conclusions

Finite amplitude effects for DRVs were explored in simulations of moist macroturbulence using the QG and primitive equations and an attempt at synthesis in the form of a toy model of the vertical structure of PV was made.

Moist QG simulations with a reduced stability parametrization transition from a state of wavy jets interspersed with vortices to a vortex dominated state as latent heating is increased. PV budget analysis revealed that the vortices in the strong

latent heating regime were DRVs with diabatic generation dominating over meridional PV advection. The solutions were maintained by a balance between mean zonal advection, nonlinear advection and diabatic generation. This is very similar to the balances maintaining the DRV mode from theory, with the additional effect of nonlinear advection which now leads to poleward self advection. Simulations of the moist primitive equations in a simple doubly periodic configuration without beta effect were run for high and low Rossby number regimes while keeping latent heating strong. The simulations provided evidence that changes in the Rossby number brought about important changes both in terms of the state of the macroturbulence simulations and the PV structure of strong diabatic storms. At low Rossby number the zonal flow became disrupted by isolated vorticity dipoles which continously spawned and self-advected poleward. The vertical velocity field broke up into isolated maxima with a strong asymmetry between upward and downward motion. At high Rossby number the flow maintained a wave-like structure and a transition to vortex world was not found. While the PV structure of strong diabatic storms in the low Rossby number simulations resembled that of DRV modes and DRV storms from warm climate simulations, the PV structure of storms in the high Rossby number simulations was more asymmetric and bottom confined and resembled that of DRVs from the current climate. We concluded that higher order terms in the PV dynamics beyond QG might play an important role in preventing transition to DRV world.

Finite amplitude effects beyond the small-amplitude QG DRV theory were explored within a simple toy model of the moist thermodynamic and PV equations. The toy model was solved for a low and high Rossby number, to transition from a modal solution to a storm, and for a bottom heavy and symmetric vertical velocity profile, to transition between a current and a warm climate . The toy model was able to reproduce much of the variety that has been observed in terms of the PV structure of DRV modes and DRV storms in current and warm climates. In particular, it was found that a high Rossby number coupled with bottom heavy heating profiles can lead to rapid generation of strong low level PV anomalies with much smaller upper level negative anomaly - as is often found for DRVs in the current climate.

Strong sensitivity of the asymmetry of the magnitude of negative versus positive PV anomalies was found to the degree of bottom heaviness of the heating rate and the magnitude of the Rossby number. In particular, symmetric vertical velocity profiles, more characteristic of a warm climate, produced stronger upper level negative PV anomaly compared to bottom heavy vertical velocity profiles when vertical advection of mean PV was important because of an exponential background stratification. The resulting solutions showed close resemblance to warm climate DRV storms in the idealized GCM simulations.

Given that strong negative PV anomaly is required for diabatic growth and poleward self-advection, the results lead us to the following speculation. In the current climate, where heating rates are more bottom heavy, diabatic generation leads to the rapid genesis of low level positive PV anomalies. The negative PV anomaly is quickly eroded away capping growth and poleward self advection. Meanwhile the diabatically generated positive PV anomaly has become sufficiently large in amplitude to be able to undergo nonlinear interaction with upper level PV anomalies in a later secondary growth process (Wernli et al. 2002). In the warm climate, where the vertical velocity profile is more symmetric between the upper and lower troposphere, diabatic generation leads to the generation of PV with more of a dipole structure. Negative anomalies are also stronger due to vertical advection of the mean PV profile towards the tropopause. The sustained presence of a negative anomaly leads to continous growth and poleward self-advection over a longer period of time allowing the DRV solutions to be more disruptive to the midlatitude flow, and facilitating a transition to DRV world.

The Rossby number in our simulations is given by $\epsilon = U/f_0 L_D = U/NH$. Hence, smaller Rossby numbers could be achieved by weaker shear or stronger static stability both of which are key parameters of interest in a warming midlatitude climate. Future work could investigate the transition to DRV world in GCMs, e.g. by varying the strength of the midlatitude jet, to confirm whether the dependence of DRV world transition on the Rossby number holds in models with a more realistic representation of moist physics and to characterize the state of the midlatitude circulation once DRV

world has been reached.

4.6 Appendix

4.6.1 Rewriting the θ Equation in an Alternative Form

We rewrite the full dimensional θ equation (Eq. 4.2) by splitting $\theta = \bar{\theta}(z,t) + \theta'(x,y,z,t)$ and $\theta_r = \bar{\theta}_r(z) + \theta'_r(y)$, where $\overline{(...)}$ refers to a horizontal average, to give

$$\frac{D\theta'}{Dt} + \partial_t\bar{\theta} + w\bar{\theta}_z = (1-r)w\bar{\theta}_z + (1-r)w\theta'_z - \alpha(\bar{\theta}-\bar{\theta}_r) - \alpha(\theta'-\theta'_r), \tag{4.22}$$

where $\bar{\theta}_r(z) = \frac{z\theta_0 N^2}{g}$ and $\theta'_r(y) = -\frac{f\theta_0 U}{gH}\frac{L_y}{2\pi}\cos(\frac{2\pi y}{L_y})$, and we have neglected the hyperdiffusion terms. Next we nondimensionalize the mean temperature like $\bar{\theta}, \bar{\theta}_r \sim \frac{H\theta_0 N^2}{g}$ and perturbations like $\theta', \theta'_r \sim \frac{\theta_0 f U L_D}{gH}$ to obtain the nondimensionalized equation

$$\frac{D\theta'}{Dt} + \frac{1}{\epsilon}\partial_t\bar{\theta} + w\bar{\theta}_z = (1-r)w\bar{\theta}_z + \epsilon(1-r)w\theta'_z - \frac{\widetilde{\alpha}}{\epsilon}(\bar{\theta}-\bar{\theta}_r) - \widetilde{\alpha}(\theta'-\theta'_r), \tag{4.23}$$

where $\bar{\theta}_r(z) = z$ and $\theta'_r(y) = -\frac{\widetilde{L_y}}{2\pi}\cos(\frac{2\pi y}{\widetilde{L_y}})$. Now taking the horizontal average of this equation we obtain

$$\frac{1}{\epsilon}\partial_t\bar{\theta} + \bar{w}\bar{\theta}_z = -(\overline{u'\theta'_x} + \overline{v'\theta'_y} + \epsilon\overline{w'\theta'_z}) + \bar{\dot{\theta}} - \frac{\widetilde{\alpha}}{\epsilon}(\bar{\theta}-\bar{\theta}_r), \tag{4.24}$$

where $\dot{\theta} = (1-r)w\bar{\theta}_z + \epsilon(1-r)w\theta'_z$. Using the fact that the flow is nondivergent so that the horizontal transport vanishes we obtain

$$\frac{1}{\epsilon}\partial_t\bar{\theta} = -\epsilon\left(\overline{w'\theta'}\right)_z + \bar{\dot{\theta}} - \frac{\widetilde{\alpha}}{\epsilon}(\bar{\theta}-\bar{\theta}_r), \tag{4.25}$$

for the mean state equation. Subtracting this equation from the full equation we obtain

$$\frac{D\theta'}{Dt} + w\bar{\theta}_z = \epsilon\left(\overline{w'\theta'}\right)_z + \dot{\theta} - \bar{\dot{\theta}} - \widetilde{\alpha}(\theta' - \theta'_r), \tag{4.26}$$

for the perturbation equation. This decomposition is more similar in spirit to that of Solomon and Stone (2001) and is kept here for future reference.)

4.6.2 Nondimensional form of the PV equation

Eqs. (4.2-4.5) can be combined into an equation for the PV Q (Vallis 2017, his Eq. 4.96)

$$\frac{DQ}{Dt} = (f+\zeta)\dot{\theta}_z - v_z\dot{\theta}_x + u_z\dot{\theta}_y, \tag{4.27}$$

where

$$Q = (f+\zeta)\theta_z - v_z\theta_x + u_z\theta_y, \tag{4.28}$$

$$\dot{\theta} = (1-r)w\theta_z, \tag{4.29}$$

$$\theta_z = \bar{\theta}_z + \theta'_z, \tag{4.30}$$

$$\frac{D}{Dt} = \partial_t + u\partial_x + v\partial_y + w\partial_z \tag{4.31}$$

and we have ignored the drag, relaxation and hyperdiffusion terms in Eq. (4.27). Nondimensionalizing θ_z, $\bar{\theta}_z \sim \theta_0 N^2/g$, the PV like $Q \sim f_0\bar{\theta}_z = f\theta_0 N^2/g$ and the rest of the variables with scales as outlined in section (4.3), we obtain the nondimensional PV equation

$$\frac{DQ}{Dt} = \epsilon(1+\epsilon\zeta)\dot{\theta}_z - \epsilon^2 v_z\dot{\theta}_x + \epsilon^2 u_z\dot{\theta}_y, \tag{4.32}$$

where

$$Q = (1 + \epsilon\zeta)\theta_z - \epsilon^2 v_z \theta_x + \epsilon^2 u_z \theta_y, \tag{4.33}$$

$$\dot{\theta} = (1 - r) w \theta_z, \tag{4.34}$$

$$\theta_z = \bar{\theta}_z + \epsilon\theta'_z, \tag{4.35}$$

$$\frac{D}{Dt} = \partial_t + u\partial_x + v\partial_y + \epsilon w \partial_z \tag{4.36}$$

and all variables are now nondimensional. The first term on the rhs of Eq. (4.32) corresponds to Eq. (4.19) in the text if we let $\bar{\theta}_z = 1$ (i.e. a constant stratification).

If we place ourselves at the location of the heating maximum $\dot{\theta}_x = \dot{\theta}_y = 0$, neglect all horizontal transport of PV, and neglect the higher order vertical shear terms in the PV (Eq. 4.33), we obtain

$$\partial_t Q + \epsilon w Q_z = \epsilon(1 + \epsilon\zeta)\dot{\theta}_z \tag{4.37}$$

$$Q = (1 + \epsilon\zeta)\theta_z \tag{4.38}$$

which we can rewrite as

$$\partial_t Q = \epsilon \frac{Q\dot{\theta}_z}{\bar{\theta}_z + \epsilon\theta'_z} - \epsilon w Q_z \tag{4.39}$$

which is the form of the PV equation (Eq. 4.21) used in the simple 1D toy-model in section (4.4.

Chapter 5

Conclusion and Future Directions

Water and its change of phase have profound effects on the dynamics of the midlatitude atmosphere challenging us to extend our theoretical understanding of baroclinic instability and macroturbulence beyond dry-adiabatic theory. Two specific phenomena in which latent heating plays a key role and that have challenged our theoretical understanding formed the central focus of this thesis: 1.) the asymmetry of the distribution of the vertical velocity field, which has important implications for the distribution of precipitation and its extremes 2.) Diabatic Rossby Vortices, which are a special class of midlatitude storm that derives its energy from latent heating rather than baroclinic effects and as such goes beyond the traditional understanding of midlatitude storm formation.

In the following we will review key contributions made in this thesis and discuss future directions of research.

5.1 Key Contributions

5.1.1 A Theory for the Asymmetry of the Vertical Velocity Distribution in Moist Macroturbulence

Previous work showed that changes in the asymmetry with climate warming is much smaller in moist macroturbulent simulations than what is predicted from the theory

of moist baroclinic modes. This distinction is significant since the atmosphere is constantly in a state of moist macroturbulence, but scalings for moist baroclinic modes have formed the basis for understanding skewness changes with warming in the literature (Pendergrass and Gerber 2016). This made the development of a theory for the asymmetry reached in the macroturbulent regime desirable.

In chapter 3, we applied inversions of a moist-QG omega equation to the GCM output of O'Gorman et al. 2018 in both the modal and macroturbulent regime and diagnosed the contributions to the asymmetry coming from the dynamical forcing versus the contributions coming from the moist static stability. We showed that while both the dynamical forcing and reductions in the moist static stability contributed to the asymmetry for the moist baroclinic modes, reductions in moist static stability were the main contributor to the asymmetry in the macroturbulent regime. The dynamical forcing was shown to be practically unskewed. An important dynamical difference between modal and macroturbulent state was hereby identified. Using 2-layer moist QG theory to explain asymmetry changes, we showed that the strong asymmetry contributions from the dynamical forcing in the modal regime were due to a feedback between the vertical velocity and the dynamical forcing which does not exist in the macroturbulent regime due to advective nonlinearties. Furthermore, we distilled the insights from the three-dimensional inversions into a toy-model of the moist omega equation that was solved for a given reduction factor and wavenumber of an unskewed dynamical forcing to reproduce the slow increase of the asymmetry with warming both in the idealized GCM simulations and from winter to summer in reanalysis. Finally, we showed using simulations of moist QG turbulence that, consistent with the toy-model prediction, high asymmetry states are still possible despite unskewed dynamical forcing so long as the wavenumber of the dynamical forcing is sufficiently large. Unlike the classic states of dry beta plane turbulence with wavy-jets interspersed with vortices, the high asymmetry states in the strong latent heating regime of the simulations corresponded to 'DRV world' - a macroturbulent flow dominated entirely by DRVs.

5.1.2 Small and Finite Amplitude Theories for Diabatic Rossby Vortices

Past research has identified a special class of midlatitude storm, dubbed the Diabatic Rossby Vortex (DRV), which derives its energy from the release of latent heat associated with condensation of water vapor, and as such goes beyond the traditional understanding of midlatitude storm formation. While we have a good theoretical understanding of classic cyclogenesis, both in terms of simple conceptual models of baroclinic instability and potential vorticity (PV) dynamics of finite-amplitude storms, our understanding of DRV formation and propagation, the controls on their growth rates and length scales and their response under climate change is poor. This makes the development of an equivalent theoretical understanding for DRVs desirable.

In chapter 2, we developed a simple moist 2-layer QG model with tilted boundaries and showed that it was capable of producing an isolated DRV mode. PV budget analysis revealed that the DRV mode is maintained by zonal advection in the downdrafts, and by a combination of zonal advection and latent heating in the updrafts. Having isolated the DRV mode within a simple model, we derived the dispersion relation for the growth rate and ascent length scale of the disturbance analytically retaining the full complexity of nonlinear heating - a major novelty of this work. In the limit of a convectively neutral stratification, asymptotic expressions for the growth rate and ascent length were found. In this limit, the DRV was shown to grow faster than the dry baroclinic wave and faster than the moist baroclinic wave consistent with its emergence as the most unstable mode with warming in idealized GCM calculations. The ascent length scaled the same between DRV and moist baroclinic waves. We then solved the dispersion relation numerically for the entire range of r values and showed mathematically that isolated solutions on an infinite domain cease to exist above values of $r > 0.4$. Reintroducing meridional PV gradients into the two-layer model and varying the strength of latent heating and meridional PV gradients, we created a phase diagram for when the most unstable mode was a DRV vs. a moist-baroclinic wave. DRVs were shown to emerge when both the PV gradients and latent heating

were sufficiently weak, and an explanation for the wave-vortex transition was given in terms of a simple PV argument. Finally, we compared the structure of DRV modes to DRV storms at finite amplitude and showed, using a generalized diabatic tendency that includes the effects of diabatic vertical and ageostrophic horizontal advection, that finite amplitude effects must be taken into account to relate the structure of PV anomalies and PV generation in observed storms.

In chapter 4, we went beyond DRV modes and studied the role of finite amplitude effects in the dynamics of individual DRV storms and the transition to DRV world in simulations of moist macroturbulence using the moist QG and primitive equations. We began by exploring the vortex world of the strong latent heating regime of the moist QG simulations. Using PV budget analysis we showed that the vortices in this regime were maintained by a balance between mean horizontal advection, nonlinear advection, and diabatic generation from latent heating, with meridional PV advection playing a negligible role. The PV budget showed strong similarity to that of the DRV mode from theory with the additional effect of nonlinear terms now leading to a poleward self-advection of the disturbances. In order to better understand the role of finite amplitude effects beyond QG, moist primitive equation simulations were run at a high Rossby number regime and a low Rossby number regime while keeping latent heating strong. As the Rossby number was lowered, a drastic change was observed both in terms of the dynamics of individual storms and in terms of the character of the overall macroturbulent circulation. The wave-like pattern of midlatitude flow observed in the high Rossby number runs started to become disrupted by vorticity dipoles that continously spawned and propagated polewards through self-advection. Similarly, the vertical velocity field broke up into strong isolated maxima and showed elevated skewness. While storms in the high Rossby number regime were dominated by low-level positive PV anomaly with weak upper-level negative PV anomaly, reminescent of DRVs in the current climate, storms in the low Rossby number regime were characterized by dipoles in PV and diabatic PV generation that extended vertically throughout the whole domain, reminescent of DRVs in warm climate simulations. We ended this chapter by distilling finite amplitude effects into a simple 1d toy-model

that was solved using a high and low Rossby number, and a current and warm climate configuration to reproduce much of the observed variety of PV structure in DRVs in idealized simulations and reanalysis. The 1d model showed that the strength of the low level PV anomaly relative to the upper PV anomaly was very sensitive to the size of the Rossby number and the bottom-heaviness of the heating profile.

5.2 Future Directions

Moist midlatitude dynamics is a largely unsolved field of research which offers many fresh challenges of which only a few have been treated in this thesis. We would like to end by spelling out interesting future directions of research that are motivated by the findings in this thesis.

5.2.1 Towards a general theory of the vertical velocity asymmetry in moist macroturbulence

Our theory for the asymmetry of the vertical velocity distribution in moist macroturbulence is based on a toy-model. While the toy-model is good at highlighting some of the key controls on the asymmetry implied by the moist omega equation, it cannot amount to being fully exact or complete. It cannot be exact because it is based on a heavily truncated representation of the dynamical forcing in the form of a single sinusoid. It cannot be complete because it depends on knowledge of the wavenumber of the dynamical forcing which is not known a priori and must be inferred. Future work could improve on the exactness front by taking into account the full spectral slope of the dynamical forcing in the toy model inversions. Concerning completeness, better understanding is required for what sets the wavenumber of the dynamical forcing in moist macroturbulent flows. Although this is certainly a hard problem, this thesis suggests that there might be an important dependence on the Rossby number to exploit - high Rossby number flows had a larger wavenumber than small Rossby number flows. Based on our toy model, this leads to the unexplored consequence

that increasing the Rossby number decreases rather than increases the vertical velocity asymmetry in moist macroturbulence - a highly counterintuitive result from the point of view of dry theory!

5.2.2 Towards a general classification of moist disturbances

In this thesis, we have begun the work of classifying moist instabilities in a two-layer model retaining the full complexity of nonlinear heating and variable meridional PV gradients. In the spirit of earlier work (De Vries et al. 2010, Cohen and Boos 2016) which attempted a classification of moist disturbances in the Eady model albeit with linearized representation of latent heating, the next steps would be to extend the phase diagram for the two-layer model to include the full vertical structure of the heating profile, the meridional PV gradient profile, and the shear profile. Furthermore, it would also be interesting to include horizontal shear since moist barotropic instabilities have been found to be relevant for monsoon depressions (Diaz and Boos 2021). The ultimate goal would be to arrive at a general classification of moist disturbances including moist baroclinic waves, DRVs, monsoon depressions and polar lows in terms of shear, latent heating and meridional PV gradients.

5.2.3 Mean meridional PV gradients as an important metric to analyze in models and reanalysis

While DRVs have previously been understood as mostly latent heating driven phenomena, this work suggests that meridional PV gradients also have an important part to play in determining the conditions under which transition from moist baroclinic waves to DRV modes of instability occur. In fact, meridional PV gradients had to be only slightly weakened with respect to the classic two-layer Phillip's model set-up to transition to isolated DRV solutions. This suggests that meridional PV gradients would be an important metric to analyze, besides latent heating, when trying to understand the environments conducive to DRV formation in models and reanalysis. In the two-layer model, diabatic generation co-occured in regions of weakened meridional

PV gradients by construction. However, in an atmosphere continous in the vertical this does not have to be the case - e.g. meridional PV gradients could be weakened aloft under climate warming, without diabatic generation yet reaching high enough to co-occur. Based on this argument, analyzing and understanding changes in the vertical structure of the latent heating and meridional PV gradient field under warming would be very fruitful. Models would have to get the phasing between both fields right in order to capture the dynamics of moist disturbrance accurately - a difficult task.

5.2.4 Understanding the limitations of the reduced stability parametrization in moist macroturbulent simulations

Throughout this thesis we have worked within the reduced stability framework which assumes that all ascending motions are saturated. While this framework is marvelous because it allows us to boil down much of the complexity of latent heating processes into a single nonlinear parameter $r(w)$ and gain great theoretical insights, it has its limitations particularly when it is employed in simulations of moist macroturbulence since it presumes an infinite reservoir of moisture and neglects horizontal moisture advection. Simple moist two-layer QG systems with prognostic moisture variable exist (Lapeyre and Held 2004), and it would be useful to compare the two systems more closely, both when it comes to the growth of moist baroclinic modes and moist macroturbulent states. In the case of synoptic scale monsoonal disturbances, having a separation between the area of maximum ascent and the area of maximum precipitation has been found to be key in theoretical descriptions (A. Adames 2018, Adames 2021). Relaxing the assumption of co-occurence of maximum ascent and maximum precipitation might therefore be important in order to reason about moist disturbances across different latitudes.

5.2.5 Understanding the impact of finite amplitude effects on the growth rate of DRVs

One of the open mysteries is whether finite amplitude effects merely distort the PV structure of DRV modes or also affect their growth rate. At first glance, the simple 1d model for understanding PV structure in storms suggests that DRVs can grow both in high and low Rossby number environments - and that they might actually do so particularly fast at high Rossby number especially when the heating rate is bottom heavy, as is often the case in the current climate. This result raises the possibility that the reason the DRVs in the low Rossby number runs of the primitive equations are more 'disruptive' to the overall macroturbulent flow is not because they are growing, but rather because they have sufficient upper level negative PV anomaly to strongly propagate poleward through self-advection. However, the drawback with the 1d model is that it assumes a constant vertical velocity profile in time and it is unclear to what extent it can be used to reason about the effects of finite amplitude effects on the growth rates. Future work should therefore test the relation between finite amplitude effects and growth rates in DRVs either with a semigeostrophic model that has sufficient vertical levels to accurately resolve effects such as vertical PV advection, or by tracking DRVs across a range of climates in idealized GCM simulations.

5.2.6 Understanding the different frequency of DRVs in the Northern and Southern Hemisphere

DRVs occur more frequently in the Northern (10 systems per month) compared to the Southern Hemisphere (4 systems per month) and this difference is important to understand (Boettcher and Wernli 2013, Boettcher and Wernli 2015). The work in chapter 3 on asymmetries showed that the seasonal cycle of λ is more pronounced in the Northern compared to the Southern Hemisphere, and this difference is because the reduction factor r decreases more strongly in summer in the Northern Hemisphere. Small reduction factors favor DRVs, and this could be a possible explanation for the differences in DRV frequencies between the two hemispheres. Further work should

look into this hypothesis and take into account possible hemispheric differences in the structure of meridional PV gradients.

5.2.7 Simulating Diabatic Rossby Vortex Worlds in GCMs

The moist primitive equation simulations give a clear indication that changes in the Rossby number bring about important changes both in terms of the PV dynamics of individual storms and in terms of the state of the overall moist macroturbulent circulation. The Rossby number in these simulations is given by $\epsilon = U/fL_d = U/NH$, where U is the strength of the jet, f is the planetary vorticity, $L_d = NH/f$ is the deformation radius, N is the static stability and H is the height of the tropopause. In physical terms, lower Rossby number regimes could be achieved by weaker shear or stronger static stability - both of which are key parameters of interest in a warming midlatitude climate. It would be very interesting to simulate different Rossby number regimes in a moist GCM in order to see if the transition to DRV world persist in models with a more realistic representation of latent heating, and to characterize the state of the simulation in terms of its precipitation field and heat transport.[1]

5.2.8 Need for problem sets, review articles, and textbook chapters on theories of moist midlatitude dynamics

A significant obstacle to the further development of moist midlatitdue dynamics, besides the inherent complexity of the subject, lies in the lack of adequate textbook coverage of key theoretical developments in the field over the last thirty years that would allow students to have an accessible pedagogical introduction, as is the case for dry dynamics. The greatest recognition that research work can receive is if it is both published and taught. We hope this thesis inspires the reader to use some of its material and that on which it builds, particularly the great theoretical work from

[1]The moist primitive equation simulations had a nondimensional domain of length $L = 6\pi$ and $n = 128$ gridpoints. Choosing a typical scale of $L_D = 1000$km for the deformation radius, this gives us an estimate for the resolution of $\Delta x = L/n \times L_D = 6\pi/128 \times 1000\text{km} = 147\text{km}$ that is at least necessary to simulate DRV world in a GCM.

the 90s that has not received the credit it deserves, towards pedagogical purposes - be it for problem sets, lectures, and, if feeling particularly ambitious, review articles and textbook chapters on moist dynamics.

Appendix A

Alternative Definition for the Reduction Factor

We can rewrite the definition of r shown in Eq. (1.4) using

$$\frac{\partial\theta}{\partial p} = \frac{\partial\theta}{\partial p}\Big|_{\theta^*} + \frac{\partial\theta}{\partial\theta^*}\Big|_p \frac{\partial\theta^*}{\partial p}, \tag{A.1}$$

and the relationship

$$\frac{\partial\theta}{\partial\theta^*}\Big|_p = \frac{\Gamma_m}{\Gamma_d}\frac{\theta}{\theta^*}, \tag{A.2}$$

derived in Emanuel et al. (1987) to arrive at the alternative expression for r

$$r = \frac{\theta}{\theta^*}\frac{\Gamma_m}{\Gamma_d}\frac{\frac{\partial\theta^*}{\partial p}}{\frac{\partial\theta}{\partial p}}. \tag{A.3}$$

Bibliography

A. Adames, Y. (2018). Interactions between water vapor and potential vorticity in synoptic-scale monsoonal disturbances: Moisture vortex instability. *Journal of the Atmospheric Sciences*, 75:2083–2106.

Adames, A. (2021). Interactions between water vapor, potential vorticity, and vertical wind shear in quasi-geostrophic motions: Implications for rotational tropical motion systems. *Journal of the Atmospheric Sciences*, 8:903–923.

Ahmadi-Givi, F., Graig, G. C., and Plant, R. S. (2004). The dynamics of a midlatitude cyclone with very strong latent-heat release. *Quart. J. Roy. Meteor. Soc.*, 130:295–323.

Bembenek, E., Straub, D. N., and Merlis, T. M. (2020). Effects of moisture in a two-layer model of the midlatitude jet stream. *J. Atmos. Sci.*, 77:131–147.

Boettcher, M. and Wernli, H. (2013). A 10-yr climatology of diabatic rossby waves in the northern hemisphere. *Mon. Wea. Rev.*, 141:1139–1154.

Boettcher, M. and Wernli, H. (2015). Diabatic Rossby waves in the Southern Hemisphere. *Quarterly Journal of the Royal Meteorological Society*, 141:3106–3117.

Booth, J. F., Polvani, L., O'Gorman, P. A., and Wang, S. (2015). Effective stability in a moist baroclinic wave. *Atmos. Sci. Lett.*, 16:56–62.

Bretherton, F. P. (1966). Baroclinic instability and the short wavelength cut-off in terms of potential vorticity. *Quart. J. Roy. Meteor. Soc.*, 92:335–345.

Büeler, D. and Pfahl, S. (2017). Potential vorticity diagnostics to quantify effects of latent heating in extratropical cyclones. Part I: Methodology. *J. Atmos. Sci.*, 74:3567–3590.

Burns, K. J., Vasil, G. M., Oishi, J. S., Lecoanet, D., and Brown, B. P. (2020). Dedalus: A flexible framework for numerical simulations with spectral methods. *Physical Review Research*, 2:023068.

Charney, J. G. (1947). The dynamics of long waves in a baroclinic westerly current. *J. Atmos. Sci.*, 4:136–162.

Charney, J. G. (1971). Geostrophic Turbulence. *J. Atmos. Sci.*, 28:1087–1095.

Cohen, N. Y. and Boos, W. R. (2016). Perspectives on moist baroclinic instability: Implications for the growth of monsoon depressions. *J. Atmos. Sci.*, 73:1767–1788.

Davis, C. A. and Emanuel, K. A. (1991). Potential vorticity diagnostics of cyclogenesis. *Monthly Weather Review*, 119:1929–1953.

De Vries, H., Methven, J., Frame, T. H., and Hoskins, B. J. (2010). Baroclinic waves with parameterized effects of moisture interpreted using Rossby wave components. *J. Atmos. Sci.*, 67:2766–2784.

Diaz, M. and Boos, W. R. (2021). Evolution of idealized vortices in monsoon-like shears: Application to monsoon depressions. *Journal of the Atmospheric Sciences*, 78:1207–1225.

Dwyer, J. G. and O'Gorman, P. A. (2017). Moist Formulations of the Eliassen–Palm Flux and Their Connection to the Surface Westerlies. *J. Atmos. Sci.*, 74:513–530.

Eady, E. T. (1949). Long Waves and Cyclone Waves. *Tellus*, 1:33–52.

Emanuel, K. A. (2001). The role of water in atmospheric dynamics and climate. In Robert Pearce, editor, *Meteorology at the Millenium*, page 333pp. Academic Press.

Emanuel, K. A., Fantini, M., and Thorpe, A. J. (1987). Baroclinic instability in an environment of small stability to slantwise moist convection. Part I: two-dimensional models. *J. Atmos. Sci.*, 44:1559–1573.

Fantini, M. (1995). Moist Eady waves in a quasigeostrophic three-dimensional model. *J. Atmos. Sci.*, 52:2473–2485.

Ferziger, J. H. and Perić, M. (2002). *Computational Methods for Fluid Dynamics*. Springer Berlin Heidelberg, 3rd edition.

Fjørtoft, R. (1950). Application of integral theorems in deriving criteria of stability for laminar flows and for the baroclinic circular vortex. *Geofysiske Publikasjoner*, 17:1–52.

Frierson, D. M. W. (2007). The Dynamics of Idealized Convection Schemes and Their Effect on the Zonally Averaged Tropical Circulation. *J. Atmos. Sci.*, 64:1959–1976.

Frierson, D. M. W., Held, I. M., and Zurita-Gotor, P. (2006). A Gray-Radiation Aquaplanet Moist GCM. Part I: Static Stability and Eddy Scale. *J. Atmos. Sci.*, 63:2548–2566.

Held, I. M. (1999). The macroturbulence of the troposphere. *Tellus*, 51:59–70.

Hersbach, H., Bell, B., Berrisford, P., Hirahara, S., Horányi, A., Muñoz-Sabater, J., Nicolas, J., Peubey, C., Radu, R., Schepers, D., Simmons, A., Soci, C., Abdalla, S., Abellan, X., Balsamo, G., Bechtold, P., Biavati, G., Bidlot, J., Bonavita, M., De Chiara, G., Dahlgren, P., Dee, D., Diamantakis, M., Dragani, R., Flemming, J.,

Forbes, R., Fuentes, M., Geer, A., Haimberger, L., Healy, S., Hogan, R. J., Hólm, E., Janisková, M., Keeley, S., Laloyaux, P., Lopez, P., Lupu, C., Radnoti, G., de Rosnay, P., Rozum, I., Vamborg, F., Villaume, S., and Thépaut, J. N. (2020). The ERA5 global reanalysis. *Quarterly Journal of the Royal Meteorological Society*, 146:1999–2049.

Hogg, N. and Stommel, H. (1985). The heton, an elementary interaction between discrete baroclinic geostrophic vortices, and its implications concerning eddy heat-flow. *Proceedings of the Royal Society of London. A. Mathematical and Physical Sciences*, 397:1–20.

Holton, J. R. (2004). *An introduction to dynamic meteorology: fourth edition*. Elsevier Academic Press.

Hoskins, B. J. (1975). Geostrophic momentum approximation and the semi-geostrophic equations. *J. Atmos. Sci.*, 32:233–242.

Hoskins, B. J. (1976). Baroclinic waves and frontogenesis Part I: Introduction and Eady waves. *Quart. J. Roy. Meteor. Soc.*, 35:414–432.

Hoskins, B. J., McIntyre, M. E., and Robertson, A. W. (1985). On the use and significance of isentropic potential vorticity maps. *Quart. J. Roy. Meteor. Soc.*, 111:877–946.

Joos, H. and Wernli, H. (2012). Influence of microphysical processes on the potential vorticity development in a warm conveyor belt: A case-study with the limited-area model COSMO. *Quarterly Journal of the Royal Meteorological Society*, 138:407–418.

Kohl, M. and O'Gorman, P. A. (2022). The Diabatic Rossby Vortex: Growth Rate, Length Scale and the Wave-Vortex Transition. *J. Atmos. Sci.*, 79:2739–2755.

Kutzbach, G. (1979). *The thermal theory of cyclones*. American Meteorological Society.

Lackmann, G. M. (2002). Cold-frontal potential vorticity maxima, the low-level jet, and moisture transport in extratropical cyclones. *Mon. Wea. Rev.*, 130:59–74.

Lambaerts, J., Lapeyre, G., and Zeitlin, V. (2012). Moist versus dry baroclinic instability in a simplified two-layer atmospheric model with condensation and latent heat release. *J. Atmos. Sci.*, 69:1405–1426.

Lapeyre, G. and Held, I. M. (2004). The Role of Moisture in the Dynamics and Energetics of Turbulent Baroclinic Eddies. *Journal of the Atmospheric Sciences*, 61:1693–1710.

Levine, X. J. and Schneider, T. (2015). Baroclinic Eddies and the Extent of the Hadley Circulation: An Idealized GCM Study. *J. Atmos. Sci.*, 72:2744–2761.

Li, Z. and O'Gorman, P. A. (2020). Response of vertical velocities in extratropical precipitation extremes to climate change. *Journal of Climate*, 33:7125–7139.

Martínez-Alvarado, O., Gray, S. L., and Methven, J. (2016). Diabatic processes and the evolution of two contrasting summer extratropical cyclones. *Mon. Wea. Rev.*, 144:3251–3276.

Montgomery, M. T. and Farrell, B. F. (1991). Moist surface frontogenesis associated with interior potential vorticity anomalies in a semigeostrophic model. *J. Atmos. Sci.*, 48:343–368.

Montgomery, M. T. and Farrell, B. F. (1992). Polar low dynamics. *J. Atmos. Sci.*, 49:2484–2505.

Moore, R. W. and Montgomery, M. T. (2004). Reexamining the dynamics of short-scale, diabatic rossby waves and their role in midlatitude moist cyclogenesis. *J. Atmos. Sci.*, 61:754–768.

Moore, R. W. and Montgomery, M. T. (2005). Analysis of an idealized, three-dimensional diabatic Rossby vortex: A coherent structure of the moist baroclinic atmosphere. *J. Atmos. Sci.*, 62:2703–2725.

Moore, R. W., Montgomery, M. T., and Davies, H. C. (2008). The integral role of a diabatic rossby vortex in a heavy snowfall event. *Mon. Wea. Rev.*, 136:1878–1897.

Moreno-Ibáñez, M., Laprise, R., and Gachon, P. (2021). Recent advances in polar low research: current knowledge, challenges and future perspectives. *Tellus*, 73:1–31.

Nielsen-Gammon, J. W. and Gold, D. A. (2008). Dynamical Diagnosis: A Comparison of Quasigeostrophy and Ertel Potential Vorticity. *Meteorological Monographs*, 33:183–202.

Oda, M. and Kanehisa, H. (2011). Analytical solutions of initial value problem of diabatic Rossby waves. *Journal of the Meteorological Society of Japan*, 89:161–169.

O'Gorman, P. A., Merlis, T. M., and Singh, M. S. (2018). Increase in the skewness of extratropical vertical velocities with climate warming: fully nonlinear simulations versus moist baroclinic instability. *Quart. J. Roy. Meteor. Soc.*, 144:208–217.

O'Gorman, P. A. and Schneider, T. (2008). The hydrological cycle over a wide range of climates simulated with an idealized GCM. *J. Climate*, 21:3815–3832.

O'Gorman, P. A. (2011). The Effective Static Stability Experienced by Eddies in a Moist Atmosphere. *J. Atmos. Sci.*, 68:75–90.

Parker, D. J. and Thorpe, A. J. (1995). Conditional convective heating in a baroclinic atmosphere: a model of convective frontogenesis. *J. Atmos. Sci.*, 52:1699–1711.

Pedlosky, J. (1964). The Stability of Currents in the Atmosphere and the Ocean: Part I. *Journal of the Atmospheric Sciences*, 21:201–219.

Pendergrass, A. G. and Gerber, E. P. (2016). The rain is askew: Two idealized models relating the vertical velocity and precipitation distributions in a warming world. *J. Clim.*, 29:6445–6462.

Perron, M. and Sura, P. (2013). Climatology of non-gaussian atmospheric statistics. *J. Climate*, 26:1063–1083.

Persson, P. O. G. (1995). Simulations of the potential vorticity structure and budget of fronts 87 IOP8. *Quart. J. Roy. Meteor. Soc.*, 121:1041–1081.

Pfahl, S., O'Gorman, P. A., and Singh, M. S. (2015). Extratropical cyclones in idealized simulations of changed climates. *J. Climate*, 28:9373–9392.

Phillips, N. (1954). Energy Transformations and Meridional Circulations associated with simple Baroclinic Waves in a two-level, Quasi-geostrophic Model. *Tellus*, 6:273–286.

Sardeshmukh, P. D., Compo, G. P., and Penland, C. (2015). Need for caution in interpreting extreme weather statistics. *J. Climate*, 28:9166–9187.

Schneider, T., O'Gorman, P. A., and Levine, X. J. (2010). Water vapor and the dynamics of climate changes.

Schubert, W. and Alworth, B. (1987). Evolution of potential vorticity in tropical cyclones. *Quarterly Journal of the Royal Meteorological Society*, 113:147–162.

Shaw, W. N. (1903). Methods of Meteorological Investigation. *Monthly Weather Review*, September:415–420.

Snyder, C. and Lindzen, R. S. (1991). Quasi-geostrophic wave-CISK in an unbounded baroclinic shear. *J. Atmos. Sci.*, 48:76–86.

Solomon, A. and Stone, P. H. (2001). Equilibration in an Eddy resolving model with simplified physics. *Journal of the Atmospheric Sciences*, 58:561–574.

Stoelinga, M. T. (1996). A potential vorticity-based study of the role of diabatic heating and friction in a numerically simulated baroclinic cyclone. *Monthly Weather Review*, 124:849–874.

Stone, H. L. (1968). Iterative Solution of Implicit Approximations of Multidimensional Partial Differential Equations. *SIAM Journal on Numerical Analysis*, 5:530–558.

Stone, P. H. and Carlson, J. H. (1979). Atmospheric lapse rate regimes and their parameterization. *Journal of the Atmospheric Sciences*, 36:415–423.

Tamarin-Brodsky, T. and Hadas, O. (2019). The Asymmetry of Vertical Velocity in Current and Future Climate. *Geophysical Research Letters*, 46:374–382.

Tierney, G., Posselt, D. J., and Booth, J. F. (2018). An examination of extratropical cyclone response to changes in baroclinicity and temperature in an idealized environment. *Climate Dyn.*, 51:3829–3846.

Vallis, G. K. (2017). *Atmospheric and oceanic fluid dynamics: Fundamentals and large-scale circulation, second edition.* Cambridge University Press.

Wernli, H. and Davies, H. C. (1997). A Lagrangian-based analysis of extratropical cyclones. I: The method and some applications. *Quarterly Journal of the Royal Meteorological Society*, 123:467–489.

Wernli, H., Dirren, S., Liniger, M. A., and Zillig, M. (2002). Dynamical aspects of the life cycle of the winter storm 'Lothar' (26-26 December 1999). *Quart. J. Roy. Meteor. Soc.*, 128:405–429.

Whitaker, J. S. and Davis, C. A. (1994). Cyclogenesis in a saturated environment. *J. Atmos. Sci.*, 51:889–908.

Zedan, M. and Schneider, G. E. (1983). A three-dimensional modified strongly implicit procedure for heat conduction. *AIAA Journal*, 21:295–303.

Zurita-Gotor, P. (2005). Updraft/downdraft constraints for moist baroclinic modes and their implications for the short-wave cutoff and maximum growth rate. *J. Atmos. Sci.*, 62:4450–4458.